Semi-Exclusive studies of $\Delta(1232)$ electroproduction in ^3He

Westley Ingram

Presented as a Thesis for the Degree of Doctor of Philosophy

Department of Physics and Astronomy,
University of Glasgow,
June 2003.

Abstract

The results of electron scattering on ^3He are presented, which are based on an analysis of the channels $^3He(e,e'p\pi^0)$ and $^3He(e,e'p\pi^-)$. The CLAS detector array at the Jefferson Laboratory was used to reconstruct semi-exclusively the decay of the $\Delta^0(1232)$ and $\Delta^+(1232)$. The $\Delta(1232)$ is studied by observing the $p\pi$ decay products. This thesis consists of three sets of results. (i)The semi-exclusive observation of the variation of the $\Delta(1232)$ invariant mass with Q^2. This does not support the previous observations of Richard Sealock[1] based on inclusive electron scattering experiments that the invariant mass of the $\Delta(1232)$ increases with Q^2 in the nuclear medium. (ii)Measurements of the angular distributions of the decay products of the $\Delta(1232)$ which suggest some difference between the $p \rightarrow \Delta$ and $n \rightarrow \Delta$ transitions. Both (i) and (ii) rely upon a geometric acceptence correction for CLAS and are compared to theoretical predictions of the MAID[2] code. (iii)Studies of the potential experienced by a proton or Δ^0 as a function of momentum in the nuclear medium which show a consistent difference of approximately 15 MeV as the momentum is varied.

Declaration

The data presented in this thesis were obtained in collaboration with colleagues from the e2 run group of the CLAS collaboration, Jefferson Lab. I participated in the execution of the experiment and the analysis of these data is my own work. This thesis was composed by myself.

Westley Ingram.

Acknowledgements

The Psalmist wrote some time ago “Unless the Lord builds the house, its builders labour in vain.[3]” as such it is fitting that first I thank God for seeing me through these past four years.

When looking to thank less divine persons it is not difficult to draw up quite a list. First and foremost is Dr. James Kellie, my supervisor who has been both encouraging and critical in due season and was willing to read drafts of this thesis both in and out of season. I am also profoundly grateful to Steven McLauchlan, who has been both a good friend and debugger from the start. The work presented herein would not have come about if not for the work of the e2 run group, special thanks goes to Stepan Stepanyan, Larry Weinstein, Mauric Holtrop and Derek Branford. The Nuclear Physics group of Glasgow University has been consistently patient with me, special praise goes to my various office-mates over the years as well as to David Ireland, Douglas MacGregor and the ever cheerful Kenneth Livingston for their additional supervision.

In closing I would like to dedicate this thesis to my late father, Winston Ingram and my ever punctual mother, Mary Ingram.

Contents

List of Figures

List of Tables

Chapter 1

Introduction

The existence of Atomic Nuclei has been well established since Rutherford's experiments in the early years of the 20th century[4]. While the assertion that the majority of the atomic mass is concentrated within a positively charged nucleus is recognized universally, it is by no means clear what is going on inside the atomic nucleus. It is now hardly contentious to say that the nucleus is made up of hadrons, the mass provided by baryons and the interactions mediated by mesons. This leaves an immense number of degrees of freedom for nuclear models. Experiments on the nucleus and nucleons may constrain these models, providing information on nuclear size, charge and mass distribution etc. These experiments have led to the popularity of nuclear shell models[5] which assume a central and spin-orbit potential, leading to shell structures for the nuclear protons and neutrons. These shell models do not describe experiment perfectly, however. Charge and mass distribution experiments show evidence for interactions between nucleons which the mean field approach of the shell model does not cater for. These include many body forces and short range correlations. There is also evidence for baryons in the nucleus other than the proton and neutron[6].

Whatever the behaviour of the nucleus it depends upon the nature of the nuclear constituents and their interactions with each other. This means that the potential that any particle experiences is of interest, as it will assist us in understanding the nuclear interactions. For example, any difference in the behaviour of the neutron as compared with the proton will give information about their different quark contents. Although at a certain level they are generally considered to be identical but for their electromagnetic charge state. Also of interest is the behaviour of hadronic resonances in the nucleus. For example the P_{33}^{+} ($\Delta(1232)$) resonance may have an identical quark content to the P_{11}^{+} proton but has a different quark spin structure and invariant mass.[1]

[1]The notation $l_{IJ}^{P}$is used throughout this thesis to name particles. I is twice the isospin of the particle, J is twice the total angular momentum and P is the parity. l is the orbital angular momentum of the decay

The nucleon, which in this thesis refers to protons and neutrons only, has been seen to behave differently within and without the nucleus. For example such properties as invariant mass, size, shape, and measured reaction cross sections show such differences. These differences are not well understood by current models of the nucleon and their investigation may prove very useful for the improvement of these models. Resonances, such as the $\Delta(1232)$ (the subject of this thesis) are also seen to behave differently depending upon their nuclear environment. The study of the behaviour of the $\Delta(1232)$ also plays a role in our understanding of the resonances themselves, an area of considerable interest to QCD physicists[7, 8].

Baryonic resonances take many forms, all of which are 3-quark systems with an invariant mass greater than that of the free proton or neutron (which are considered the ground state). They are unstable, decaying back to lighter particles. The $\Delta(1232)$ is the first resonance. The number and nature of these resonances is a topic of some interest as different pQCD (perturbative Quantum Chromo-Dynamic) models make different predictions. This is the main motivation for the search for missing resonances at high invariant mass[9].

When studying resonances it is necessary to excite a resonance directly by means of some probe. Common and useful probes are the pion, photon and electron. The subject of this thesis is an electron scattering experiment where the electromagnetic interaction is mediated via a virtual photon. Electromagnetic (e.m.) probes (electrons and photons) have the advantage over pion probes since the electromagnetic interaction is well understood, and the probe does not interact with the target via the poorly understood strong nuclear force[6].

The e.m. probes also investigate the whole body of the nuclear target whereas the pion usually only interacts on the surface, or may lead to the break up of the target. This means that the e.m. probe leads to information on the whole nucleus with relatively unambiguous results[6].

The electron has a lower interaction cross section than the photon. However it has the advantage that the virtual photons it provides do not obey the $E = pc$ relation of the real photon (where E is the energy, p the momentum and c the speed of light). This means that a quantity Q^2 can be defined which is analogous to the invariant mass squared of the virtual photon (i.e. $Q^2 = \underline{q}^2 - \omega^2$, where ω and $\underline{q}$ are the change in energy and momentum between the incoming and scattered electron. They are also the energy and momentum carried by the virtual photon.). The virtual photon may have transverse and longitudinal components of polarisation as opposed to the purely transverse real photon. This allows additional degrees of freedom for experiments to explore.

In order to use electrons to probe the nucleus, high quality electron beams are necessary.

products. The two most common instances of this notation are for the spin $\frac{1}{2}$, isospin $\frac{1}{2}$ nucleon with positive parity (P_{11}^{+}) and the spin $\frac{3}{2}$, isospin $\frac{3}{2}$ $\Delta(1232)$ resonance with positive parity(P_{33}^{+}).

The ideal case of a 100% duty factor electron beam with good energy and spatial resolution has in recent years come close to realisation. The Continuous Electron Beam Electron Facility (CEBAF) at the Jefferson Laboratory, which was used for the experiment described in this thesis, comes very close to this ideal.

Jefferson Lab. is based in Newport News, Virginia, USA. It consists of an electron beam facility which delivers continuous wave electrons to three (soon to be four) experimental halls. At the time of this experiment, beam energies came in increments of 1.1GeV energy plus the 0.062GeV injector energy. JLab allows a range of experiments using polarised and unpolarised electrons and photons. Jefferson Lab's main physics goals are the study of free nucleons and nucleons in the nucleus. The experiment described in this thesis was carried out in May 1999 using the CLAS detector array housed in JLab's hall B.

CLAS is a large solid angle detector array which provides good particle identification. Due to this versatility, experimental runs can simultaneously cater for a number of analysis interests. The data upon which this thesis is based were taken during the e2a run period. The e2 run group is the experimental arm of the MultiHadron physics group, and a part of the CLAS collaboration.

The large solid angle coverage and particle identification of CLAS allows the detection of many reaction products over a broad range of kinematics. This makes semi-exclusive or exclusive experiments (where the reaction is fully determined) possible. This is ideal for studying invariant mass distributions of the $\Delta(1232)$ resonance, particularly since previous results obtained from inclusive experiments (where only the electron is detected) are very ambiguous due to the effects of competing reaction channels in the region of the $\Delta(1232)$. The ability to detect the decay products of the $\Delta(1232)$ (a nucleon and pion) make the analysis significantly clearer.The large azimuthal coverage also allows measurements of reactions where the decay products are emitted out of the electron scattering plane. The resulting azimuthal distribution of the $\Delta(1232)$ decay products sheds light upon the nature of the transition from nucleon to $\Delta(1232)$.

Before detectors such as CLAS became available, a great deal of work was carried out studying the electromagnetic response of the nucleus by measuring the energy and momentum of the scattered electron[10, 11, 12, 13, 14, 15, 16]. As stated above the square of the invariant mass, Q^2, of the virtual photon may be deduced from the detected electron. It is also possible to define W^2, the invariant mass squared of the hadronic system which is calculated from the exchanged virtual photon coupling to a target nucleon, i.e. $W^2 = (\omega + M_N)^2 - \underline{q}^2 = M_N^2 + 2\omega M_N - Q^2$, where M_N is the nucleon mass. W provides a characteristic spectrum[6] which features the quasi-elastic peak at the nucleon mass, nucleon resonances at higher invariant masses and also other features arising from two nucleon knockout and non-resonant pion production. An example of such a W distribution is

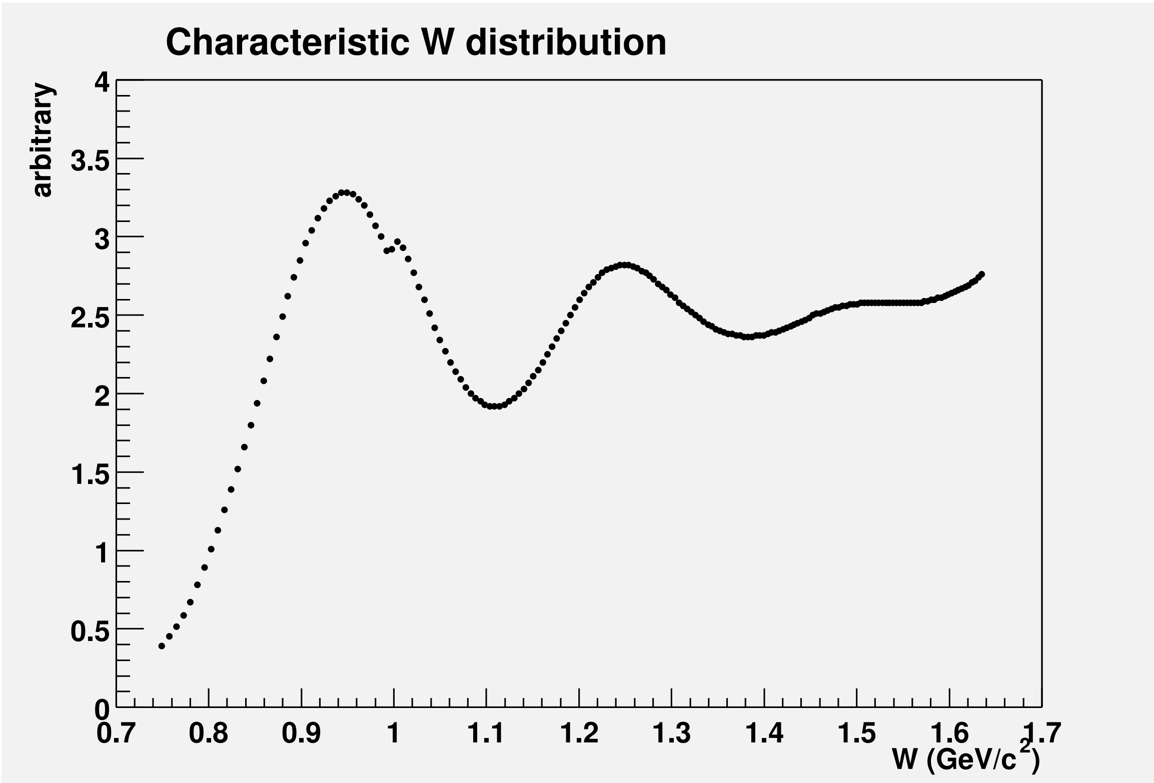

Figure 1.1: Characteristic inclusive invariant mass (W) distribution.
This distribution represents the inclusive electromagnetic response of the atomic nucleus to an electron probe. At the nucleon and $\Delta(1232)$ invariant mass broad peaks are present, which are modified by the presence of background processes. These include the non-resonant pion production (or Born terms), 2N knockout, which contributes mainly in the 'dip' region between the two peaks. After the $\Delta(1232)$ peak is the continuum where the higher resonances are not easily separable. The small peak at $1.02GeV/c^2$ is a feature of the code used to produce this distribution and not of any physical significance.

shown in figure 1.1(The small peak at about $1.02GeV/c^2$ is not a physical phenomenon but a feature of the code used to generate this plot).

Since all of these features overlap significantly on the W distribution, estimations of the relevant strengths of these different processes are heavily model dependent.

Using data from inclusive measurements, in 1989 Sealock et al.[17] observed that the peak position and width of the $\Delta(1232)$ varied depending upon the Q^2 of the virtual photon which excited it and the nucleus in which it was excited[18]. If these results could be verified, the consequences would be significant, since it would mean that the properties of nuclear constituents are sensitive to their form of excitation and that this sensitivity could be observed directly in electron scattering experiments.

Sealock et al.[17] found the centroid of the W spectra to vary with Q^2 for a number of atomic nuclei as shown in figure 1.2, the variation being most sensitive to Q^2 at low values

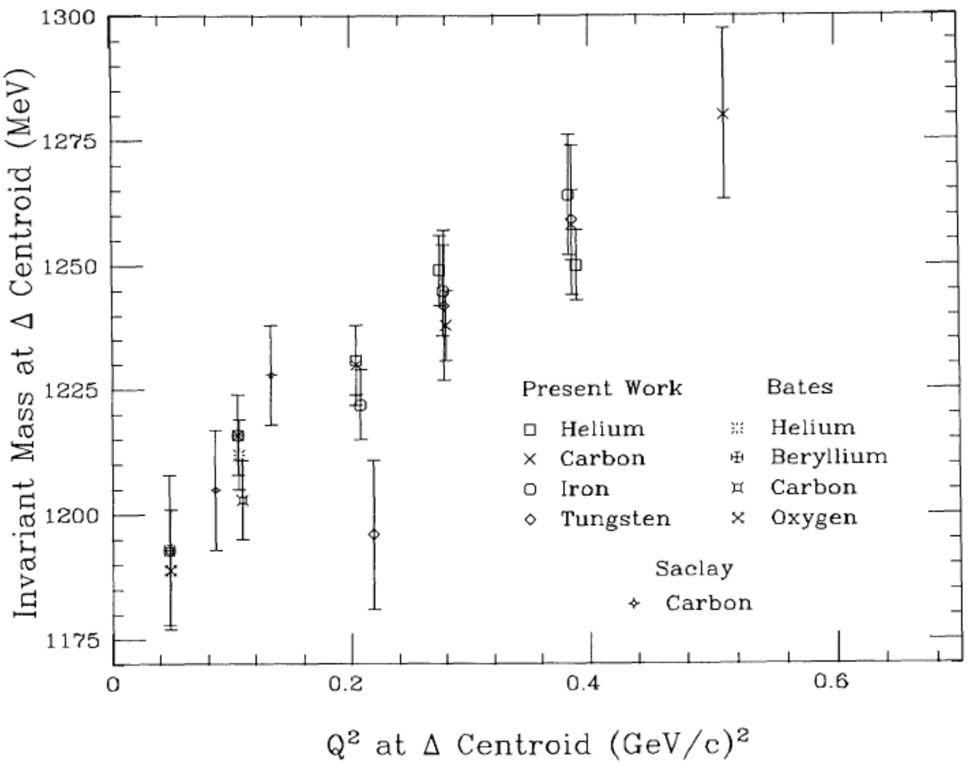

Figure 1.2: Δ centroid vs. Q^2 for various atomic nuclei.
These results are taken from ref [17]. and show measured Δ centroid positions as observed from inclusive electron scattering experiments.

of Q^2[18].

The results of Sealock et al.[17] are open to question as they were based upon inclusive measurements, and his extraction of the $\Delta(1232)$ signal depended heavily on the models they used to calculate contributions from competing processes. Also, as the detector they used had a small angular coverage, his invariant mass spectrum had to be obtained from a number of different measurements. Consequently, his overall spectrum was dependent upon accurate calibrations for a range of different experimental configurations.

When the CLAS detector became available, Selaock et al proposed a series of exclusive measurements examining the effect of Q^2 and the atomic mass number of the target nucleus on the properties of the $\Delta(1232)$. (This proposal was accepted under CLAS experiment 89-017[1], and the work which is the basis of this thesis has grown out of this proposal.)

The results presented here are from an experiment where 1.162GeV unpolarised electrons were incident upon a liquid ^3He target. The $^3He(e, e'p\pi^0)pn$ and $^3He(e, e'p\pi^-)pp$ channels have been studied by detecting the proton and pion. In the case of the π^0 the two decay photons were detected from which the four vector of the π^0 was reconstructed.

This thesis features three sets of analyses which are significantly independent of one another.

The first is a study of the invariant mass of the $\Delta(1232)$, and its variation with Q^2 in ^3He. This was done using the two channels mentioned above. The available Q^2 distribution was split into three ranges and the resultant invariant mass distributions for the corresponding data sets were plotted and fitted.

The second is a study of the azimuthal distributions of the decay products of the $\Delta(1232)$ in the Δ rest frame for the same two channels. This analysis follows closely the work done by Joo et al[19]. which was carried out using the $p(e, e'p\pi^0)$ reaction, where the proton and scattered electron were detected and the four vector of the π^0 is deduced from the missing momentum for events where the missing mass is compatible with a missing π^0. Due to the nuclear target used in our experiment this approach is not suitable. The $\pi^-$was measured directly, and the π^0 reconstructed from its directly measured decay products (which are two photons).

The final area of study looks at the nuclear potential experienced by the proton and Δ^0 in the nucleus. For each particle the difference between the potential experienced before and after the particle interacts with the virtual photon is calculated. This generally follows but improves upon the approach taken in reference [20].

Chapter 2

Theoretical background

2.1 Electron Scattering

This thesis is based upon an experiment where electrons of energy 1.162 GeV and zero average polarization were incident upon a liquid ^3He target.

2.1.1 Electrons

The spin $\frac{1}{2}$ electron has a charge of -1 $(-1.627 \times 10^{-19}\,C)$ and a mass of $0.511\,MeV/c^2$ $(9.11 \times 10^{-31}\,kg)$. At the energies discussed in this thesis it is safe to consider the electrons as massless (when compared to the other particles of interest, i.e. the $140MeV/c^2$ pions and the $940MeV/c^2$ nucleons) and always traveling at the speed of light $(c = 2.99 \times 10^8 ms^{-1})$.

The $\Delta(1232)$ excitation can be considered as the result of the exchange of a single virtual photon (impulse approximation) with the nucleon being excited. This is shown in figure 2.1, where an incident electron scatters via the virtual photon from a target nucleon(considered stationary) and excites it into a Δ. Although we are chiefly interested in the excitation of the $\Delta(1232)$ this diagram is applicable to any other impulse event, producing other nucleon resonances for example.

The electron interacts only via the electromagnetic force. This means it interacts with particles with a net charge (i.e. the proton or charged pion) or particles with a significant magnetic moment (i.e. the neutron). As the electron interacts by the exchange of virtual photons (in this case by only one) the energy and momentum exchange of the interaction has more degrees of freedom than for a real photon. Also, the momentum exchange can have both longitudinal and transverse components, giving rise to areas of physics inaccessible with real photons.

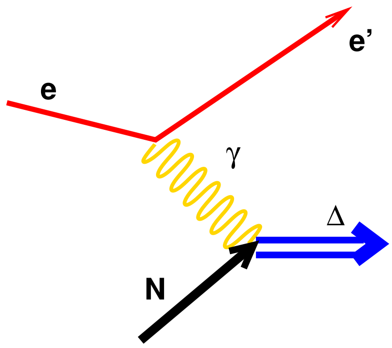

Figure 2.1: Impulse Delta excitation.
Here the red electron(e) scatters off the black nucleon (N) via the exchange of a yellow virtual photon(γ) producing the blue Delta resonance (Δ).

2.1.2 The Virtual Photon

Unlike the real photon, which obeys the relation $E = pc$, the momentum and energy of the virtual photon (defining a 4-vector (q,ω)) are independent. Due to this feature of the virtual photon, there exists a quantity Q^2 which is analogous to the invariant mass of a particle. Q^2 obeys the relations expressed in equations 2.1 and 2.2.

$$Q^2 = q^2 - \omega^2 \tag{2.1}$$

$$Q^2 = 4EE^{'}sin^2(\frac{\theta_e}{2}) \tag{2.2}$$

E and $E^{'}$are the energies of the incident and scattered electron respectively and θ_e is the scattering angle of the electron.

As the electron scattering distribution is concentrated at small scattering angles the Q^2 distribution is also very forward peaked. The experimental distribution reaches a minimum value defined by the detector geometry.

2.1.3 Electron scattering experiments

An incident virtual photon can initiate a number of reactions within the target nucleus (as well as some elsewhere - examples are interactions with the target cell walls and events where the electrons radiate real photons leading to radiative losses[21, 22, 23, 24]). To determine which reaction has taken place it is often necessary to detect all of the outgoing particles. Experimentally, this is difficult, especially with heavy nuclei, but also with ^3He where each final state particle must be detected. Although CLAS provides a large detector solid angle, it is often problematic to define the reaction channel for a given event. When describing experiments of the type performed by CLAS, the term inclusive refers to events where only the scattered electron is detected. If the beam energy and momentum of the scattered electron are known then this allows the virtual photon 4-vector to be deduced. If a sufficient number of the outgoing particles are detected so there is no ambiguity about the reaction channel. Then the event is referred to as exclusive. All events which lie between these two descriptions are semi-inclusive (or semi-exclusive).

The inclusive electromagnetic response of the atomic nucleus.

The incident virtual photon may interact with either an individual nucleon, causing direct nucleon knockout, or with nucleon pairs causing 2N knockout particularly if the two nucleons are closely correlated. It may also interact with a charged meson (mainly pions) within the nucleus(the uncharged mesons do not significantly interact with the e.m.-field of the virtual photon). Meson interactions also contribute to 2N knockout and also to non-resonant meson production(Born terms). These Born terms can contribute significantly to the $N\pi^{\pm}$channels. Also, the virtual photon may cause some nucleonic excitation into the $\Delta(1232)$, which is of particular interest for this thesis, but also to other Δ and N^*resonances. These processes (for a free nucleon target) are shown as Feynman diagrams in figure 2.2.

With only the scattered electron detected, and hence only the four momentum of the exchanged virtual photon available, it is possible to calculate the quantity W, where W is the hadronic invariant mass of the system. It is the invariant mass of a particle whose 4-vector is the sum of the target and the virtual photon 4-vector.

This is shown in equation 2.3. The quantity W^2 is then calculated as in equation 2.4.

$$W = |T(0, M_T) - \gamma(q, \omega)| \tag{2.3}$$

$$W^2 = M_T^2 + 2M_T\omega - Q^2 \tag{2.4}$$

The shape of the inclusive W spectrum depends upon the experimental conditions (such as beam energy, target and electron scattering angle) but it usually has a characteristic shape. An example of the characteristic W distribution is shown in figure 2.3, and exhibits the main contributions to the inclusive cross-section.

As can be seen the different contributions overlap significantly. This means that it is only possible to use an inclusive measurement to study the $\Delta(1232)$ in the nucleus if the behaviour of the other contributions is well understood for the relevant experimental condi-

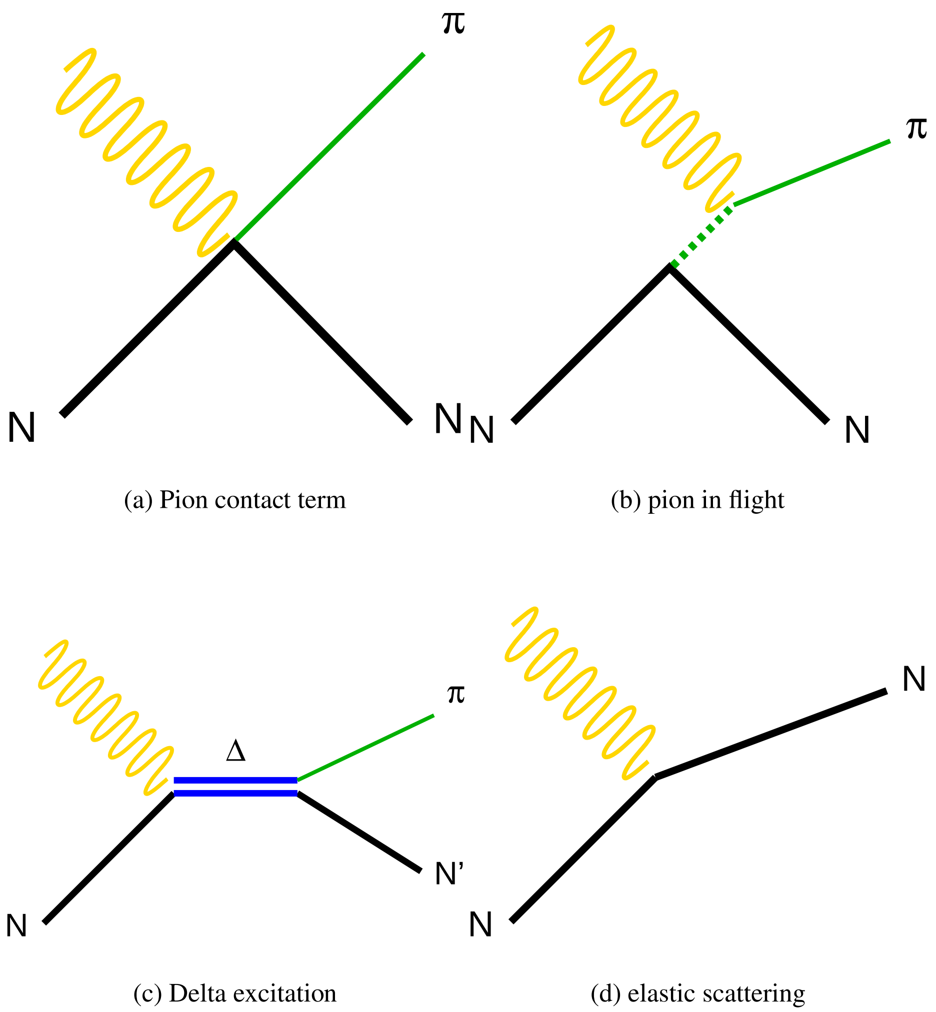

(a) Pion contact term

(b) pion in flight

(c) Delta excitation

(d) elastic scattering

Figure 2.2: Inclusive Feynman diagrams

Above are a number of possible processes when a virtual photon is incident upon a nucleon target. The terms shown are a) the pion contact (seagull) term, b) the pion in flight term, c) Δ excitation and d) elastic scattering. These are a few of many possible processes. If interactions involving multiple virtual photon are considered this adds alot more possible reactions.

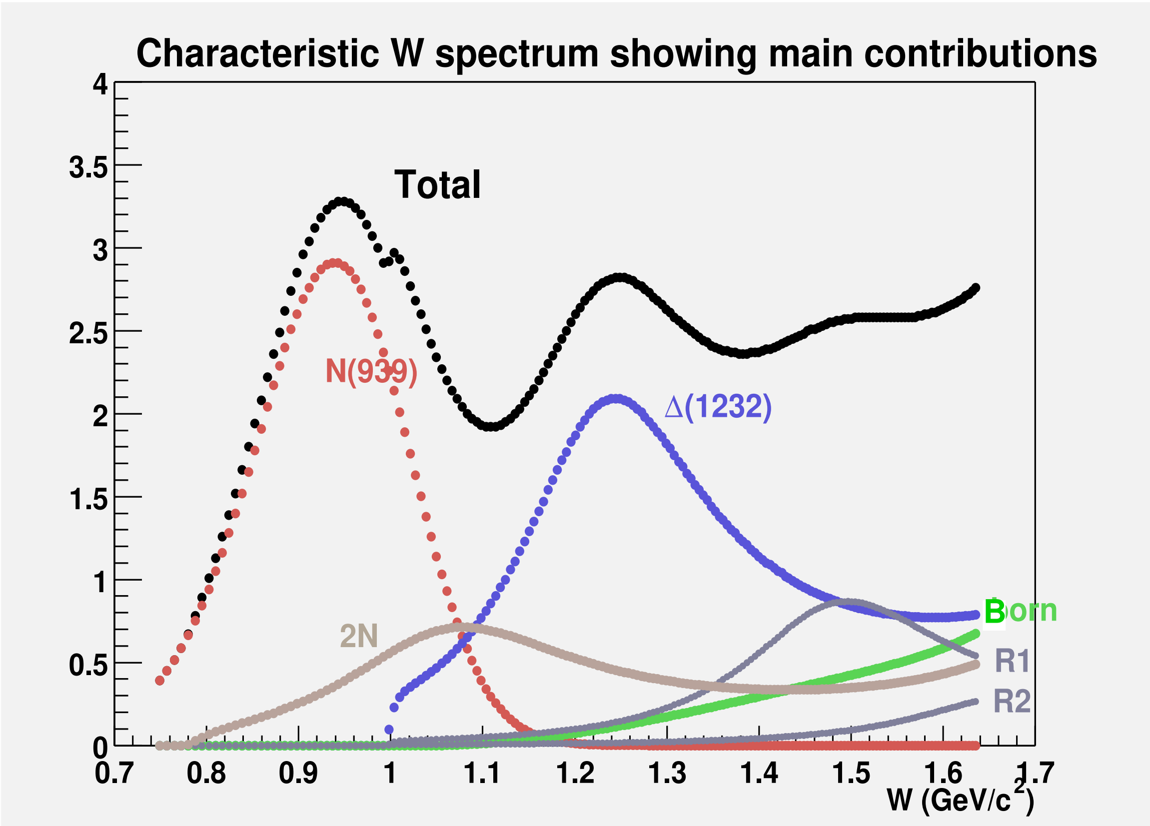

Figure 2.3: Contributions toward the characteristic inclusive W spectrum.
Here the characteristic W spectrum of figure 1.1 is shown with the contributions shown. This figure is mainly schematic as the processes which make up the total and their interactions with each other are not fully understood. From this figure it is clear that the relative strengths of these contributions will lead to variations of the observed centroid position of the $\Delta(1232)$.
This plot was created using the qfs[25] code written by Lightbody and O'Connell. It is used here only to show the contributions to the total cross-section of the quasi-free response of a nucleus and the regions of W where they contribute most. The total cross-section shows a discontinuity at approximately $1GeV/c^2$. This is a result of the poorly reproduced $\Delta(1232)$ distribution. In reality the $\Delta(1232)$distribution falls to zero at the threshhold of the pion mass and the nucleon mass. The discontinuity should be disregarded as this plot is used to show the various contributions and is not used for the analysis of any data.

tions. By extracting the $\Delta(1232)$ contribution from inclusive W spectra for a range of nuclei, Sealock et al.[17] (see section 1) deduced that the invariant mass of the $\Delta(1232)$ varied with Q^2. However, since it is doubtful the other contributions are understood sufficiently well for their effects to be extracted from the W spectrum with the necessary accuracy, the claim that the $\Delta(1232)$ invariant mass varies with Q^2, requires to be investigated by new and independent measurements. It is one of the main objectives of the present work to undertake such an investigation.

Exclusive measurements of the $\Delta(1232)$.

By measuring the final state particles from a reaction it is in some cases possible to work out the details of the reaction. In the case of $^3He(e,e^{'}p\pi^0)pn$ and $^3He(e,e^{'}p\pi^-)pp$ where a proton and a pion are detected, the 2N, Born and resonance terms all contribute. The detected proton can also be a spectator and in effect not interact with the virtual photon (this will be discussed later in section 2.4.3). This all makes it impossible to claim exclusivity for the events investigated in this thesis. However, since the electron beam energy is only 1.1GeV higher resonances are unlikely to contribute significantly to the data set measured. The kinetic energy imparted to the undetected nucleon in 2N knockout will appear as missing energy and can therefore be removed by applying appropriate kinematic cuts. However, since the non-resonant π^-contribution cannot be identified by basic kinematics it must be taken into account when interpreting any results.

2.2 The Nucleus.

The nucleus is made up of a number of quarks and gluons. It is usually easiest to use a static quark model of the nucleus and consider the quarks as arranged into 2-quark and 3-quark systems which display corporate qualities. The interactions between the 3-quark systems are usually mediated by the exchange of 2-quark systems. The most common of these 3-quark systems is the nucleon (N), a singlet state.

The neutral N state is the neutron and the positively charged N state is the proton. Although the properties of the free or isolated N have been studied extensively, there exists some evidence that the behaviour of the N is modified (see section 2.3.2) when found within the nuclear medium. These medium modifications have been studied in less detail. As well as the N state there are a number of other three quark configurations, some of which are shown in table 2.1(It is worth noting that as the nucleus is composed almost totally of up(u) and down(d) quarks, the available 3-quark arrangements are usually limited to those which consist of u and d quarks, although there is some evidence of a very small contribution from strange quarks[6].)

Table 2.1: 3 quark systems relevant to the current W range.

Isobar	name	isospin	spin	parity	mass(MeV/c^2)	width(MeV/c^2)
P_{11}^+	N(940)	1/2	1/2	+	938.3/939.6	~0
P_{33}^+	$\Delta(1232)$	3/2	3/2	+	1230-1234	115-125
P_{11}	N(1440)	1/2	1/2	+	1430-1470	250-450
D_{13}	N(1520)	1/2	3/2	-	1515-1530	110-135
S_{11}	N(1535)	1/2	1/2	-	1520-1555	100-250

As is seen in table 2.1 the N(940) is the lightest state available. The N(940) can be excited into one of the other more massive states so long as the conservation rules are obeyed. The first available of these states, is the $\Delta(1232)$ resonance. As discussed in section 2.3, the $\Delta(1232)$ is the most prominent of the excited states (or resonances) in the energy range of interest in the present thesis.

2.2.1 Resonances

Various nuclear resonances may exist within the nucleus at any given time. It has been estimated that the $\Delta(1232)$ makes up a few percent of the composition of the nucleus[26, 27, 28, 29, 30]. These resonances are very short lived and their presence and role within the nuclear medium cannot be detected directly. Also the chance of Δ knockout (for example) is very slight, as it relies upon an electron interacting quasi-elastically with a pre-formed Δ. Consequently, the main approach for investigating the behaviour of resonances in the nuclear medium is by external excitation (e.g. with pion, photo, or electro-production).

On the treatment of higher resonances in this thesis

The W range relevant to the work presented in this thesis does not significantly exceed $1.5GeV/c^2$. Obviously the $\Delta(1232)$ lies within this range, beginning at the invariant mass threshold defined by the sum of the invariant masses of its decay products($1.08GeV/c^2$) and peaking at approximately $1.23GeV/c^2$. There also exist within or close to this range the $N^*(1440)$, $N^*(1520)$ and $N^*(1535)$.[1]The amplitudes of these resonances are small compared to the $\Delta(1232)$ and are considered not to contribute significantly to the results of this thesis.

[1]The notation N^* is used to denote singlet baryronic states (these have two charge states). The Δ is a triplet state and has four charge states. [31]

Table 2.2: The four charge states of the $\Delta(1232)$

isobar	quark content	charge
Δ^-	ddd	-1
Δ^0	udd	0
Δ^+	uud	+1
Δ^{++}	uuu	+2

2.3 The $\Delta(1232)$ resonance.

As stated in section 2.2, the $\Delta(1232)$ or P_{33}^+ is the first excited state of the nucleon (P_{11}^+). The $\Delta(1232)$ couples strongly to the $N\pi$ channel. This means that decay is almost invariably into the Nπ (the branching ratio for the $N\pi$ channel is about 99.9%[32] and for the purposes of this study it shall be considered 100%). Following a Δ decay, the N and π can be on their respective mass shell (real particles) or otherwise (virtual). For the $p(e, e^{'}N\pi)$ interaction the three final state particles involved are observed experimentally and hence are real. However, in the nucleus virtual particles may be involved. These manifest themselves in more complicated interactions as discussed in section 2.3.2. Due to the strong $N\pi$ coupling of the $\Delta(1232)$, the most efficient means of Δ production is with pion beams. As we are are specifically interested in the effect of Q^2 upon the properties of the $\Delta(1232)$ in the nucleus, such as its invariant mass, it is necessary to use virtual photons (from an electron beam) as opposed to real photons which are much less flexible.

2.3.1 Properties

The $\Delta(1232)$ is a triplet state made up of u and d quarks. This allows four different $\Delta(1232)$ configurations as shown in table 2.2.

The invariant mass of the free $\Delta(1232)$ has been measured to be in the region of $(1230 - 1234) MeV/c^2$, with a width of about $120 MeV/c^2$[32]. For the P_{33}^+ state the $\Delta(1232)$ has spin of $\frac{3}{2}$, an isospin of $\frac{3}{2}$, and a positive parity. In electroproduction the $\Delta(1232)$ is generally considered to be formed by an M_1^+transition meaning that the transition amplitude is determined mainly by the transverse component of the virtual photon, There is however some evidence for a longitudinal contribution to the excitation[33, 34].

The behaviour of the $\Delta(1232)$ in the nucleus can be measured in terms of its invariant mass, the width of its resonance and the magnitude of the production cross-section. These will be discussed in section 2.3.2.

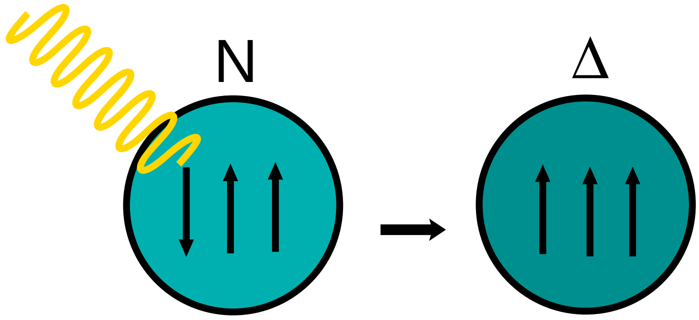

Figure 2.4: NQM Δ excitation process.
The nucleon(N) is made up of three quarks. These quarks are not aligned, leading to a vector sum of $\frac{1}{2}$. The incoming virtual photon deposits spin of 1 to the quark of spin $\frac{1}{2}$, reversing its sign. The three quark spin vectors are now aligned and their total spin is $\frac{3}{2}$, creating a $\Delta(1232)$.

2.3.2 Excitation and Decay.

Naive Quark Model

The simplest approach to understanding the electroproduction of the $\Delta(1232)$ is obtained using the naive quark model(NQM). This model depicts the nucleon as being made up of a spherical distribution of three constituent quarks in a sea of virtual $q\overline{q}$ pairs. In the NQM the total spin of the nucleon $\left(\frac{1}{2}\right)$ is the vector sum of the three constituent quarks, each of which has an intrinsic angular momentum of $\left(\frac{1}{2}\right)$. Using this model, the electroproduction of the $\Delta(1232)$ occurs when a virtual photon (of spin 1) is incident upon one of the constituent quarks. The spin of this quark is then 'flipped' leading to a system with a total angular momentum of 3/2: the $\Delta(1232)$. This process is a magnetic dipole (M1) transition, and is the only one available to the nucleon described by the naive quark model. This process is shown schematically in figure 2.4.

The resultant $\Delta(1232)$ exists in the same charge state as the target nucleon and continues to exist until it decays by way of the strong nuclear force (τ~$10^{-24}s$)[2] into a nucleon and pion (with charge conserved). This description applies to both the free nucleon and quasifree nucleons(where the nucleon in the nucleus is considered independent of the other members of the nucleus; see section 2.4.1). The decay products ($N\pi$) can interact either within the nuclear medium, or, if they escape from the nucleus, with some detector element. The total process is shown in figure 2.5. If a π^0 is produced, it is unstable, and decays electromagnetically into a $\gamma\gamma$ pair with a $\tau \sim 10^{-17}$. The two $\gamma's$ must be detected to reconstruct the four momentum of the π^0.

[2]Here τ is the mean life time of the particle.

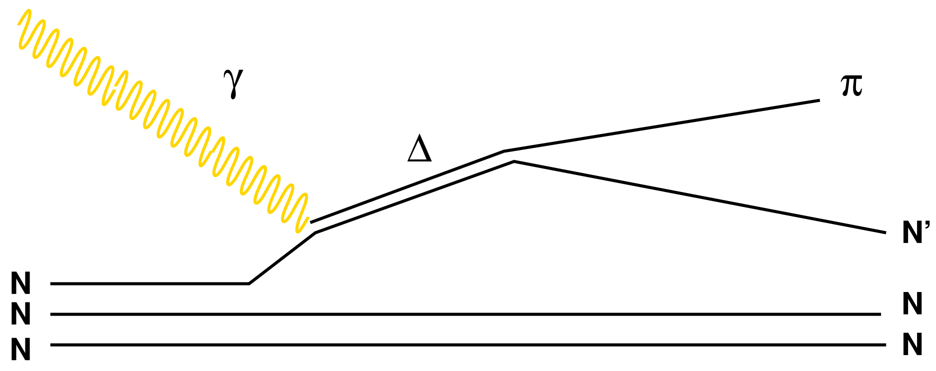

Figure 2.5: Delta excitation and decay in ^3He (Feynman diagram)
The electroproduction of a Δ on a nuclear target is shown(A=3), leading to the $\Delta's$ decay into the π and N' leaving the A-2 residual nucleus.

Medium modifications

The $\Delta(1232)$ resonance when excited from a free proton (H_2 target) behaves as described in section 2.3.1. However the behaviour of a $\Delta(1232)$ created inside a nucleus has been observed to be significantly different from the free target case. The invariant mass(W), the production cross section and the resonance width are all observed to be different [17, 35, 36].[3]

The invariant mass of the $\Delta(1232)$ in the nucleus seems to be considerably lower than for the free Δ. For Δ electroproduction on light nuclei the centroid of the $\Delta(1232)$ peak is about 10MeV lower than for hydrogen[10]. For charge exchange experiments with a pion beam, the centroid position has been observed to be around 70MeV lower than expected [38, 39]. This modification of the Δ mass may be attributed to alterations to the self energy of the Δ in the presence of the strong nuclear force[11]. The observation of Sealock et al.[17] of the variation in centroid position with Q^2 may be the result of a momentum dependent potential. This will be discussed later in section 2.4.2. However, there is always the possibility that with inclusive measurements the subtraction of the background processes mentioned in section 2.1.3 may produce the effect, and that there is no significant underlying reason for it.

The width of the W distribution for the Δ in the nucleus is also seen to be significantly different from the case of a proton target[16]. This is to be expected as the Fermi motion of the target nucleon in the nucleus will smear the distribution.

There are also additional processes which effect the width of the distribution which are only

[3]Medium modifications of the invariant mass of the pion have also been observed in electron scattering experiments on ^3He. See Kohl et al[37].

relevant in the nucleus, e.g. Pauli blocking and additional decay channels ($\Delta N \to NN$, is a major one)[40]. It is thought, however, that the effect of Fermi motion is dominant. Despite this, the observed width of the W spectrum for the Δ in the nuclear medium is notably larger than is expected from folding the elastic scattering distribution into the Δ distribution. (The width of the elastic scattering distribution is mainly due to Fermi motion, assuming the experimental resolution is sufficiently small).

The cross-section for Δ electroproduction in the nucleus is also different from that of free Δ electroproduction. This is presumably due to interaction effects between the decay nucleon and pion within the medium.

Multipole analysis

Although the naive quark model predicts a pure magnetic dipole (M1) transition for Δ electroproduction, in reality the electric (E2) or coulomb quadrupole amplitudes (C2) may also contribute[2, 41, 42]. In experiments M1 is found to be dominant with a small contribution from E2 and C2[10, 43]. More sophisticated models exist which can explain the presence of the E2 and C2 contributions. It is not the purpose of this thesis to calculate these multipole contributions, but to observe the angular distributions of the Δ decay products for signs that these multipole contributions may vary depending upon the $N \to \Delta$ charge state.

Electroproduction cross-section

The analyses of the $^3He(e, e'p\pi^-)$ and $^3He(e, e'p\pi^0)$ reactions in this thesis assume the reaction to be quasi-free and therefore follow the theoretical approach taken by Joo et al.[19]. Then the experimental electroproduction cross-section is given by equation 2.5.

$$\frac{d^5\sigma}{d\Omega_f dE_f d\Omega^*_\pi} = \Gamma \frac{d^2\sigma}{d\Omega^*_\pi} \tag{2.5}$$

where Ω_f, E_f are the solid angle and energy of the scattered (final) electron and Ω^*_π is the solid angle of the π^*. The asterisk refers to particles in the Δ centre of mass frame. Γ is referred to as the virtual photon flux[19] as expressed in equation 2.6.

$$\Gamma = \frac{\alpha}{2\pi^2}\frac{E_f}{E_i}\frac{k_\gamma}{Q^2}\frac{1}{1-\varepsilon} \tag{2.6}$$

where α is the fine structure constant, E_i and E_f are the initial and final electron energies respectively, k_γ is the 'photon equivalent energy' defined as $k_\gamma = (W^2 - M_T^2)/2M_T$, Q^2 is the 4-momentum transfer of the virtual photon and ε is the degree of transverse polarisation of the virtual photon (equation 2.7).

$$\varepsilon = (1 + \frac{2\overrightarrow{q}^2}{Q^2} tan^2(\frac{\theta_e}{2}))^{-1} \tag{2.7}$$

where $\overrightarrow{q}$ is the virtual photon 3-momentum and θ_e is the electron scattering angle in the laboratory frame. The longitudinal polarization of the virtual photon is shown in equation 2.8.

$$\varepsilon_L = (\frac{Q^2}{\omega^2})\varepsilon \tag{2.8}$$

where ω is the energy transferred by the virtual photon.

The differential cross-section (equation 2.9)for an unpolarised beam incident upon an unpolarised target depends upon ε, ε_L and four structure functions: σ_T, σ_L, σ_{LT} and σ_{TT}[19].

$$\frac{d\sigma}{d\Omega^*_\pi} = \frac{p^*_\pi}{k^*_\gamma}(\sigma_T + \varepsilon_L\sigma_L + \varepsilon\sigma_{TT} sin^2\theta^*_\pi cos2\phi^*_\pi + \sqrt{2\varepsilon_L(\varepsilon+1)}\sigma_{LT} sin\theta^*_\pi cos\phi^*_\pi) \tag{2.9}$$

where p^*_π is the magnitude of the π momentum and k^*_γ is the magnitude of the momentum transferred by the exchanged virtual photon.

It is not possible to separate σ_T from σ_L using only one beam energy. However as CLAS allows out of scattering plane measurements of θ^*_π and ϕ^*_πit is possible to separate σ_{LT} and σ_{TT}. The angles θ^*_π and ϕ^*_π are defined as shown in figure 2.6.

$\theta^*$and $\phi^*$are defined relative to the virtual photon, such that the polar angle θ^* is deduced from the dot product of the momenta of the virtual photon and the outgoing pion. The azimuthal ϕ^* angle is measured relative to a vector perpendicular to the electron scattering plane(in the Δ rest frame). This perpendicular vector is calculated as the cross-product of the scattered electron and the virtual photon (in the Δ rest frame). Therefore both θ^* and $\phi^*$are defined with respect to the Δ rest frame. The virtual photon 3-vector is parallel to the z-axis, the vector perpendicular to the scattering plane is parallel to the x-axis and the y-axis lies in the electron scattering plane.

The determination of σ_T, σ_L, σ_{LT} and σ_{TT} provides information about the multipole composition of the $N \rightarrow \Delta$ transition form factor[44, 43]. The aim of this thesis is not to determine these multipoles, but to compare the structure functions arising from the $^3He(e, e'p\pi^-)$ and the $^3He(e, e'p\pi^0)$ reaction. Any difference will be due to the channels being studied, shedding light upon the natures of the $\gamma + p \rightarrow \Delta^+$ and $\gamma + n \rightarrow \Delta^0$ transitions and the differences between them. Significant differences between the proton and neutron structure functions would be of interest as the proton and neutron are usually treated as identical but

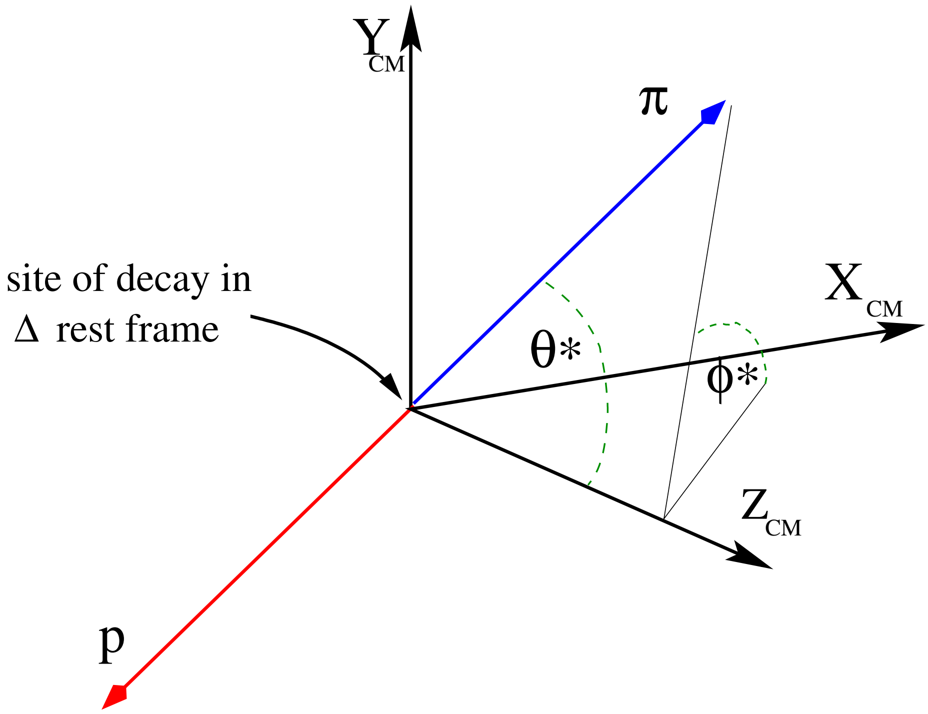

(a) polar and azimuthal angles relative to centre of mass angles

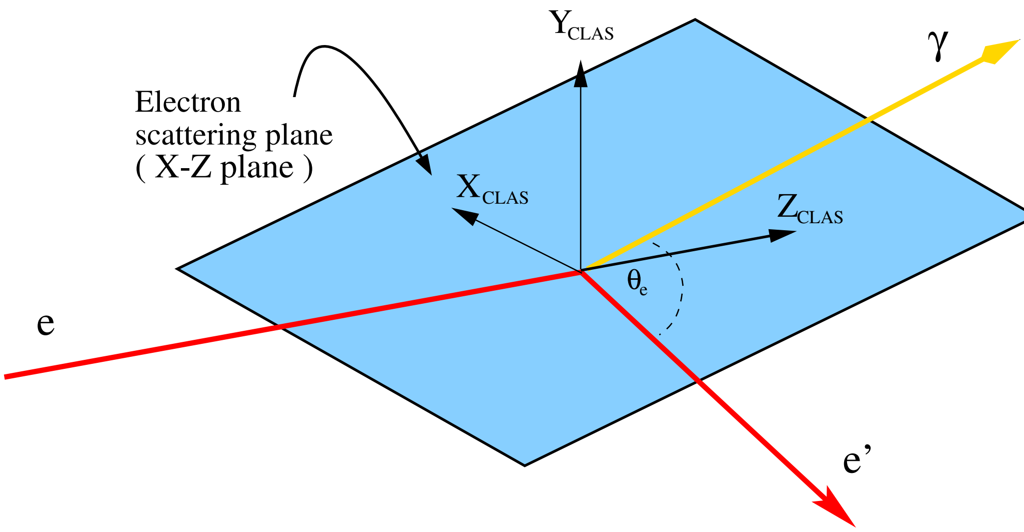

(b) electron scattering relative to the lab angles defined in CLAS

Figure 2.6: Rest frame axes and angles defined.
The angles $\theta^*$and ϕ^* are defined relative to the Z_{CM} axis as shown above (top figure). This Z_{CM} axis along with the X and Y axes are defined relative to the electron scattering plane (shown below), with the exchanged virtual photon parallel to the Z_{CM} axis and the Y_{CM} axis normal to the electron scattering plane. The beamline is defined as the Z_{CLAS} axis in the lab and the electron scattering angle in the lab (θ_e) is shown.

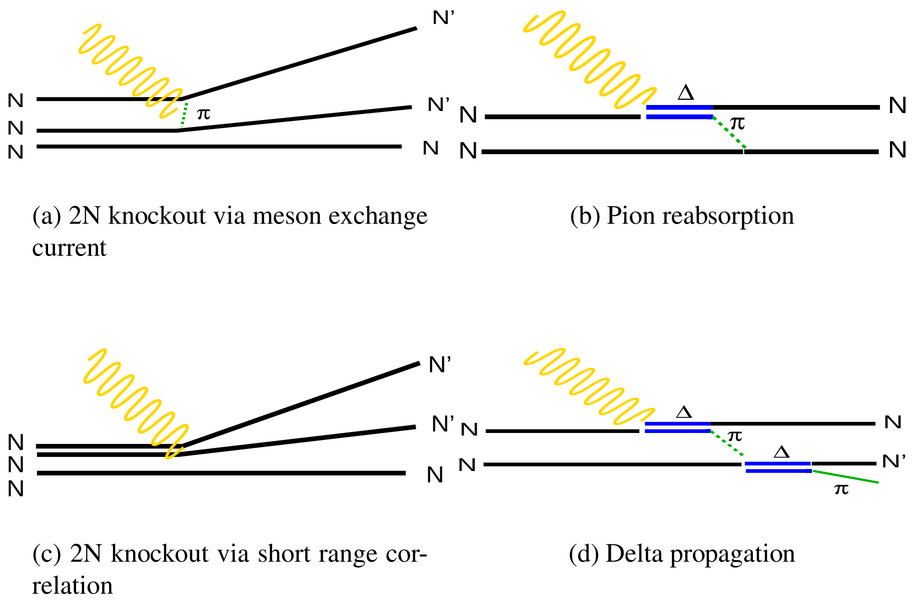

Figure 2.7: Feynmann diagrams for Δ electroduction in the the ^3He nucleus.

for their charge. The $^3He(e, e'p\pi^0)$ channel may also be compared qualitatively with the $(e, e'p\pi^0)$ reaction on a free proton (see reference [43]).

2.4 The ^3He Nucleus.

This work is concerned with the effect of the nuclear medium upon the electroproduction and decay of the $\Delta(1232)$ resonance in ^3He. Furthermore the excitation process is considered to be quasi-free. This means that much of the analysis is general and can be applied to any nucleus or indeed to a free nucleon. What follows is a brief description of the quasi-free process, the ^3He nucleus and factors peculiar to the ^3He target.

2.4.1 Quasi-free excitation.

As mentioned above, in 2.3.2 the behaviour of the nucleon and its resonances is modified by the nuclear environment. A complete theoretical treatment would have to include six quark and three quark states etc. However, it is reasonable to restrict the virtual photon interactions to those described by the Feynmann diagrams shown in figure 2.2. There are also processes arising from the additional nucleons in the nucleus and the pion field generated by the nucleus. The most significant of these additional processes are shown in figure 2.7.

These include 2-nucleon knockout either as a result of meson exchange currents or short range correlations. There is also the possibility that the decay products of the nucleus will be reabsorbed into the nucleus leading to either Δ propagation or other resonances. Despite the presence of the interactions shown in figure 2.7, the dominant processes are quasi-free. These quasi-free processes are where only one nucleon participates in the reaction, leaving the other nucleons as spectators. These lead to Feynmann diagrams similar to those of figure 2.2 but with A-1 spectators present. An example of this is shown in figure 2.5, which is the process shown in figure 2.2(c) taking place in ^3He.

2.4.2 Momentum dependent potentials

One of the three areas covered in this thesis is a study in the variation of the potential experienced by a particle in the ^3He nucleus as a function of the particle momentum. More particularly it is the difference in the potential experienced by a particle immediately before and after it is struck by the virtual photon. Specifically two cases are studied. The first is for the $^3He(e,e'p)$ channel, where the change in the proton-Nucleus potential (dV_N) is calculated. The second is for the channel $^3He(e,e'p\pi^-)$, where a quantity dV_Δ is calculated. dV_Δ is the difference between the potential experienced by the neutron in the ^3He nucleus and that experienced by the Δ^0 while in the nucleus. What follows is a definition of these terms and the approach taken to calculate dV_N and dV_Δ.

If a bound nucleon with momentum $\underline{p}$ experiences a momentum dependent potential $V_N(p)$ then its total energy is shown in eqn 2.10.

$$E = (p^2 + M^2)^{\frac{1}{2}} + V_N(p) \tag{2.10}$$

Where E is the total energy of the nucleon and M is the mass of the nucleon.

If a state of invariant mass W is created during an electron scattering event where energy(ω) and momentum($\underline{q}$) is transferred, then ω, which is the difference in the total energy of the final state from the initial state, is such that $\omega = E_i - E_f$. (The final state referred to here is the state that exists after the nucleon is struck and is not the same as the final detected state. The subscripts 'i' and 'f' will refer to the states immediately before and after the interaction with the virtual photon) This means that ω may be expressed in terms of eqn 2.10, as shown in eqn 2.11.

$$\omega = [(p_f^2 + M_f^2)^{\frac{1}{2}} + V_{W(p_f)}] - [(p_i^2 + M_i^2)^{\frac{1}{2}} + V_{N(p_i)}] \tag{2.11}$$

where $\underline{p_f}$ is defined in eqn 2.12.

$$\underline{p_f} = \underline{p_i} + \underline{q} \tag{2.12}$$

V_N and V_W are the real parts of the momentum dependent potentials felt by the nucleon and recoil hadron, respectively. For the $^3He(e,e'p)$ channel, M_i = nucleon invariant mass, for the $^3He(e,e'p\pi^-)$ channel the centroid position of the invariant mass peak is approximately $W = 1.232 GeV/c^2$, however for any given event the detected invariant mass will lie within the $\Delta(1232)$ invariant mass distribution. The implications of this are discussed further in section 4.6.

p_i is derived from the Fermi motion of the bound nucleon. An average is used such that $\langle p_i^2 \rangle = \frac{k_F^2}{2}$, where $k_F \approx 200 MeV/c$ is the Fermi momentum.

Based on equation2.11, we can then calculate the difference in the potential between the initial and final states ($\delta V_{(e,e'p)} = V(p_f) - V(p_i)$ shown in equation 2.13 and $\delta V_{(e,e'p\pi^-)} = V(p_\Delta) - V(p_i)$ shown in equation 2.14).

$$\delta V_{(e,e'p)} = \omega - (p_f^2 + M_f^2)^{\frac{1}{2}} + ((k_F^2/2) + M_i^2)^{\frac{1}{2}} \tag{2.13}$$

$$\delta V_{(e,e'p\pi^-)} = \omega - (p_\Delta^2 + M_\Delta^2)^{\frac{1}{2}} + ((k_F^2/2) + M_i^2)^{\frac{1}{2}} \tag{2.14}$$

where $p_\Delta$is the reconstructed momentum of the excited Δ and $M_\Delta$is the invariant mass of the excited Δ.

Any non-zero value of $\delta V_{(e,e'p)}$ will mean that some momentum dependence of the nucleon-nucleus potential exists. However it may be of greater significance if the behaviour of the two channels, display a systematic difference between $\delta V_{(e,e'p)}$ and $\delta V_{(e,e'p\pi^-)}$. This would result from a different momentum dependent potential being experienced by a proton and Δ^0 inside the ^3He nucleus. It should be noted that the two channels cannot be compared directly as the $^3He(e,ep\pi^-)$ reaction involves a $n \rightarrow \Delta$ transition whereas the $^3He(e,e'p)$ channel refers to quasi-elastic scattering from a proton in ^3He.

2.4.3 ^3He

^3He is a stable nucleus consisting of two protons and a neutron. Although the spatial resolution of the incident virtual photons means that the interaction is predominantly with a single nucleon, the presence of the two spectator nuclei in the ^3He nucleus must be taken into account in the course of the data analysis.

Although ^3He is stable with a binding energy of approximately 8 MeV per nucleon, the virtual photon energies used in the present experiment mostly lead to the break-up of the nucleus into three nucleons.

In the event of quasi-free excitation, the target nucleon either leaves behind 2 protons ($^3He(e,ep\pi^-)pp$) or an np pair ($^3He(e,ep\pi^0)pn$). The pp pair is unbound and the np pair is only very weakly bound (2.2MeV). This means that the spectator nucleons are liable to be incident upon the detector.

However since there is a relatively high momentum threshhold (approximately 200MeV/c) for detecting particles in CLAS, for quasi-free interactions the spectator nucleons are not energetic enough to register in CLAS. However, the proton from either $(\Delta^0 \rightarrow p\pi^-)$ or$(\Delta^+ \rightarrow p\pi^0)$ will in general have sufficient momentum to be detected. Furthermore, in the present experiment, since the typical momentum of the virtual photon is only a few hundred MeV/c, if the interaction is not quasi-free and the momentum is shared amongst the nucleons, then it is probable that they will not all be above threshhold.

Hence, it is assumed that an event which has a fairly high energy proton in coincidence with a pion probably results from the quasi-free interaction $^3He(e, e'p\pi^-)pp$ or $^3He(e, e'p\pi^0)pn$.

Chapter 3

Experiment

The data presented in this thesis were collected at the Thomas Jefferson National Accelerator Facility (JLab.) using the Continuous Electron Beam Accelerator Facility(CEBAF) and the CEBAF Large Acceptance Spectrometer(CLAS)[45], housed in JLab's Hall B. Unpolarised electrons of energy 1.162 GeV were incident upon a liquid ^3He target leading to the excitation of the $\Delta(1232)$ resonance within the nucleus among other reactions. The decay products of the $\Delta(1232)$ were then detected in the CLAS detector array. Due to the large acceptance and good particle identification of CLAS many experiments were carried out simultaneously. The experiment described here was carried out in 1999 by the e2 run group of the CLAS collaboration. The experiment used a variety of beam energies and detector configurations. What follows is a brief description of the apparatus used to record the events described above. The main components are the CEBAF accelerator, the CLAS detector array and the liquid ^3He cryotarget. A brief overview is then given of the experimental configuration used to collect the present data, the calibration of CLAS and some of the necessary corrections to the data.

3.1 Beam

JLab consists of CEBAF, an electron accelerator facility based on two sets of linear accelerators (LinAc's) in a racetrack configuration as shown in figure 3.1. Electrons are accelerated through each Linac, made up of 20 cyro-modules each containing 5 RF cavities and then turned through 180^o by bending magnets to be accelerated again by the other set of RF cavities. This continues until the desired energy is reached.

Electron bunches are produced when a laser pulse is incident upon a photo-cathode which results in polarised electrons of initial energy 0.062 GeV. At the time of the 1999 run each LinAc accelerated the beam by 0.55 GeV, providing beam energies incrementing by

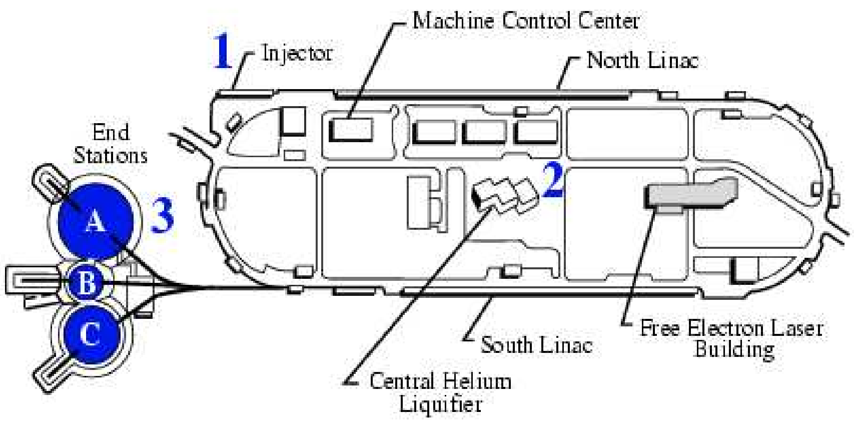

Figure 3.1: Plan view of the JLab experimental area.

1.1GeV, the bending magnets providing an upper limit of 5.562 GeV. The beam is then split to provide electrons to the three experimental halls. Due to the high acceptance of CLAS, Hall B requires significantly lower beam currents than Halls A and C.

The Beam recirculator separates and recombines the different energy electrons so as to cater for this and provide beams of different energies and currents to each hall simultaneously.

3.2 CLAS

CLAS (figure 3.2) is made up of six almost identical sectors built around a superconducting toroidal magnet. A cross-section of CLAS is shown in figures 3.3, clearly showing the various elements.

Nearest to the target are the Drift Chambers (DC) which allow tracking of charged particles. Next are the Cerenkov Counters(CC) which are used to discriminate between electrons and π^-s. The Scintillation Counters (SC) provide a large fraction of the angular coverage and allow time of flight (TOF) measurements. At the outside, near the beam line is the Electromagnetic Calorimeter (EC) which allows accurate energy and position measurements. The Large Angle Calorimeter(LAC) (which is only present in sectors 1 and 2) next to it plays a similar role at angles further from the beam line. Each of these segments will be discussed in more detail below. Hall B also houses photon tagging facilities to cater for real photon experiments.

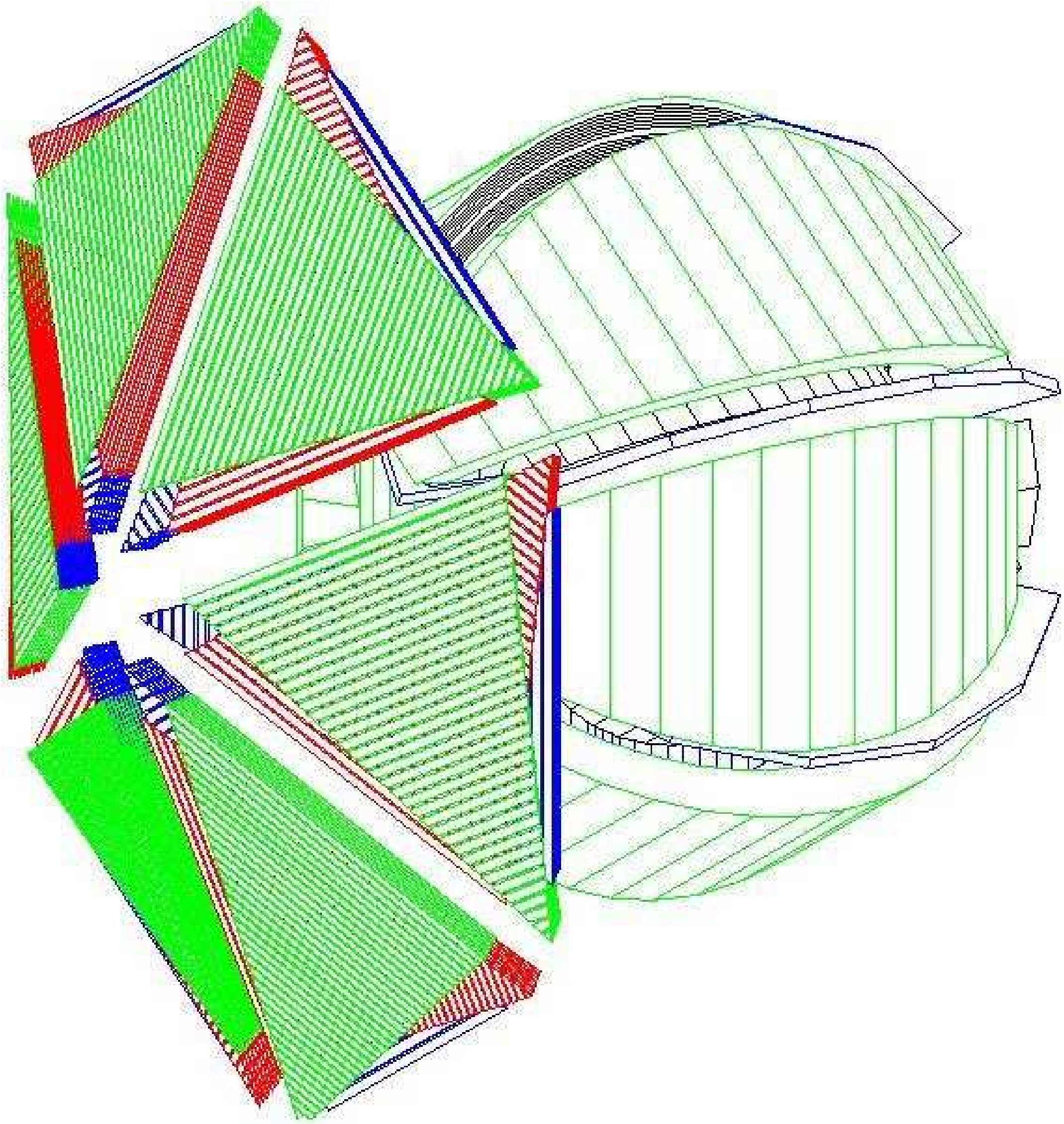

Figure 3.2: The CLAS detector array(exploded).

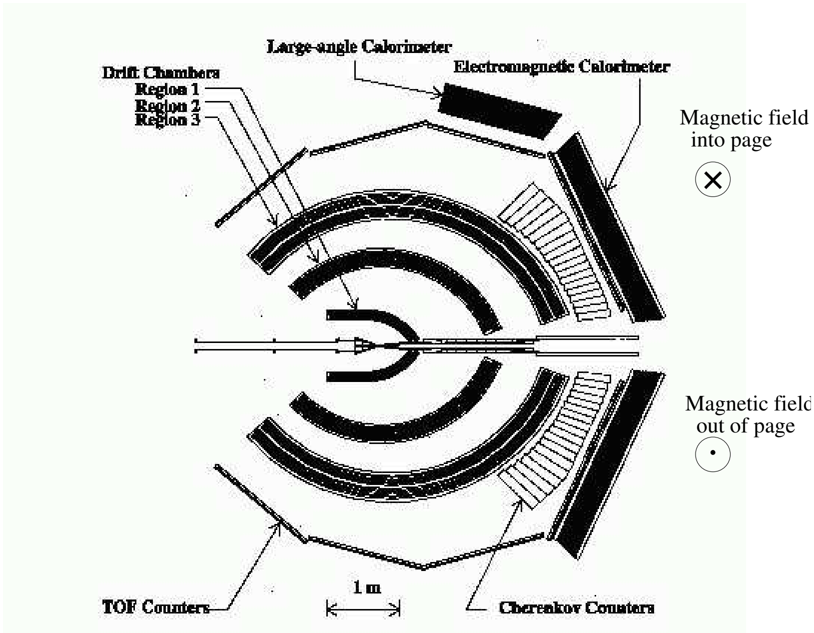

(a) CLAS cross section (side view)

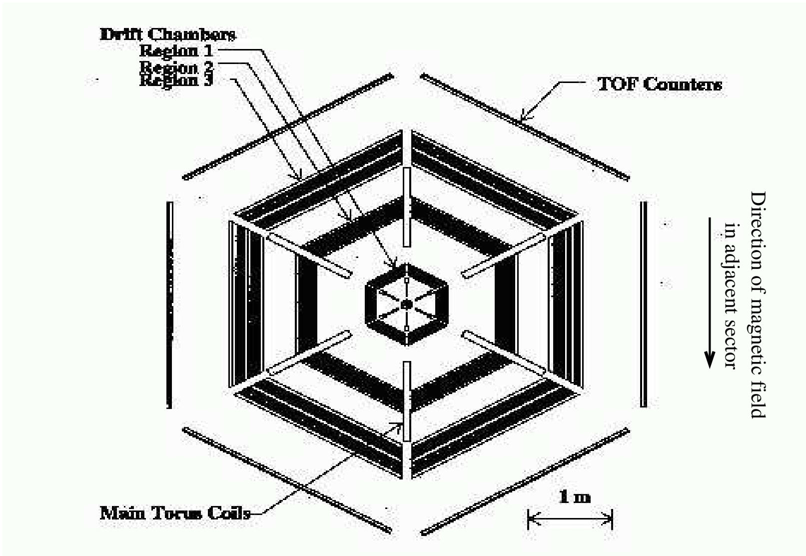

(b) CLAS cross section (front view)

Figure 3.3: The CLAS detector array (cross-sections).
Also shown are the direction of the toroidal magnetic field. In the top figure the field is coming out of the page at the bottom and back into the page at the top. In the bottom figure the field points in a clockwise direction (here the arrow shows the direction of the field in the sector directly adjacent to the arrow).

Figure 3.4: CLAS toroidal magnet (side view).

3.2.1 CLAS magnets

The CLAS superconducting magnet creates a forward peaked toroidal field. The integrated product (field x trajectory length) reaches a maximum of 2.7 Tm in the forward angles and decreases to 0.5 Tm towards the rear. The magnet is designed such that the field is near zero at the target and region 1 of the drift chambers(see drift chambers below), and reaches its peak in region 2 of the drift chambers. The magnet is built in six flat sections radiating from the beam line (fig 3.4) so as to reduce the obstruction to outgoing particles. Due to the toroidal field produced, particle trajectories are bent relative to the beamline, so that their phi distribution is unaltered. This also reduces the obstruction of the magnet to outgoing particles.

There is also a smaller magnet near the target which removes low energy atomic electrons (Moeller electrons). This is used to reduce background and has no significant effect on the measurements.

3.2.2 DC - Drift Chambers

Tracking in CLAS is provided by the Drift Chambers. This tracking is essential for identifying events and for assigning momentum to particles. From the track of a charged particle in a drift chamber it is possible to estimate its momentum by referring to the field map of the CLAS toroid. As this field map is not precisely defined, momentum corrections are necessary. These corrections will be discussed later(see section 3.4.2).

As described earlier(see section 3.2.1) CLAS is constructed to allow free passage of particles within the volumes of CLAS between the six arms of the toroid. For these volumes, as with the rest of CLAS, the tracking system is made up of six identical sectors. Each sector contains three gas filled multi-wire drift chambers (see figure 3.3), each consisting of two layers (superlayers). All the sectors are similar in design and construction, and are treated as being identical (for more details see reference [46, 47]). A photograph of one of the sectors, with an explanatory diagram, is shown in figure 3.5, with the placement within the toroid shown in figure 3.6.

Each drift chamber is made of one super-layer with wires perpendicular to the beam line (and also roughly perpendicular to the plane of the curved path of a charged particle to improve sensitivity to the momentum of the particle) and another superlayer with wires at 6^o to the first layer to provide some azimuthal information. The wires (almost 130,000 in total) are arranged in a pattern which subdivides the total volume of a layer into hexagonal prisms (see fig 3.7). The prisms are arranged six deep and each is centred on a sense wire. There are over 35,000 hexagonal drift cells in total. The gas used is a 90% argon -10% CO_2 mixture. The distance of closest approach (DOCA) of a charged particle to the sense wire is recorded for each cell, and later during the data analysis (see section 3.4.2) these DOCA's are combined for each super layer and tracks are reconstructed for the charged particles. An uncharged particle does not interact in the DC's, its energy is measured in the EC and LAC, and time of flight information is provided by the SC. The only uncharged particles used in this thesis are $\gamma's$ (from the decay of a π^0).

3.2.3 CC - Cerenkov Counters

The CLAS Cerenkov counters[48]. are situated at the front of CLAS(see figure 3.3). CC coverage is in all six sector with a solid angle coverage similar the EC. The CC's are primarily used to discriminate between electrons and negative pions, and are often included in triggering events at low(1.1GeV and 2.2GeV) beam energies. Discrimination is only possible at lowish momenta as the CC does not discriminate between particles over 2.7 GeV/c. All the particles measured during the 1.1 GeV beam running had momenta well below this.

The CC is made up of six identical segments, each lying within one of the CLAS sectors. Each is split into 18 sections in polar angle. Each section is split in half creating two sub-sectors providing equal azimuthal angle coverage (see figure 3.8). The sections are identical for any given value of theta, and each sub-sector is a mirror image of its partner.

The sub-sectors are designed so that light created from any charged particle will be directed into PMT's which lie within the shadow of the magnet, so as to increase the available solid angle of the detector. This mirror arrangement is shown in figure 3.9.

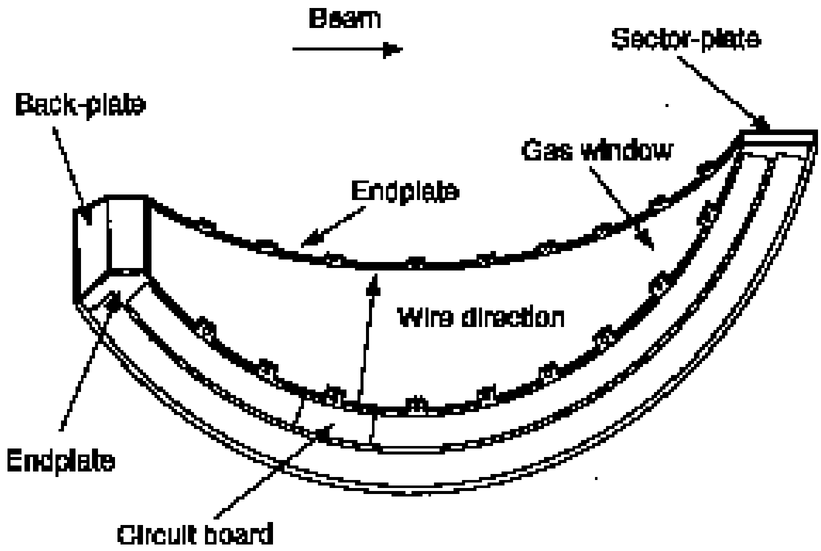

(a) CLAS drift chamber

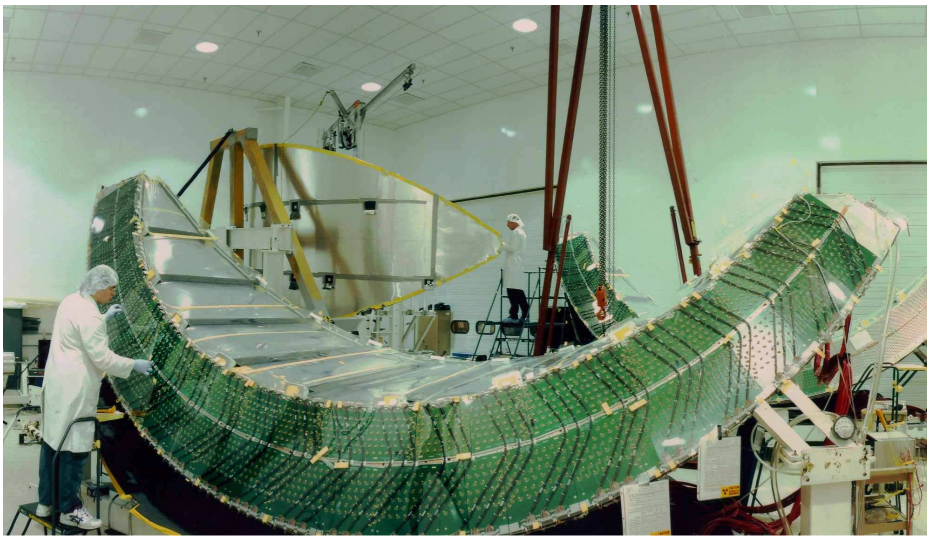

(b) CLAS drift chamber during construction

Figure 3.5: CLAS drift chambers.

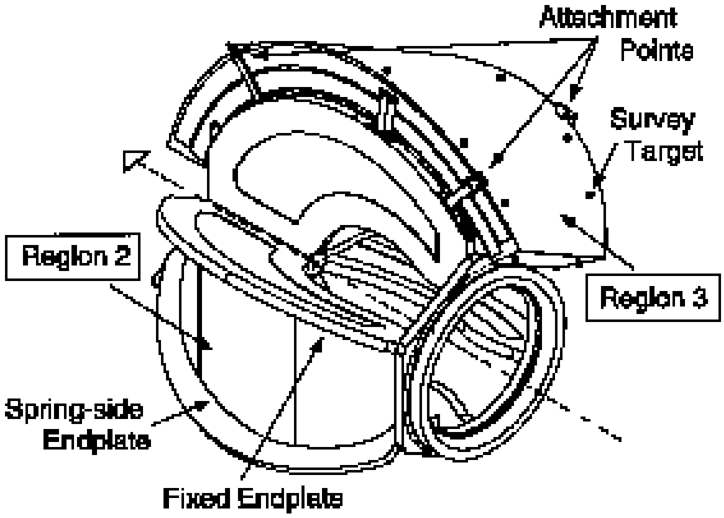

Figure 3.6: CLAS DC installation.

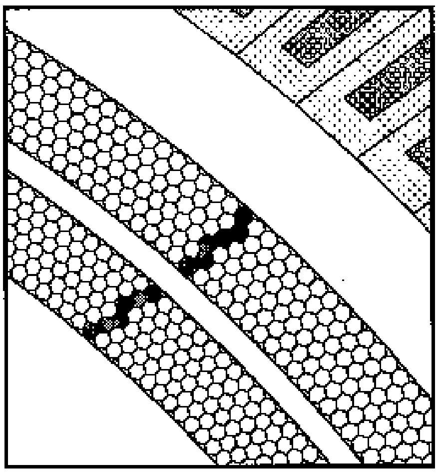

(a) region 3 showing reconstructed track

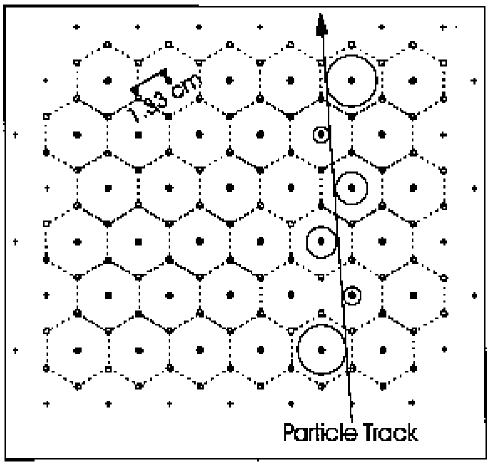

(b) track reconstruction in the drift chamber

Figure 3.7: CLAS DC layout

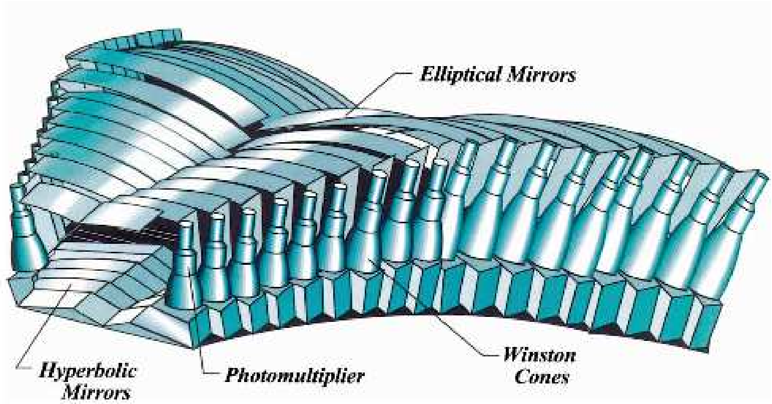

Figure 3.8: CLAS CC Optical mirror system

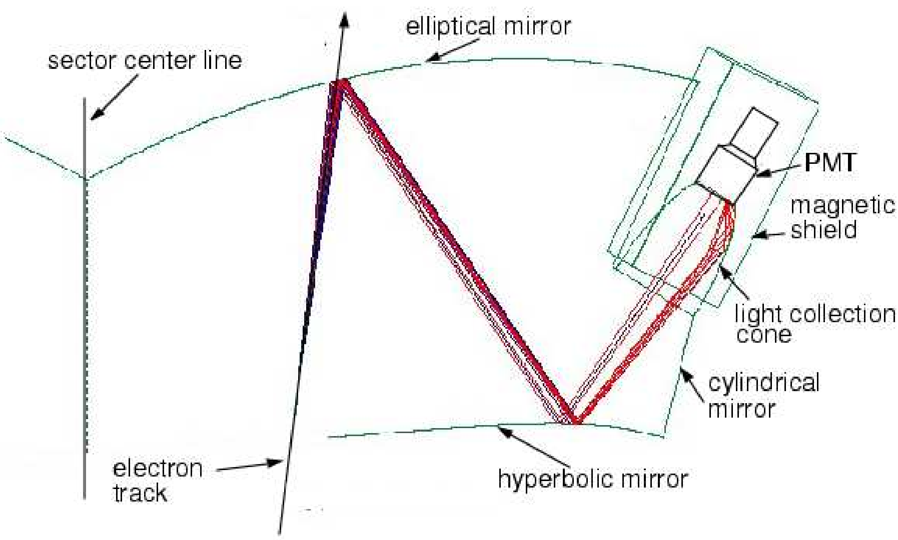

Figure 3.9: CLAS Cerenkov counter mirror setup

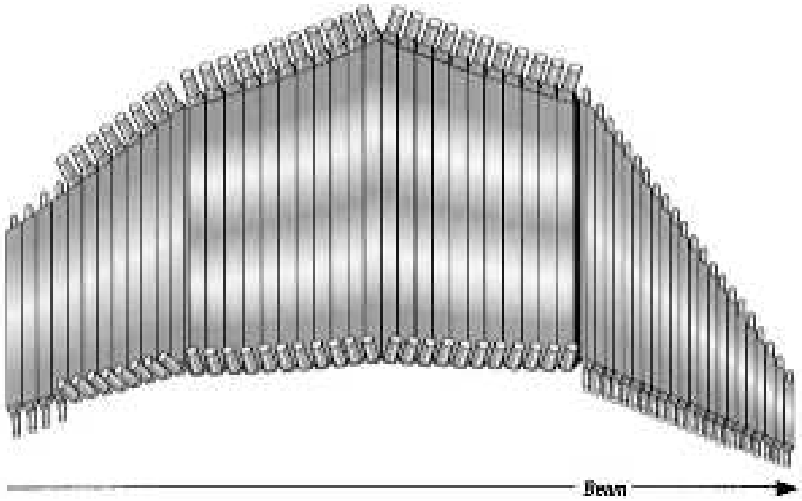

Figure 3.10: CLAS Time of flight layout

3.2.4 SC - Scintillation Counters

The majority of the solid angle coverage of CLAS is provided by its time of flight system[49]. As shown in figure 3.2 and figure 3.3 CLAS is almost completely covered (but for the gaps caused by the magnet coils and the gaps around the beam-line in the forward and backward directions.) by panels of scintillator. Each panel is 5cm thick, and varies in length between about 32cm and 445cm. At front and back, the panels are 15cm wide, and 22cm wide in the middle. There are 57 scintillators per sector. The forward most 39 have a PMT at each end, with the rear 18 paired together to give a total of 48 separate output signals. Polar angular resolution depends upon the width of these scintillator panels, whereas the azimuthal resolution comes from the time difference between signals reaching the two PMT's. Position measurement is also provided by the drift chambers. The scintillator layout for one sector is shown in figure 3.10.

The timing resolution of the TOF panels varies between 60ps and 160 ps. Average values of about 140 ps have been obtained for the whole TOF system.

3.2.5 EC - Electromagnetic Calorimeter

As seen in figure 3.3, the electromagnetic calorimeter covers the forward angles ($8^o < \theta < 45^o$) and is divided among the six sectors of CLAS. The EC is made up of a total 39 layers of plastic scintillator and lead. These layers are made up of 36 strips of plastic scintillator (10 cm wide) of increasing length from the beam line so each is roughly triangular in shape (see fig 3.2). Each adjacent layer is rotated by 60^o relative to the previous one.

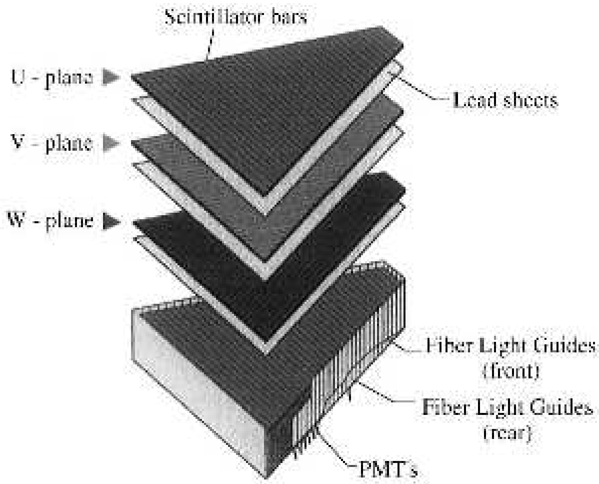

Figure 3.11: CLAS EC exploded.
The electromagnetic calorimeter consists of consecutive layers of lead and glass scintillator. Each adjacent lead glass pair of sheets is rotated by 60^o producing three axes (the U, V and W axes). Using these position measurements are made.

The different orientations of scintillator bars are labeled U, V and W as shown in figure 3.11. The orientation of these U,V and W layers then create triangular pixels (of side length 10cm) for spatial resolution.

Parallel strips are then lead to a light guide which combines the signals. Then the innermost 5 and the outermost 8 are fed to separate PMT's. This maintains the θ and ϕ resolution and creates an inner and outer layer in the EC, which is a useful feature for particle identification.

3.2.6 LAC - Large Angle Calorimeter

The LAC[50] performs a similar role to the EC but is situated further back and exists only in 2 sectors. Its construction is also similar to the EC but is rectangular with a series of perpendicular layers providing θ and ϕ coordinates(see fig 3.12).

3.3 Target

The ^3He target used for this experiment was housed in a cryo-target built by the Saclay Nuclear Physics group. The ^3He was cooled to approximately 3K and was kept at a density which has been independently calculated at $0.064 g/cm^3$ and $0.067 g/cm^3$. The target length is 3cm. For the purposes of calculating a cross section (see section 4.7) the average value of target density is used.

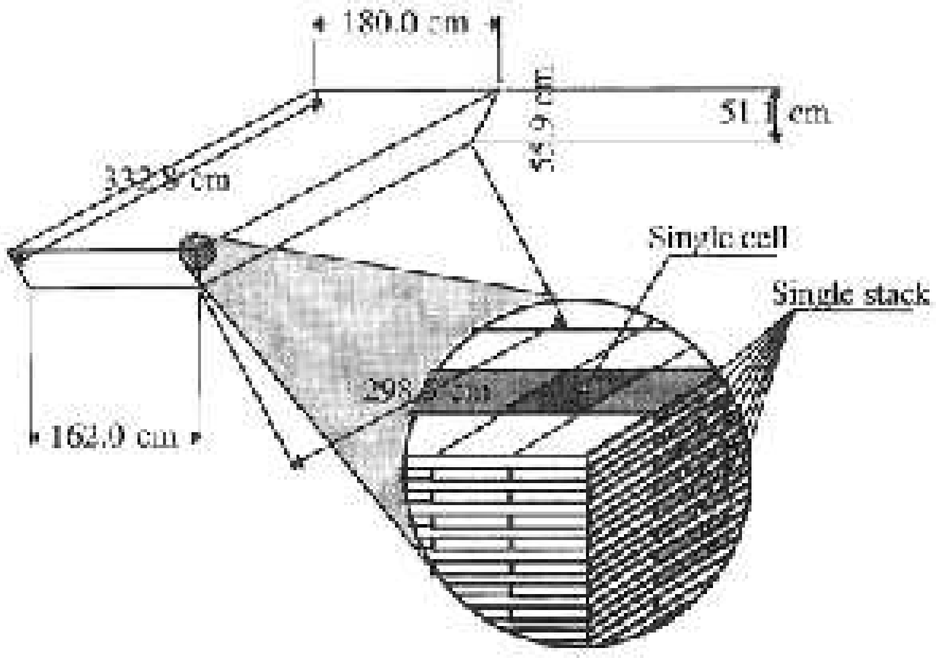

Figure 3.12: CLAS LAC figure

3.4 Experimental run

3.4.1 Run conditions

In order to gain the best possible statistics for the Q^2 range of interest to us ($Q^2 < 0.5$ GeV/c^2) the CEBAF beam energy was set at 1.162GeV. The beam current was set at approximately 5 nA to keep the dead time in the CLAS acquisition system to below 10%. Typical counting rates were about 1500 triggers per second.

The CLAS superconducting toroid current was set at both 750 Amps and 1500 Amps, collecting two separate data sets. However, the analysis discussed in this thesis is only applied to the 1500A data.

The trigger used for these measurements required an electron to be identified in both the EC and CC. This restricted electron measurements to within the coverage of the EC and CC, but the lost electrons make a negligible contribution to the scattering cross section. The LAC was not used at any stage in the analysis described in this thesis.

Data relevant to this thesis were collected during 2 days of the e2a run amounting to approximately 130 Million triggers. This figure is reduced considerably by the cooking process and fiducial cuts.

3.4.2 Cooking, Calibration and Corrections.

After the completion of the experimental run, the data are in the form of ADC values (raw data). In the "cooking" process is where these ADC values are used to reconstruct the particle tracks, time of flight measurements and energy deposited in each detector element. This information is then used to discern individual particles, assigning each a particle identity, momentum and energy. It is in this cooked form that physics information is extracted from the data.

The result of this cooking procedure depends upon the calibration of the CLAS detectors. CLAS is calibrated at the end of every run period. In the absence of any serious breakdown the calibration constants will vary smoothly from run to run.

The first cooking (pass zero) of the raw data uses the calibration constants from the previous experimental run. The pass zero cooked data are then used to calibrate CLAS throughout the run period. Responsibility for calibrating each of the detector sections is assigned to members of the run group. I was involved in calibrating the LAC.

The momentum allocated to charged particles depends upon their path through the magnetic field of CLAS. This means that any deviation from the true magnetic field from that assumed during cooking will give incorrect particle momenta. The electron, having such a low mass, is the particle most affected by these deviations. The magnetic field assumed for cooking does deviate from the true magnetic field and momentum corrections must be carried out after the data are cooked. For the $1.1GeV$ beam energy these corrections were carried out by Steven McLauchlan of the Glasgow Group as described in reference [51].

3.4.3 Fiducial cuts

Although CLAS is built in six sectors to minimise any interactions between the toroidal magnet and outgoing particles, the magnets do have an effect upon the geometrical acceptance of CLAS. Events which enter areas around the edge of the detector sectors, close to the magnets are removed. This is referred to as a fiducial cut. Fiducial cuts for the $1.1GeV$ run period were carried out by Steven McLauclan of the Glasgow group as described in reference [51]. The fiducial cuts used as described in ref [51] are shown below. Figure 3.13 shows an example of the region accepted by the electron fiducial cut (taken from [51]). Figure 3.14 shows examples of the hadron fiducial cuts used[52]. These hadron fiducial cuts applied the the proton (the positive hadron cut) and the π^-(the negative hadron cut). The fiducial cut used for the detected photons were carried out by myself using a cut on the θ vs. ϕ distribution (as shown in figure 3.15).

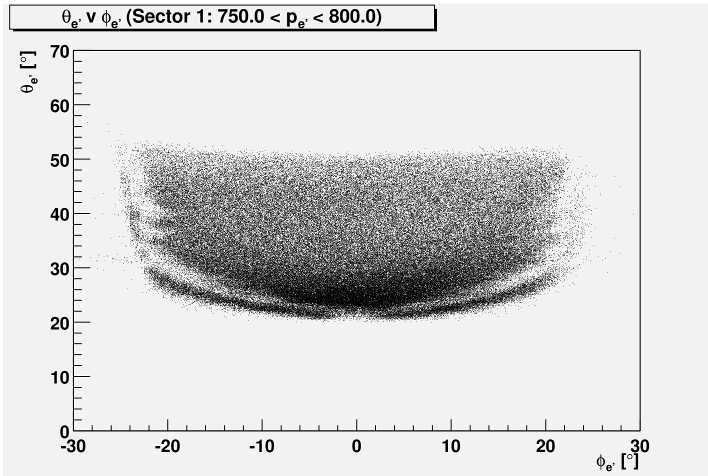

(a) Angular distrinbutions of detected electrons in sector 1 (no fiducial cut applied)

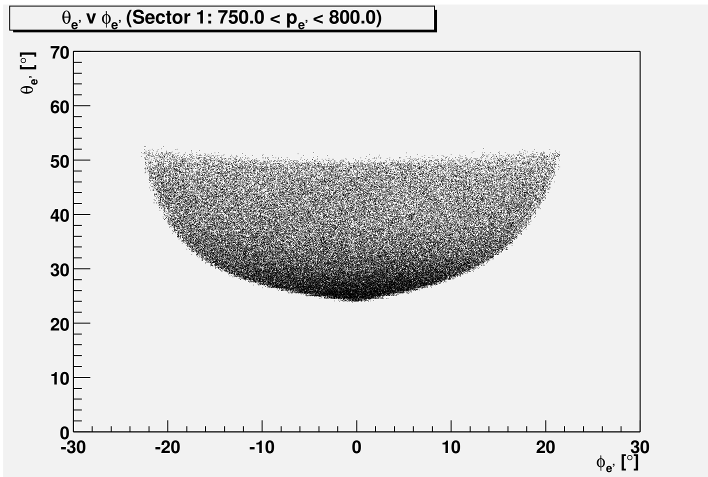

(b) Angular distrinbutions of detected electrons in sector 1 (fiducial cut applied)

Figure 3.13: Regions of sector 1 of CLAS accepted in electron fiducial cut. As is clear the areas at the extremities (which correspond to areas close to the toroid, where the acceptance of CLAS is not reliable) are removed by the electron fiducial cuts, as is the feature at low $\theta_{e'}$ which is caused by the CC.

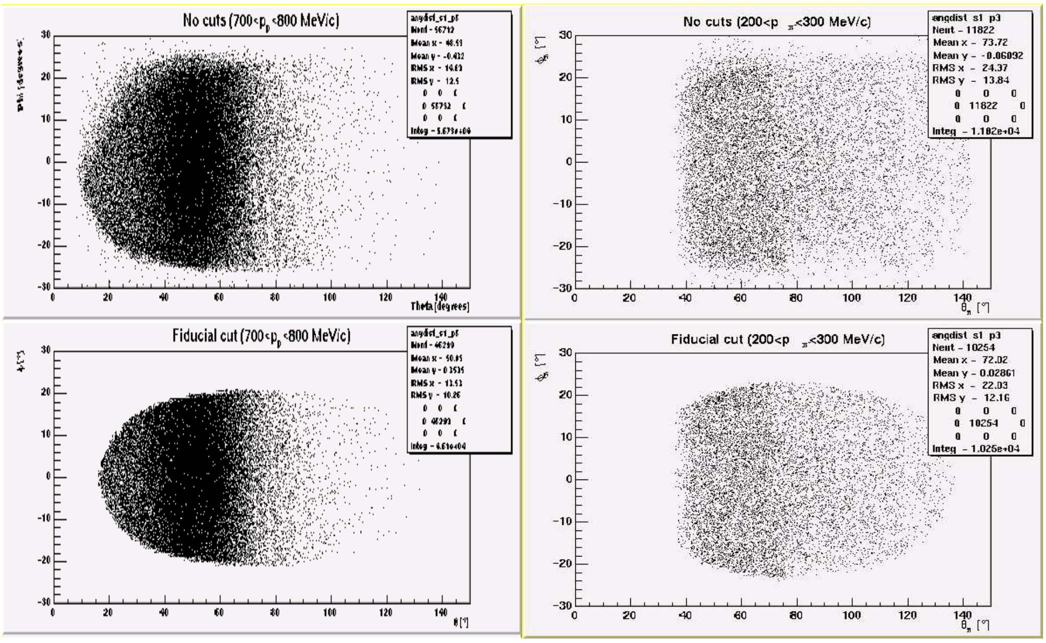

(a) Positive hadron fiducial cut.

(b) Negative hadron fiducial cut.

Figure 3.14: Examples of the charged hadron fiducial cuts.
Figure a.) shows the positive hadron cut for protons with momentum of between 700 and 800 MeV/c. Figure b.) shows the negative hadron fiducial cut for π^-'s with momentum of between 200 and 300 MeV/c.

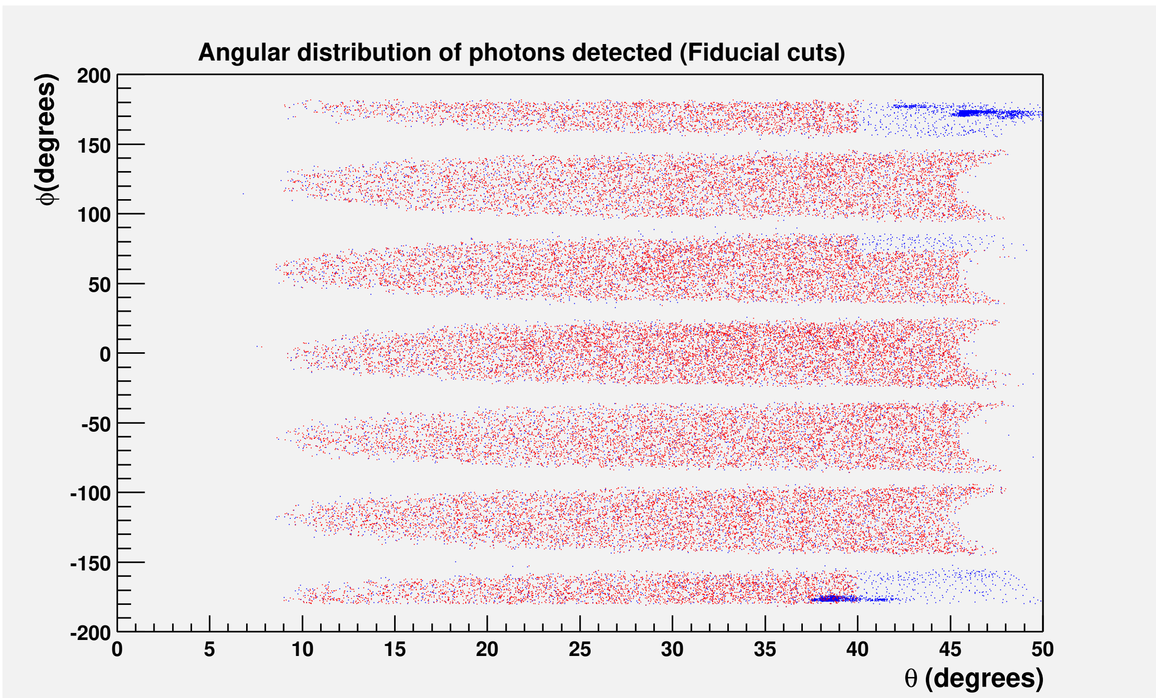

Figure 3.15: Photon fiducial cuts.
Shown above is the simple geometrical cut used for the photon fiducial cut. The main effect of these cuts were to avoid unreliable areas of the CLAS. The underlying blue shows the distribution with no fiducial cuts and the red is the region accepted by the fiducial cut.

Chapter 4

Analysis

What follows is a description of the analysis carried out on the cooked data that were collected from the e2a run as described in chapter 3. First, some basic data selection techniques are described, and unless stated otherwise, these are applied to all the relevant data. They are cuts on the missing energy, missing momentum and the opening angle between the virtual photon and reconstructed Δ. Next, the approach taken to compensate for the geometric acceptance of CLAS is outlined. The measures taken to make theoretical MAID calculations relevant to the current data set are then presented. Following this is a description of the analysis appropriate to each of the three main sections of the thesis. These are the Q^2 dependence of the invariant mass distributions of the $\Delta(1232)$ resonance, the momentum dependence of the proton-nucleus and $\Delta(1232)$-nucleus potential, and the azimuthal distributions of the decay products of the $\Delta(1232)$ in the $\Delta(1232)$'s rest frame.

4.1 Data selection techniques.

4.1.1 Missing momentum and energy cuts.

Since energy and momentum are conserved, for every event the total energy and momentum of the incoming and outgoing particles must be the same. Furthermore, a very basic and straightforward way of checking the quality of an event and our understanding of it, is to determine if there is any energy or momentum missing.

Missing energy and momentum can be extracted from the missing 4-vector ($p_{Missing}$) as defined in equation 4.1.

$$p_{Missing} = \gamma + T - (N + \pi) \tag{4.1}$$

Channel	Accepted Missing Energy Range	Accepted Missing Momentum Range
$^3He(e,e'p\pi^-)$	-0.01 - 0.04 GeV	-0.01 - 0.2 GeV/c
$^3He(e,e'p\pi^0)$	-0.2 - 0.02 GeV	-0.01 - 0.2 GeV/c

Table 4.1: Missing Energy and Momentum cuts applied to data set.

where the 4-vectors, γ, T, N and π are as follows: γ refers to the exchanged virtual photon, T refers to the target (assumed a free proton or neutron at rest), N refers to the outgoing nucleon, and π refers to either the π^0 or π^- depending upon the channel being considered.

Missing energy is then the energy term of the Missing 4-vector, and the missing momentum 3-vector corresponds to the momentum components of the same 4-vector.

For this definition of missing energy and momentum, both the missing energy and momentum are zero for events which correspond to a free nucleon being excited into a Δ by a virtual photon of known 4-vector, and the Δ decay products subsequently both being accurately measured.

This is unlikely to be exactly the case for any real events, since even quasi-free Δ excitation on a nucleon is affected by radiative losses and the target motion. However these effects are relatively small, and a very effective way of selecting quasi-free Δ excitation is to perform cuts on low missing energy and momentum. These cuts screen out most events which deviate significantly from the description given above.

Examples of the missing energy and momentum distributions are shown below in figure 4.1 for the $(e,e'p\pi^0)$ channel and $(e,e'p\pi^-)$ channel. Note the reduced resolution of the $(e,e'p\pi^0)$ channel when compared to the $(e,e'p\pi^-)$. This is the result of the relatively poor resolution for the π^0 invariant mass after reconstruction (as discussed in section 4.2). The accepted ranges of missing energy and missing momentum used in the cuts are shown in table 4.1.

4.1.2 The opening angle cut.

If the target nucleon were at rest with the properties of a free particle, then the 3-momentum vector of the reconstructed Δ will be identical to the 3-momentum of the incident virtual photon. If this is the case, then the angle between the incident virtual photon and the momentum vector of the reconstructed Δ should be zero. As it is Quasi-free Δ excitation of the Δ that is of interest here, this opening angle (the term 'opening angle' will be used throughout to refer to this cut.) can be used to discard events where the Δ decay products are either spurious or have been involved in a more complex process. There will also be legitimate events with a non-zero opening angle due to the Fermi motion of the target nucleon.

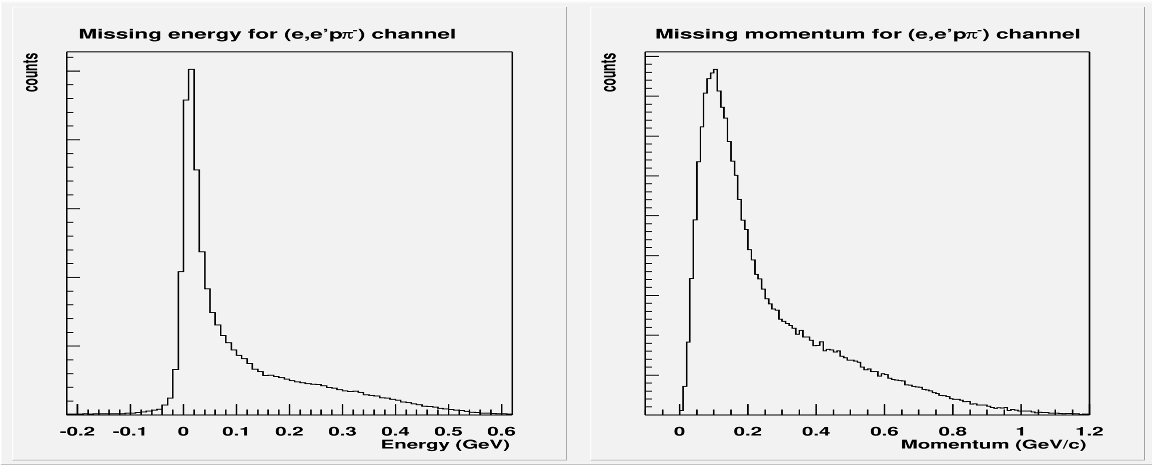

(a) Missing energy and missing momentum plots for the (e,e'pπ^-) channel.

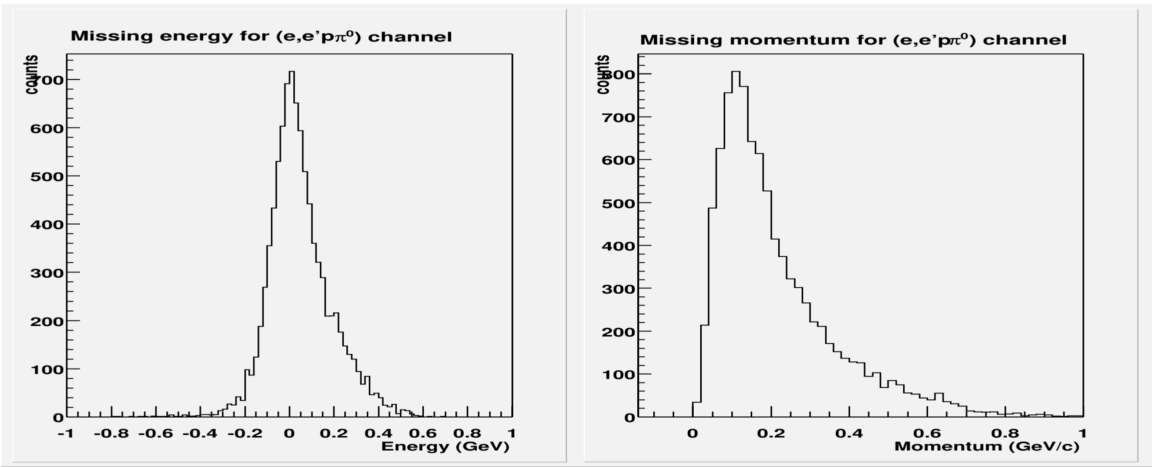

(b) Missing energy and missing momentum for the (e,e'pπ^0) channel.

Figure 4.1: Missing energy and missing momentum plots.

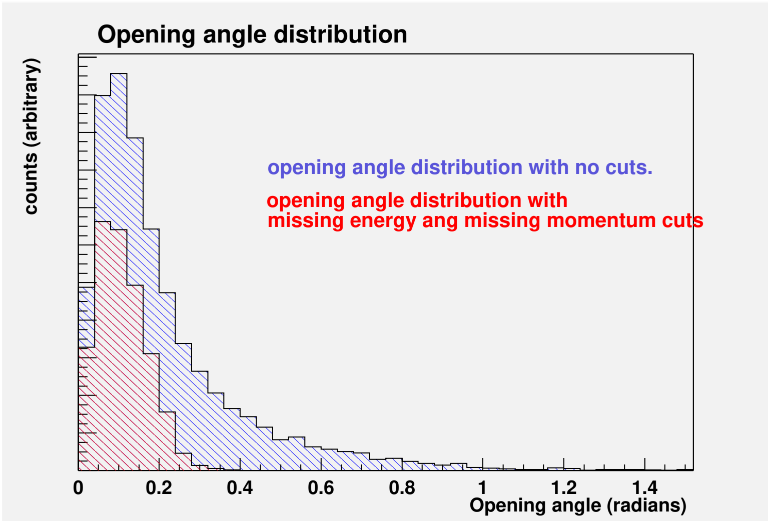

Figure 4.2: Experimental Opening Angle distribution.

Excluding events where this opening angle is large should then improve the quality of the physics signal with little loss of good events.

The opening angle distributions before and after the missing energy and missing momentum cuts were applied were used to decide upon the optimal value to set as the maximum acceptable opening angle between the reconstructed $\Delta(1232)$ and the exchanged virtual photon. As the missing energy, missing momentum and opening angle cut are all complementary, in selecting quasi-free $\Delta(1232)$ excitation, an acceptable opening angle cut corresponds to acceptable ranges in missing energy and missing momentum. The opening angle distributions before and after the missing energy and momentum cuts, are shown in fig 4.2. Based on this approach, a limit of 0.2 radians was set as the opening angle cut for both channels of interest.

In turn the effect of this opening angle cut on the missing energy and momentum distributions can be seen in fig 4.3.

The effect of the opening angle cut seems to improve the quality of the missing energy and missing momentum distributions significantly while only slightly reducing the height of the peaks.

A cut on the angle between the incident virtual photon and the reconstructed Δ was included in the analysis of the $\Delta(1232)$ invariant mass distributions and the analysis of the angular distributions of the decay products of the $\Delta(1232)$.

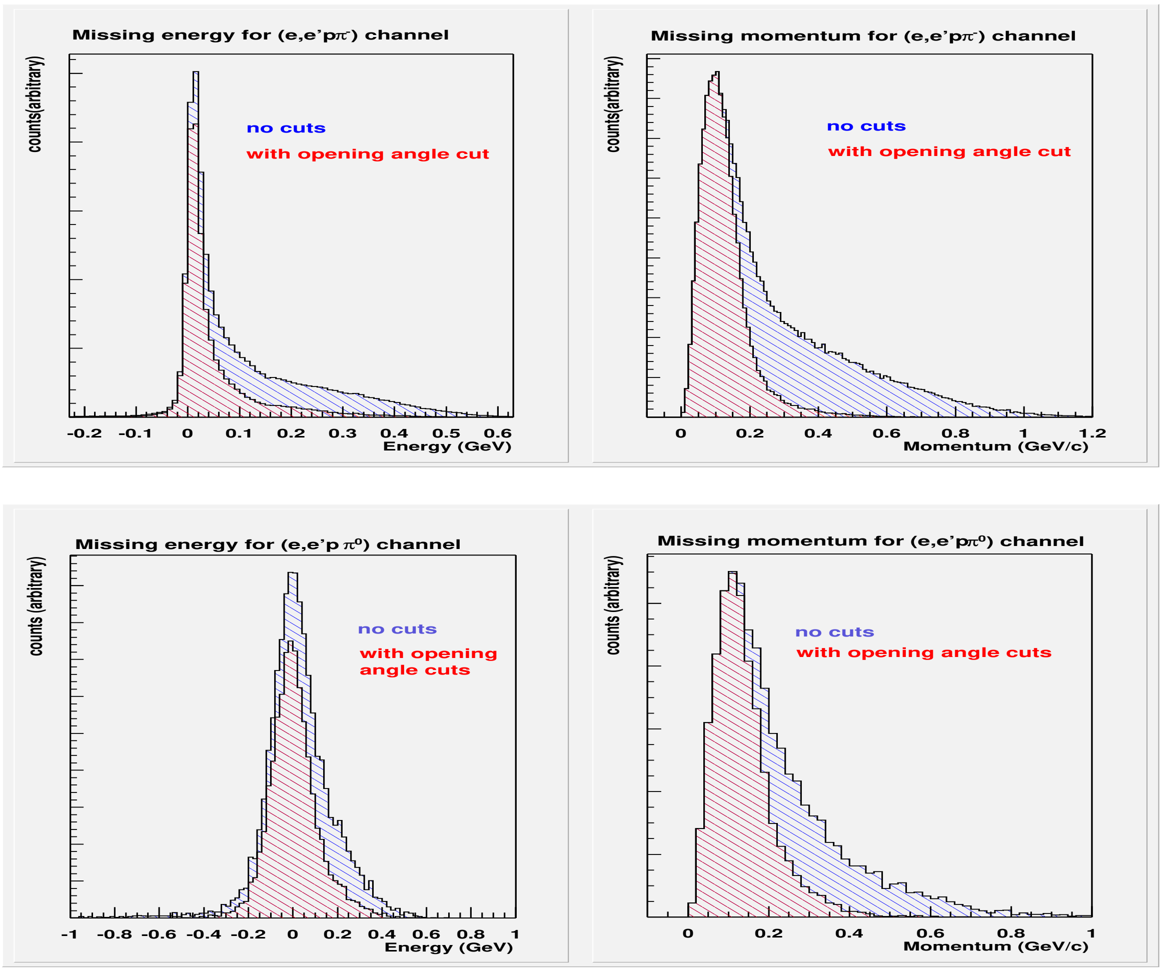

Figure 4.3: Effect of opening angle cut on missing energy and missing momentum distributions.

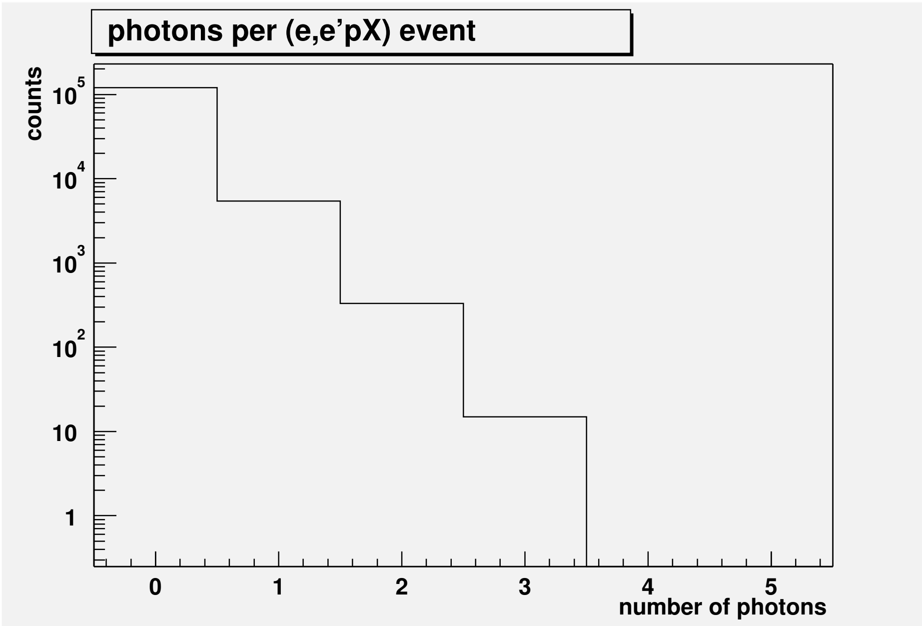

Figure 4.4: Number of photons per (e,e'pX) event (log scale).

4.2 π^0 reconstruction.

The π^0 decays electromagnetically into two $\gamma's$ with a mean lifetime of $8.4{\times}10^{-17}$s. Due to this short lifetime, the two $\gamma's$ must be detected and the π^0 reconstructed. This limits the CLAS π^0 detection to events where both $\gamma's$ are detected (the forward facing EC is the only detector element with reasonable π^0 detection efficiencies).

Reconstructing the π^0 is achieved by adding the 4-vectors of the two decay products. This necessitates a procedure for selecting $\gamma's$, which are decay products of the π^0 in question from the background of $\gamma's$ from other reactions.

Figure 4.4 shows a sample of events from the ^3He target used in the e2 run. Shown are the number of $\gamma's$ detected when a proton and electron were also detected. Since the number of 3γ events is so low, it was not considered worthwhile extracting possible π^0's from those events. Only the 2γ events were used.

By applying cuts on missing energy, missing momentum and opening angle the spurious photon pairs are largely eliminated, with little effect on the measured yield of the genuine π^0's. This can be seen in figure 4.5 which shows the invariant mass of the π^0 candidates before and after the the cuts are applied. π^0 candidates are only accepted within the invariant mass range of $0.1GeV/c^2$ and $0.2GeV/c^2$.

The π^0 events which remain after the cuts are then used for the Δ^+ reconstruction. The width of the π^0 invariant mass determines the quality of the physics signal for the $(e, e'p\pi^0)$ channel at every stage of the analysis, and leads to a reduction in resolution.

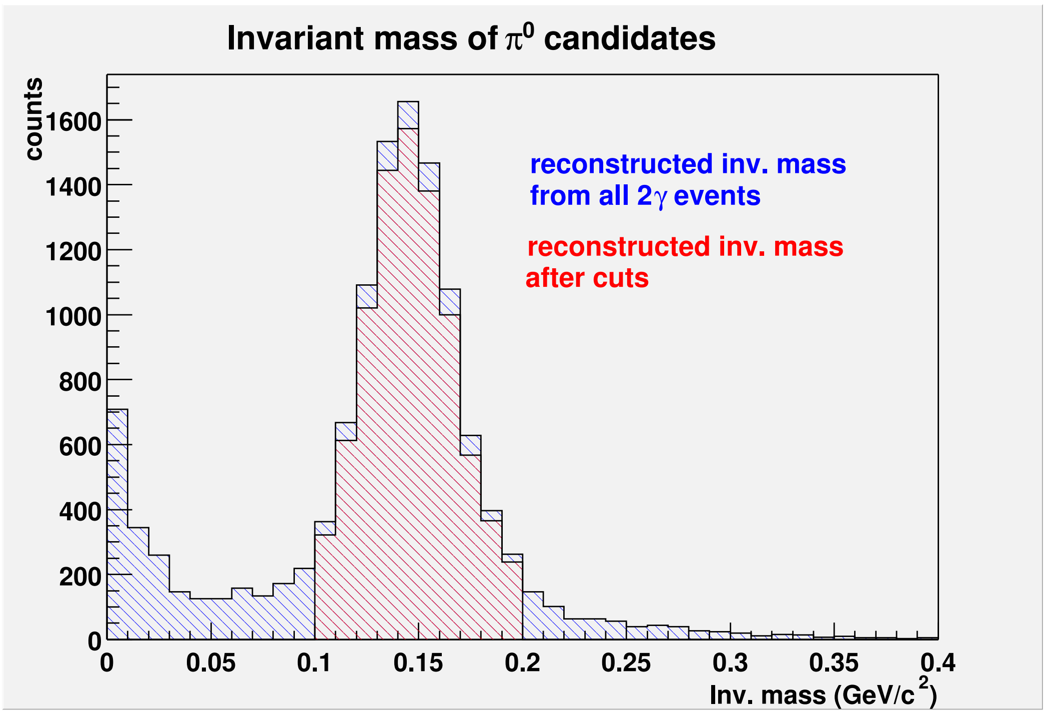

Figure 4.5: π^0 invariant mass selection.

Parameter	lower limit	upper limit
Opening Angle	0.0 radians	0.2 radians
Missing Energy	-0.2 GeV	0.2 GeV
Missing Momentum	-0.01GeV/c	0.2 GeV/c
π^0 Invariant Mass	0.1 GeV/c^2	0.2 GeV/c^2

Table 4.2: Cuts imposed for π^0 selection.

4.3 Acceptance Corrections

All the particle distributions measured in CLAS must be modified to take account of the acceptance of CLAS. Obvious geometrical examples of this are polar angles in the lab frame, which are limited by the lack of coverage at extreme forward and backward angles in CLAS due to the passage of the beam, and the azimuthal lab angles, which have six gaps caused by the magnet coils in CLAS. Also affecting acceptance are detector efficiencies and the effects of the event reconstruction software. These acceptance effects affect the measured angular distributions of the outgoing particles.

There exists a computational procedure for correcting for these effects (the geometrical coverage, detector efficiencies and software effects). i.e. a number of events are simulated by an event generator and the outgoing particles are tracked through a computer model of CLAS using a software package called GSIM which is based on the Geant simulation package. The output of GSIM then is subjected to the "cooking " process, and produces simulated events that display the effect of CLAS on the data set.

Due to time constraints the present analysis carried out a simpler approach where the geometrical coverage of CLAS alone was taken into account. Generated events were produced and selected based upon whether or not they would pass the fiducial cuts (see section 3.4.3). This assumes a flat acceptance within the region accepted by the fiducial cuts.This is a reasonable assumption which only neglects effects due to non-uniformities between individual elements in CLAS. These are monitored throughout experimental data taking and are known to be less than 10%.

The event generator used was called PSG, a phase space generator. Two separate data sets were created, one with an outgoing electron, proton and negatively charged pion (containing 9.7 million simulated events), the other with an electron, proton and neutral pion and its two photon decay products(containing 10 million simulated events). The W and Q^2 ranges of the generated events were $(1.0 < W < 1.6GeV)$ and $(0.1 < Q^2 < 0.6GeV)$ and the beam energy was set to the experimental value of 1.162GeV. Given these limits, and within the restrictions of energy and momentum conservation, events were generated at random.

The same analyses were carried out on the experimental data set and the generated data set. The effects of the fiducial cuts on the generated data were taken into account as follows.

For a given experimental distribution (f_{exp}) (which is made up of a series of bins), the content of each bin is f^i_{exp}, where i is the bin number. (In what follows the multiplication and addition of distributions means that the contents of each bin are multiplied or added.) For each distribution (f_{exp}) corresponding distributions (f_{PS}) and (f_{FC}) are generated using PSG. (f_{PS}) is the distribution before fiducial cuts are applied, and (f_{FC}) is the resulting distribution after fiducial cuts are applied. A distribution (f_C) is obtained such that $f_{PS} =$

$f_{FC} + f_C$.

(f_C) is the correction which restores (f_{FC}) to (f_{PS}). The correction (f_C) may then be applied to the experimental distribution (f_{exp}) if a factor is applied to each bin of (f_C) which takes into account the different bin contents of (f_{FC}) and (f_{exp}). This then means that the final corrected result (f_{CR}) has the form $f_{CR} = f_{exp} + f_C \times (\frac{f_{exp}}{f_{FC}})$.

Some examples of the result of this process are shown in figures 4.6 and 4.7. Figure 4.6 shows examples of (f_{PS}), (f_{FC}), $f(exp)$ and (f_{CR}) used for the correction to the invariant mass distribution from the $^3He(e, e'p\pi^-)$ channel (for the total Q^2 range available). Figure 4.7 shows (f_{PS}), (f_{FC}), $f(exp)$ and (f_{CR}) used for the correction of a ϕ^* distribution (using the $^3He(e, e'p\pi^-)$ channel for $0.6 < \theta^* < 0.8$ radians).

This general approach is adopted to correct for the geometrical acceptance in the analysis of the $\Delta(1232)$ invariant mass, and in the analysis of the ϕ^* and θ^* distributions(ϕ^* and θ^* are the azimuthal and polar angles of the decay products in the Δ zero momentum frame).

4.4 Theoretical comparison

In order to compare the behaviour of the $\Delta(1232)$ in the ^3He nucleus with the behaviour of the $\Delta(1232)$ excited from a free nucleon target the MAID program was used[1]. This comparison may provide information on where there are changes in behaviour of the $\Delta(1232)$ in the nuclear medium of ^3He in comparison to free nucleon Δ excitation.

Although the Δ resonance has been studied frequently, and some of its properties are predicted by a number of theoretical models, there remains, however, a number of aspects of Δ behaviour which have not received attention.

This thesis seeks to rectify some of these omissions, by specifically investigating if the $\Delta(1232)$ invariant mass is found to vary with Q^2, and if the $p \rightarrow \Delta^+$transition is significantly different from the $n \rightarrow \Delta^0$ transition. The latter point would be indicated by a difference in the ϕ^* distributions for the two reaction channels.

To provide theoretical input to the present studies, the MAID program was used to generate differential cross sections for the $n(e, e'p\pi^-)$ and the $p(e, e'p\pi^0)$ channels[54]. For each channel the total cross-section and the individual contributions from pure P_{33}^+ and pure non-resonant (Born) pion production were calculated. The resulting six differential cross sections were produced for the range $1100 < W < 1700 MeV/c^2$ in $2MeV/c^2$ steps, and the range $100 < Q^2 < 700(MeV/c)^2$ in $100(MeV/c)^2$ steps. The calculations were further

[1]The MAID code is the work of members of the Institut fur Kernphysik in Mainz, Germany. The code generates cross sections for photo and electroproduction reaction channels. The code is currently available to run on the University of Mainz web-site[53] and is based on work by Drechsel et al.[2, 41]

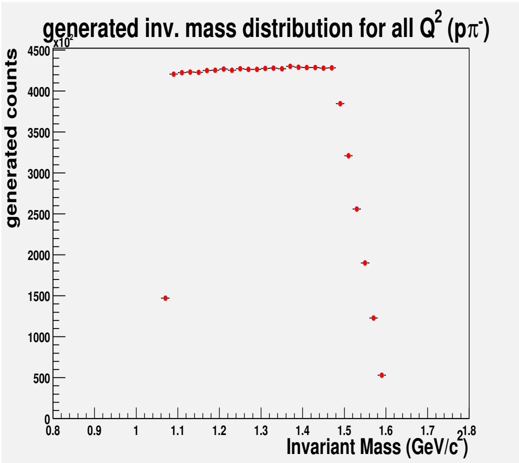

(a) generated events (PSG)

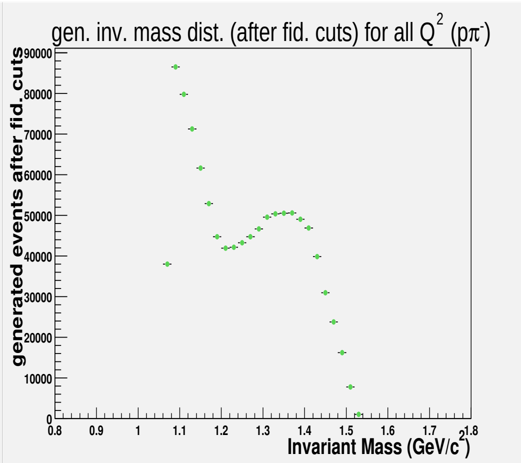

(b) generated events after fiducial cuts

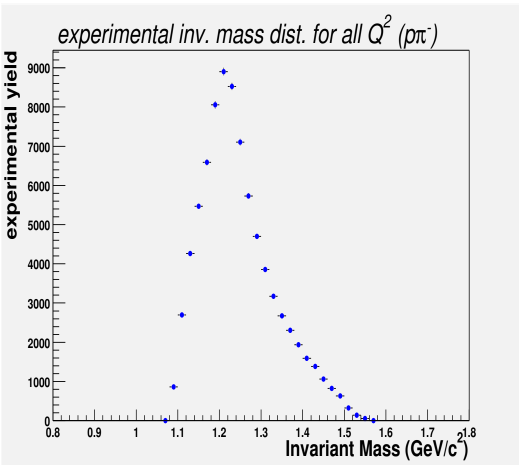

(c) experimental distribution (with fid. cuts)

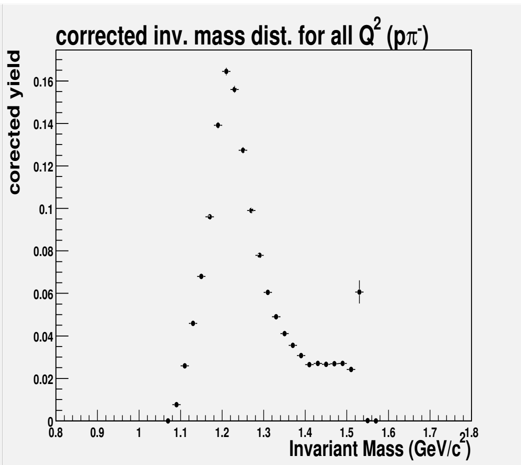

(d) corrected distribution

Figure 4.6: Correction carried out on an invariant mass distribution

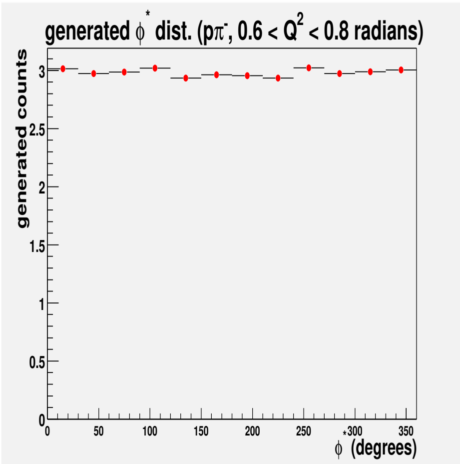

(a) generated events (PSG)

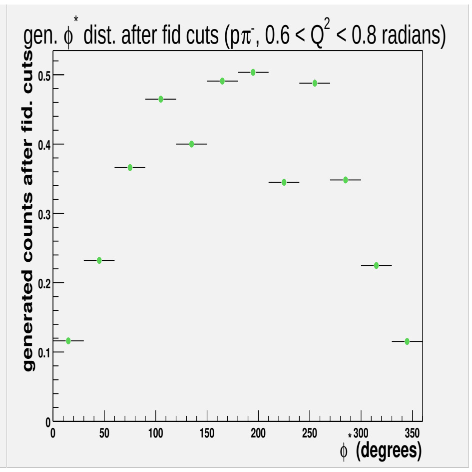

(b) generated events after fiducial cuts

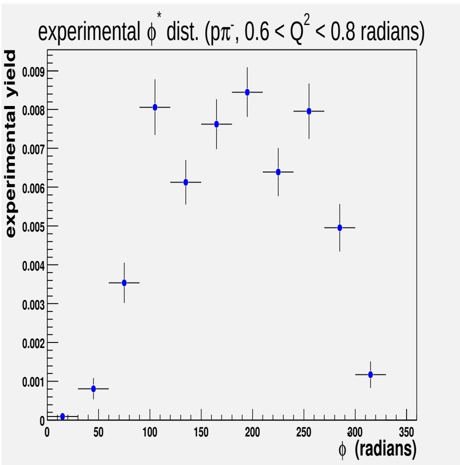

(c) experimental distribution (with fiducial cuts)

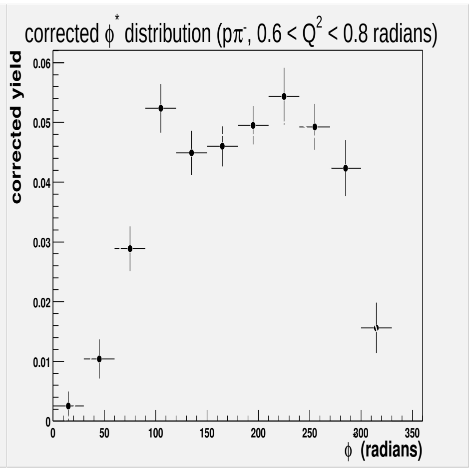

(d) corrected distribution

Figure 4.7: Correction carried out on ϕ^* distribution

subdivided to provide differential cross-sections for the $\Delta(1232)$ decay products for full θ^* and ϕ^* coverage. This means that over a range of phase space defined by the W and Q^2 ranges selected, we have access to theoretical values for the cross section at any point for the invariant mass of the $\Delta(1232)$, and for any values of the ϕ^* and θ^* angles of the $\Delta(1232)$ decay products.

4.5 $\Delta(1232)$ distributions with Q^2

As has been covered earlier, the work presented in this thesis falls into three sets of results. The first of these is a study of the variation of the $\Delta(1232)$ invariant mass with Q^2 in response to the the results published by Richard Sealock (as discussed in section 1.).

The procedure for reconstructing the invariant mass of the $\Delta(1232)$ is similar to the procedure used to reconstruct the π^0 invariant mass. The proton and the pion (or the 2γ final state of the π^0) must be detected. After this the $\Delta(1232)$ four vector is calculated from the vector sum of the decay products. The opening angle cut and the missing energy and missing momentum cuts of section 4.1.1 were then applied and the acceptance correction of section 4.3 used.

The distributions were split into three Q^2 ranges and were compared to see if there was any variation on centroid position and width with Q^2. The distributions were fitted using a standard Lorentz function. The invariant mass fit was limited to the range of $1.15 GeV/c^2$ to $1.30 GeV/c^2$. The reason for this is that the invariant mass distributions for the $(e, e'p\pi^-)$ channel contain a contribution from Born terms, where non resonant π^- production is added to the resonant π^-production.

The upper limit of $1.3 GeV/c^2$ was chosen, since above this value, the Born terms are clearly disturbing the shape of the invariant mass distribution. The lower limit of $1.15 GeV/c^2$ is set to avoid the deformation to the Lorentzian shape of the distribution by the invariant mass threshhold for producing a nucleon and pion.

Although the effect of Born terms is much less for the $^3He(e, e'p\pi^0)$, the fitting range used for the $(e, e'p\pi^0)$ channel is the same as that of the $(e, e'p\pi^-)$ channel for the sake of consistency, since the values of centroid position and width are to some degree dependent upon the fitting ranges. The experimental invariant mass distributions for the $(e, e'p\pi^0)$ channel have widths which are broadened by the resolution of the π^0 invariant mass which contributes to the reconstructed invariant mass of the Δ^+.

The Q^2 ranges for each channel are shown in figure 4.8.

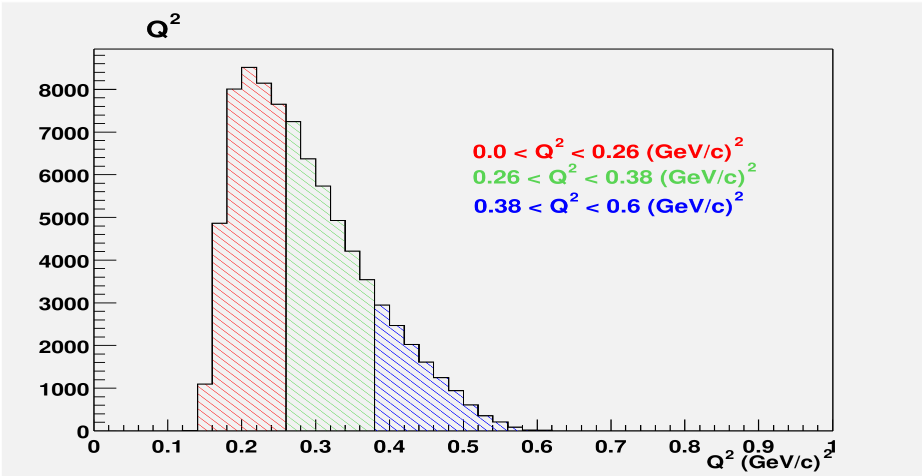

(a) Q^2 ranges for the (e,e'pπ^-) channel.

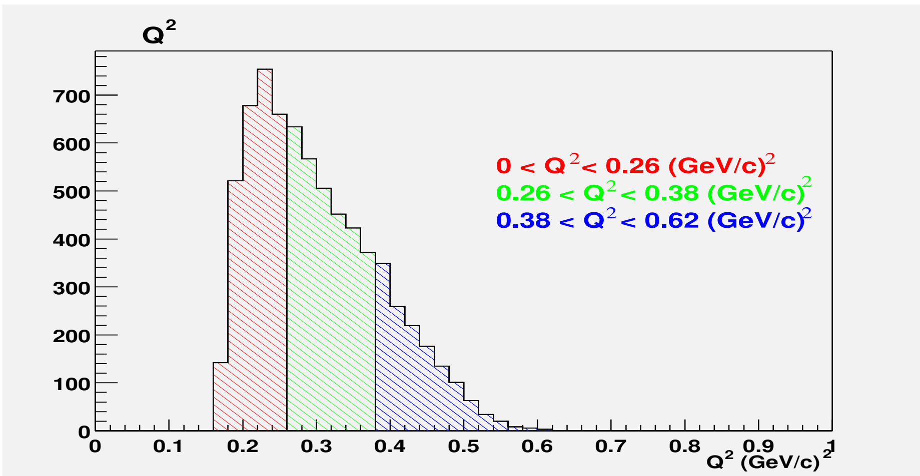

(b) Q^2 ranges for the (e,e'pπ^0) channel.

Figure 4.8: Q^2 ranges used for Δ invariant mass distributions

4.6 On a possible momentum dependent potential

As discussed in section 2.4.2, for events where a particle in the nucleus is given some additional momentum by the transferred virtual photon during electron scattering, it is possible to determine the difference between the potential experienced by the particle before and after it is struck. This has been carried out for a proton in ^3He using the $(e, e'p)$ quasi-elastic peak. A similar investigation has been undertaken for an excited Δ^0. In this case it is the difference between the potential experienced by the neutron in ^3He and the excited Δ^0.

Events are selected where only the outgoing particle of interest is involved in the reaction. The data selection procedure has been based on missing energy cuts, where missing energy is defined according to the channel of interest. This has been successful in isolating the channel of interest, as is shown in figure 4.9.

For the $^3He(e, e'p)pn$ channel the missing 4-vector ($p_{Missing}$) for the reaction is shown in eqn 4.2. The events in the red-hatched region of figure 4.9 have missing energies less than 0.05GeV and greater than -0.05GeV. The events in the blue-hatched region of figure 4.9 also have missing energies less than 0.05GeV and greater then -0.05GeV. (For the $^3He(e, e'p\pi^-)$ channel the missing 4-vector is defined as above in eqn 4.1).

$$p_{Missing} = \gamma + T - p \tag{4.2}$$

Calculation of p_f and δV

The calculations of p_f, $\delta V_{(e,e'p)}$ and $\delta V_{(e,e'p\pi^-)}$ as defined in section 2.4.2 are described are carried out as follows.

The magnitude of the vector $\underline{p_f}$ is calculated assuming that the magnitude of the initial momentum($\underline{p_i}$) is known. The value chosen for p_i is derived from the expression $\langle p_i^2 \rangle = \frac{k_F^2}{2}$, where k_f is the Fermi momentum(values for k_f were set at $272MeV/c$ for the proton and $216MeV/c$ for the neutron). It is also assumed that the direction of the struck particle, with momentum $\underline{p_f}$ is parallel to the direction of the detected particle($\underline{p_o}$). Since $\underline{p_f}$ is the vector sum of $\underline{q}$ (the 3-momentum transferred during the electron scattering interaction) and $\underline{p_i}$ then $\underline{p_f}$ is calculated based upon the diagram shown in figure 4.10.

The quantity δV for each channel is calculated from equation **??**, the arguments for which are now all known.

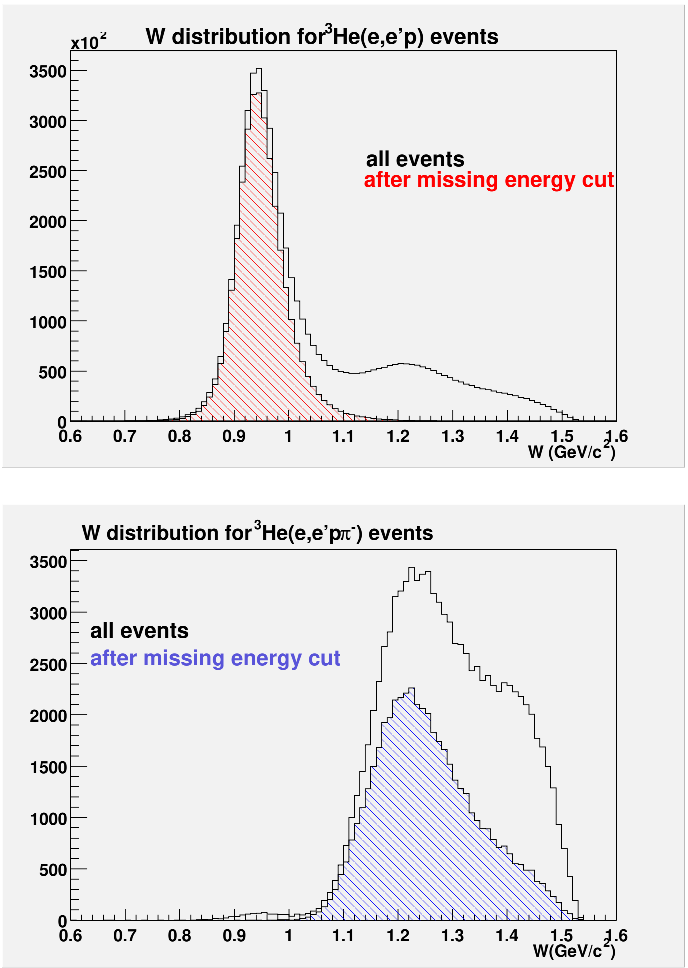

Figure 4.9: Missing energy cut effects on W used for δV vs. p_f analysis.

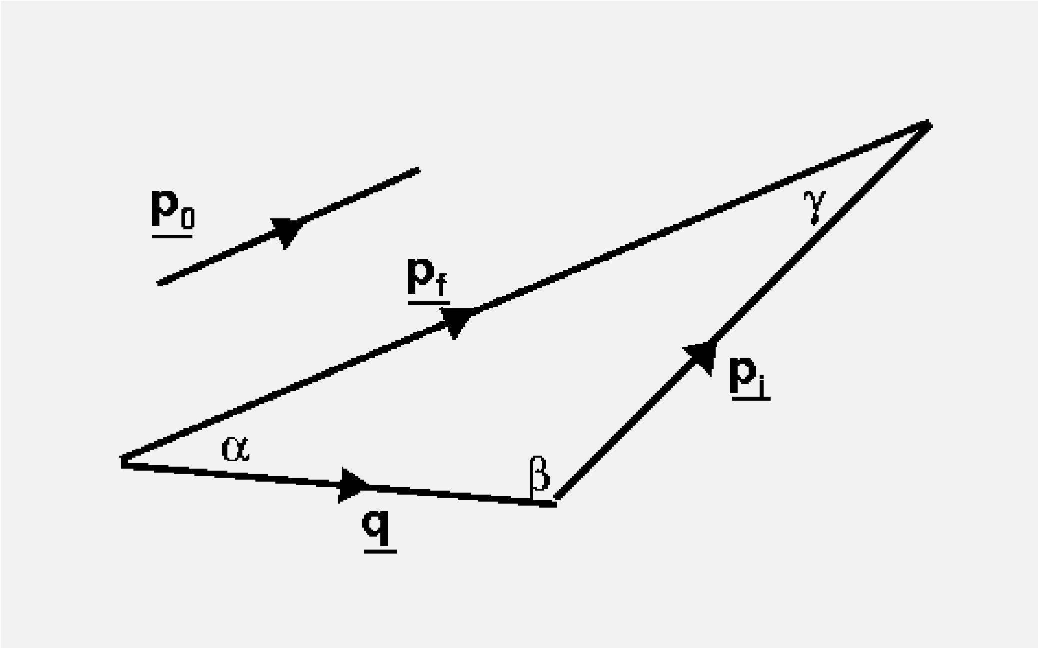

Figure 4.10: Method of calculating the magnitude of p_f.

4.7 Azimuthal Distributions

As discussed earlier(section 2.3.2) the ϕ^* distribution for a given θ^* of the $\Delta(1232)$ decay products in the Δ rest frame is of interest as it allows the $N - \Delta$ transition multipole amplitudes to be deduced. These angles ϕ^* and θ^* can be calculated if the Δ decay particles are detected in CLAS.

4.7.1 Definition of terms.

The relevant quantities are shown in figure 4.11. θ^* and ϕ^* are the polar and azimuthal angles of the pion, which, in the Δ rest frame, is anti-parallel to the proton2.3.2.

$\theta^*$and $\phi^*$are defined relative to the virtual photon, such that the polar angle θ^* is deduced from the dot product of the momenta of the virtual photon and the outgoing pion. The azimuthal ϕ^* angle is measured relative to a vector perpendicular to the electron scattering plane(in the Δ rest frame). This perpendicular vector is calculated as the cross-product of the scattered electron and the virtual photon (in the Δ rest frame). Therefore both θ^* and $\phi^*$are defined with respect to the Δ rest frame. The virtual photon 3-vector is parallel to the z-axis, the vector perpendicular to the scattering plane is parallel to the x-axis and the y-axis lies in the electron scattering plane.

The data are analysed to provide plots of ϕ^* distributions for various θ^* ranges. From these plots the quantities proportional to $\sigma_T + \epsilon_L\sigma_L$, σ_{TT} and σ_{LT} are extracted.

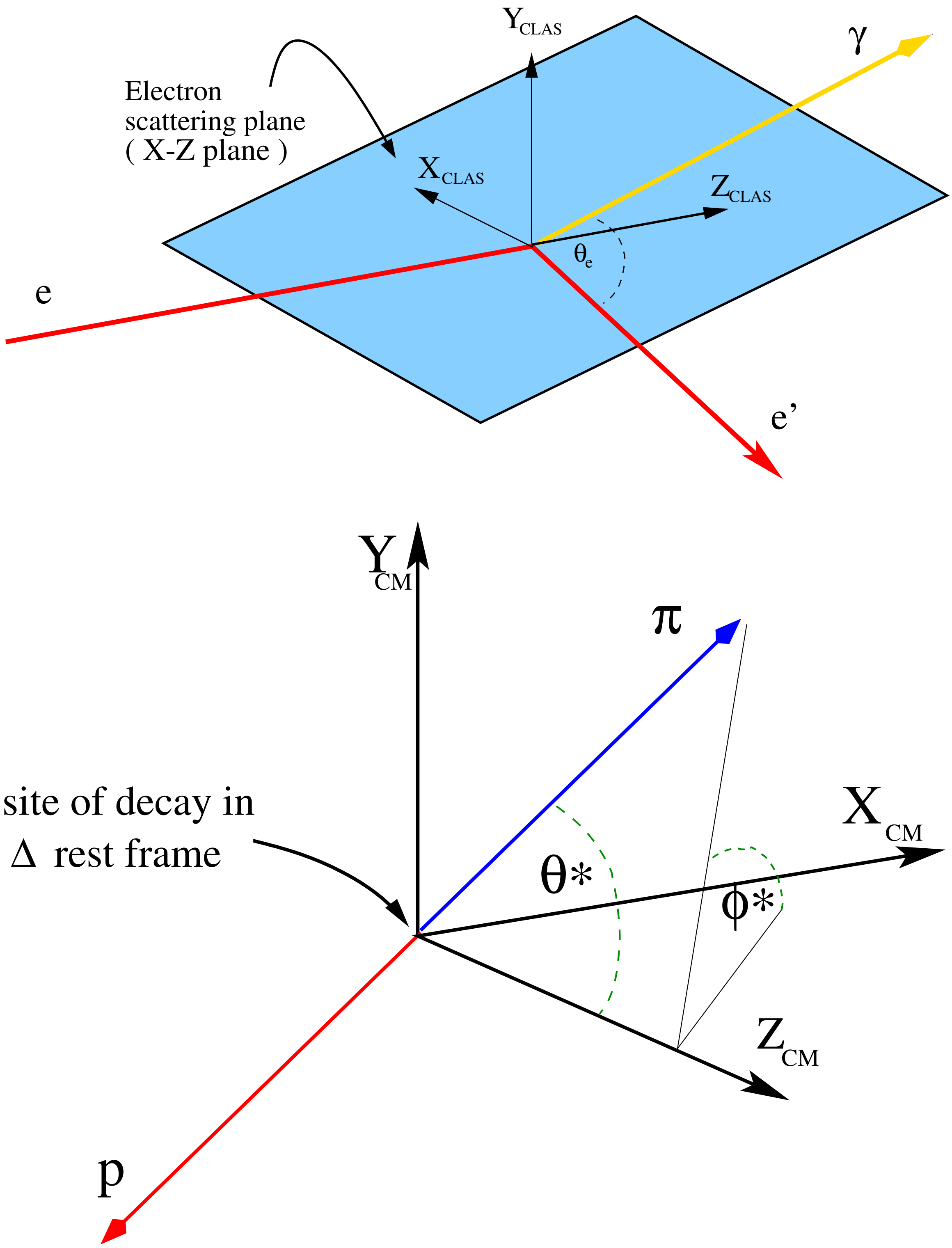

Figure 4.11: Definitions of ϕ^* and θ^* angles. (see section 2.3.2)

As discussed earlier (see section 2.3.2) the electro-production cross section is of the form shown in eqn. 2.9 multiplied by the Γ (the "virtual photon flux" [19]). The values of θ^*_π and ϕ^*_π are calculated as described above for each event. Then the values of p^*_π, $k^*_\gamma$and Γ are also calculated also on an event by event basis and for each division in θ^*_π the ϕ^*_π distributions are filled. Each entry in the ϕ^*_π distributions is weighted by multiplying by a factor $(\frac{p^*_\pi}{k^*_\gamma})\Gamma sin(\theta^*_\pi)$. This means that the magnitude of the distributions should be proportional to the cross section when the acceptance of CLAS (described in section 4.3)is taken into account.

4.7.2 Fitting procedure

After the ϕ^*_π distributions have undergone the acceptance corrections they may now be fitted. The form of the electroproduction cross section is as shown in equation 2.9. This equation is then fitted using a fitting function(F) as shown in equation 4.3.

$$F = A + Bcos(2\phi^*_\pi) + Ccos(\phi^*_\pi) \tag{4.3}$$

where $A = \sigma_T + \epsilon_L \sigma_L$, $B = \epsilon \sigma_{TT} sin^2(\theta^*_\pi)$ and $C = \sqrt{2\epsilon_L(\epsilon + 1)}\sigma_{LT} sin(\theta^*_\pi)$.

The data were split into θ^*_π bins of 0.2 radians(approx. 11.5^o) and each ϕ^*_π distribution was split into 12 bins of 30^o(approx. 0.5 radians).

For each θ^*_π segment values of A,B and C were calculated. Then the values of $\sigma_T + \epsilon_L \sigma_L$, σ_{LT} and σ_{TT} were calculated (using the mean value of ϵ and $\epsilon_L$for the appropriate value of θ^*_π) for each θ^*_π segment.

Chapter 5

Results and Conclusions

What follows are the results of the analyses described in the previous chapter. The results of the invariant mass distributions are shown as the yield (number of events filling the relevant bin) corrected for the geometrical acceptance of CLAS and then scaled according to the area under the range of the fit (which is from 1.15 to 1.3 GeV/c^2). The results of the study of the momentum dependence of the potential experienced by nuclear constituents are shown as contour plots. These plots are of the number of events per bin, with no acceptance corrections applied. The angular distributions of the $\Delta(1232)$ decay products are shown as yield corrected for the CLAS acceptance. What are presented here are therefore not cross sections but (assuming the acceptance corrections are complete) differ from cross sections by a constant factor in each case.

Hence these analyses a.) Compare the qualitative behaviour of the shift in centroid value and width of the invariant mass distributions with four momentum transfer for the $^3He(e, e'p\pi^-)$ and $^3He(e, e'p\pi^0)$ channels. b.) Present evidence that a proton and a Δ^0 experience momentum dependent potentials in ^3He and c.) Present angular distributions of the decay products for both channels.

5.1 Invariant mass distributions

The invariant mass distributions for the $^3He(e, e'p\pi^-)$ and $^3He(e, e'p\pi^0)$ channels are shown in figures 5.1 to 5.4 and figures 5.8 to 5.12 respectively. The fits described in section 4.7.2 are shown for each data set (the three Q^2 ranges and the total data set) and the fit parameters for each are shown in tables 5.1 and 5.2. As stated above these are not cross sections. Additionally, the variation in amplitude between data sets is due to a combination of the behaviour of the physics signal, the CLAS acceptance and choice of Q^2 ranges as well as the scaling process (although the scaling will not effect the shape of the invariant mass distributions).

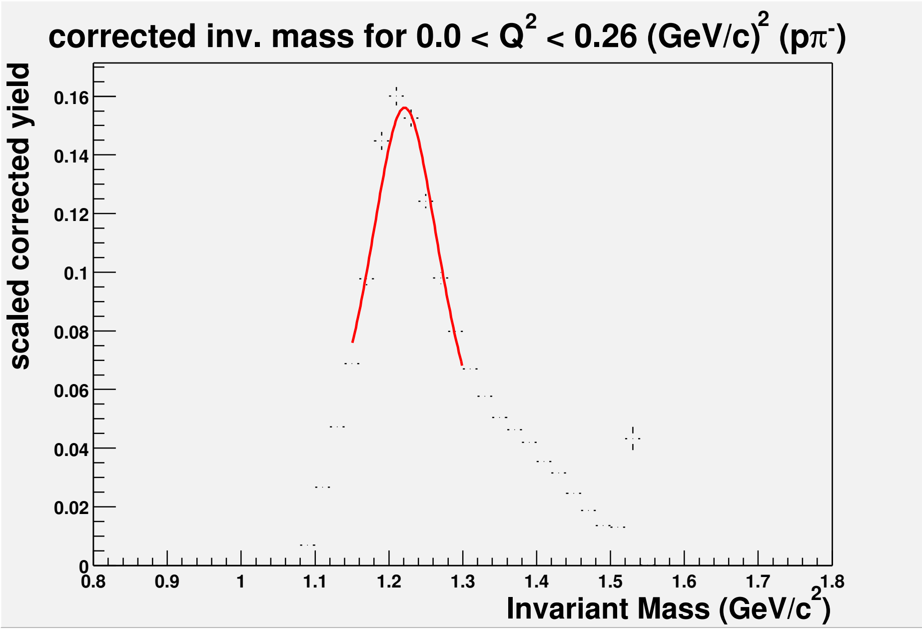

Figure 5.1: $p\pi^-(\Delta^0)$invariant mass distribution. $(0.0 < Q^2 < 0.26(GeV/c)^2)$ Corrected yield scaled for the area under the fitting range for the $^3He(e, e'p\pi^-)$ channel using events in the lowest Q^2 range.

5.1.1 $^3He(e, e'p\pi^-)$ events.

The invariant mass distribution for detected proton and pi-minus pairs lying within the first Q^2 range (0.0 < Q^2 < 0.26 $(GeV/c)^2$) is shown in figure 5.1, for the second Q^2 range (0.26 < Q^2 < 0.38 $(GeV/c)^2$) in figure 5.2 and the third Q^2 range (0.38 < Q^2 < 0.6 $(GeV/c)^2$) in figure 5.3. The invariant mass distributions for the whole Q^2 range are shown in figure 5.4. All four distributions are shown along with the distribution of the total Q^2 range in figure 5.5.

As can be clearly seen by looking at figure 5.5, the shape of the invariant mass distributions varies with increasing Q^2. The number of events decreases at higher values of invariant mass and both the centroid position and the width of these distributions decrease with increasing Q^2.

These effects may be due to CLAS acceptance effects which a complete GSIM simulation would take into account. However, there may be physical explanations for these effects. The first is that the non-resonant pion production background is dropping off significantly more quickly than the P_{33} term, leading to a signal which can be considered pure P_{33} resonance as we reach higher values of Q^2. The second is that there may be some other process for example another baryon resonance, which is most relevant at lower Q^2 values. Finally the behaviour of Born terms must be considered. The MAID code was used to estimate the relative importance of these effects, and a discussion of its use is included below.

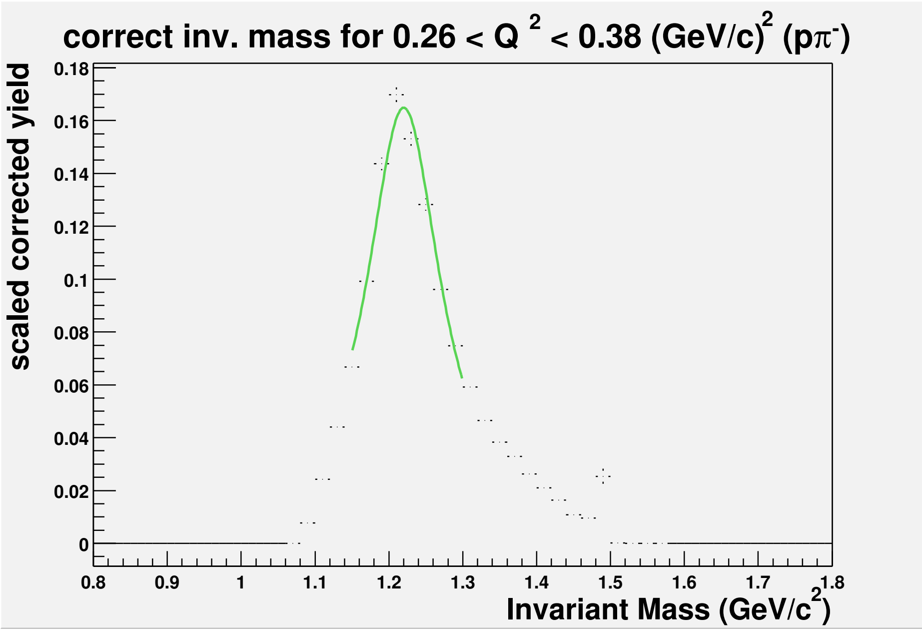

Figure 5.2: $p\pi^-(\Delta^0)$invariant mass distribution $(0.26 < Q^2 < 0.38(GeV/c)^2)$ Corrected yield scaled for the area under the fitting range for the $^3He(e, e'p\pi^-)$channel using events in the middle Q^2range.

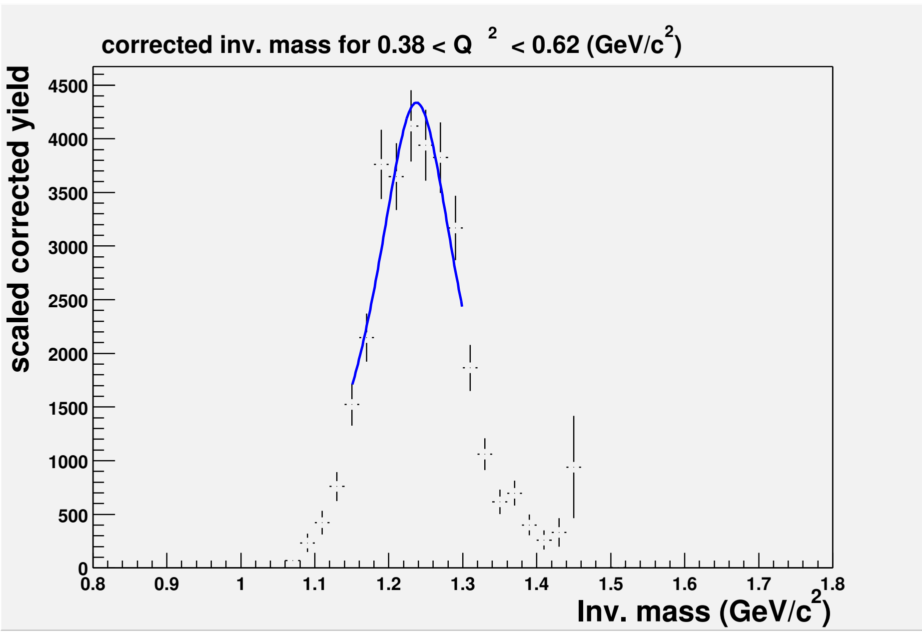

Figure 5.3: $p\pi^-(\Delta^0)$invariant mass distribution $(0.38 < Q^2 < 0.60(GeV/c)^2)$ Corrected yield scaled for the area under the fitting range for the $^3He(e, e'p\pi^-)$ channel using events in the middle Q^2 range.

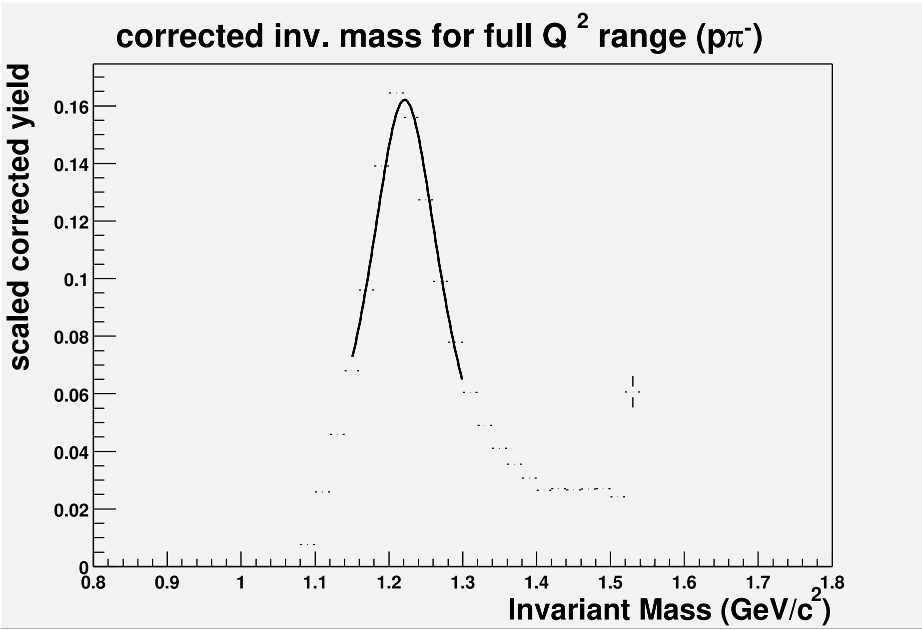

Figure 5.4: $p\pi^-(\Delta^0)$ invariant mass distribution $(0.0 < Q^2 < 0.60(GeV/c)^2$ Corrected yield scaled for the area under the fitting range for the $^3He(e, e'p\pi^-)$ channel using all events (total Q^2range).

Comparison with MAID code

As stated above, if the behaviour of the background observed in figure 5.5 is to be accounted for as the contribution from Born terms, then this means that the contribution from Born terms must decrease more quickly than the contribution from the P_{33} resonance as Q^2 increases. The MAID calculations for the behaviour of the invariant mass for pure Born term contributions and pure P_{33} contributions are shown in figure 5.6. Although the behaviour of the invariant mass distributions at the $\Delta(1232)$ peak (i.e. for invariant mass < $1.3GeV/c^2$) show a significant decrease in amplitude with Q^2 for both the Born terms and P_{33} contributions, the P_{33} strength is much more peaked around the Δ resonance particularly for the lowest Q^2 range. At higher invariant mass the Born terms and P_{33} contributions have similar shapes as is shown in figure 5.7.

It is worth noting two points. The first is that the Q^2 ranges for the MAID calculations do not relate exactly to the Q^2 ranges used for the data. It is also essential to remember that because these are calculations of pure P_{33} and Born term amplitudes, the calculation is incomplete since the amplitudes which include the P_{33} and Born terms will not simply be the addition of the two, but must also contain the interference terms between the two processes.

Clearly, a more complete theoretical treatment is required and a more accurate determination of the CLAS acceptance should be carried out before the nature of the background in the invariant mass distributions can be fully explained. However, the present analysis does

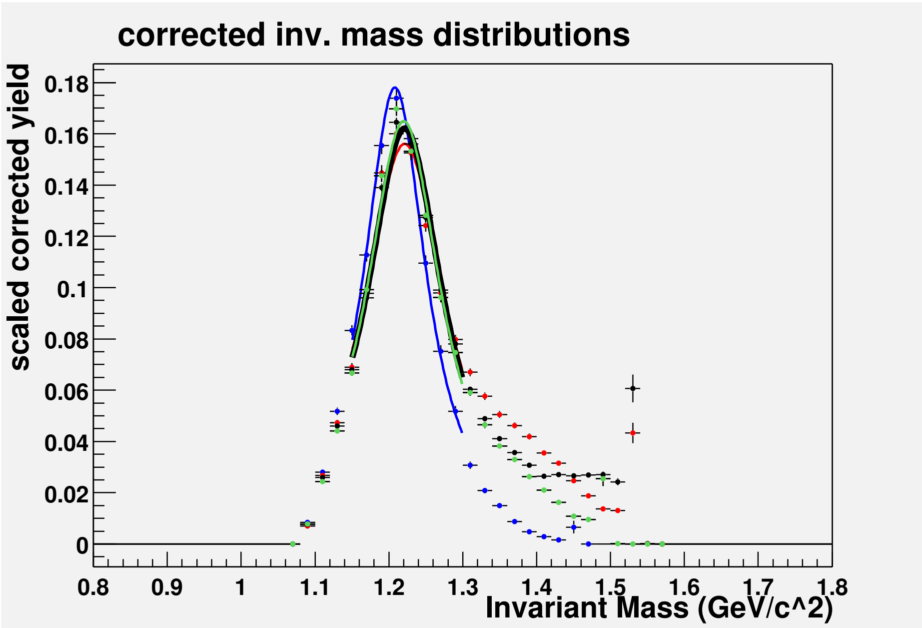

(a) Comparison of inv. mass distributions for varying Q^2 ranges

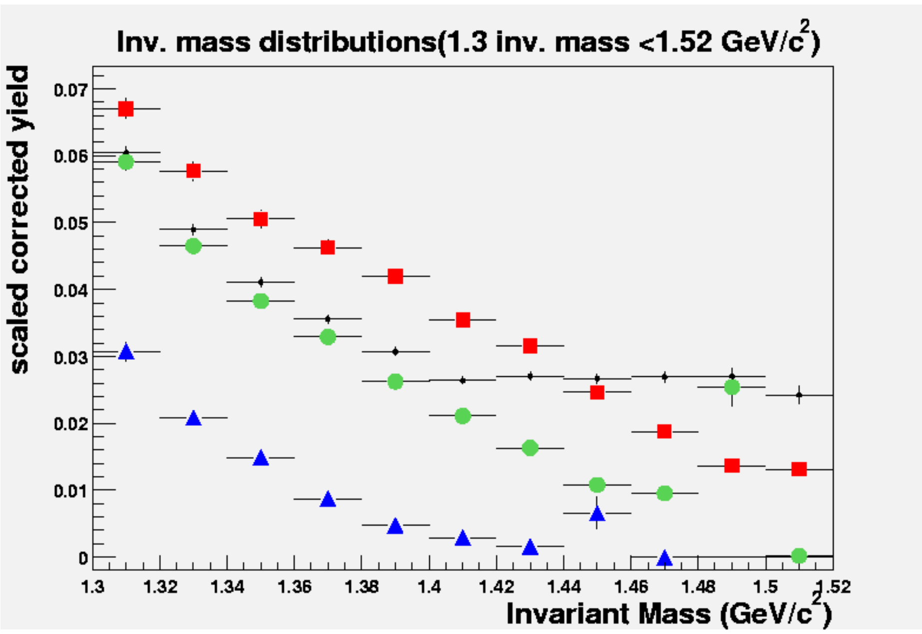

(b) as above but for inv. mass range 1.3 - 1.52 GeV/c^2

Figure 5.5: Comparison of $p\pi^-(\Delta^0)$ invariant mass distributions.
Comparison of four data sets: $0.0 < Q^2 < 0.26(GeV/c)^2$(red), $0.26 < Q^2 < 0.38(GeV/c)^2$(green), $0.38 < Q^2 < 0.6(GeV/c)^2$(blue), $0.0 < Q^2 < 0.6(GeV/c)^2$ (black).

provide values for the Δ width and centroid position which have been measured in a more direct manner than for any previous measurements.

As the Born terms are suppressed for the $^3He(e,e'p\pi^0)$ channel in comparison of the $^3He(e,e'p\pi^-)$ channel, the shapes of the $^3He(e,e'p\pi^0)$ invariant mass distributions will be more sensitive to the resonance than the Born term amplitudes.

5.1.2 $^3He(e,e'p\pi^0)$ events

Here we present in figures 5.8 to 5.12 plots for the $^3He(e,e'p\pi^0)$ channel. The Q^2 ranges for $^3He(e,e'p\pi^0)$ are the same as for $^3He(e,e'p\pi^-)$ (except for the third Q^2 bin which covers the range 0.38 - 0.62 $(GeV/c)^2$ as opposed to the range 0.38 - 0.60 $(GeV/c)^2$). This channel should have no contributions from Born terms. Hence any background observed at higher invariant mass for the $^3He(e,e'p\pi^-)$ channel will not be due to Born terms.

The invariant mass distributions for the Q^2 range 0.0 - 0.26 $(GeV/c)^2$ is shown in figure 5.8, for the Q^2 range 0.26 - 0.38 $(GeV/c)^2$ in figure 5.9, and for the Q^2 range 0.38 - 0.62 $(GeV/c)^2$ in figure 5.10. With the invariant mass distribution for the total Q^2 range is shown in figure 5.11.

It is clear that for all Q^2 ranges, the resonance strength is more dominant for$^3He(e,e'p\pi^0)$ than $^3He(e,e'p\pi^-)$. This is a clear indication that Born terms are important in the $^3He(e,e'p\pi^-)$ channel.

5.1.3 Summary

The peak centroid positions and widths for all of the plots produced from this analysis are shown in tables 5.1 and 5.2. Table 5.1 shows the fit parameters for the $^3He(e,e'p\pi^-)$channel while table 5.2 shows the fit parameters for the $^3He(e,e'p\pi^0)$ channel. As stated earlier the fitting range was chosen to be between $1.15GeV/c^2$ and $1.3GeV/c^2$ for both channels. This range was chosen to avoid the low invariant mass part of the distributions where the characteristic resonant shape is lost due to the $p\pi$ invariant mass threshhold and also to avoid the higher invariant mass part of the distribution where the background processes make a more significant contribution. Although this fitting range is justifiable the resulting fit parameters (centroid position and width) are sensitive to the fitting range. As such, slight variations on the fitting range were used (up to $30MeV/c^2$ above and below the preferred upper and lower limits of the fitting range) to observe the sensitivity of the fit parameters to the chosen range. It was found that the centroid position varied very little with the fitting range (by less than 1%) but because of the variation of the shape of the fitted line as the fitting range varied the width of the distributions was much more sensitive. The width of the

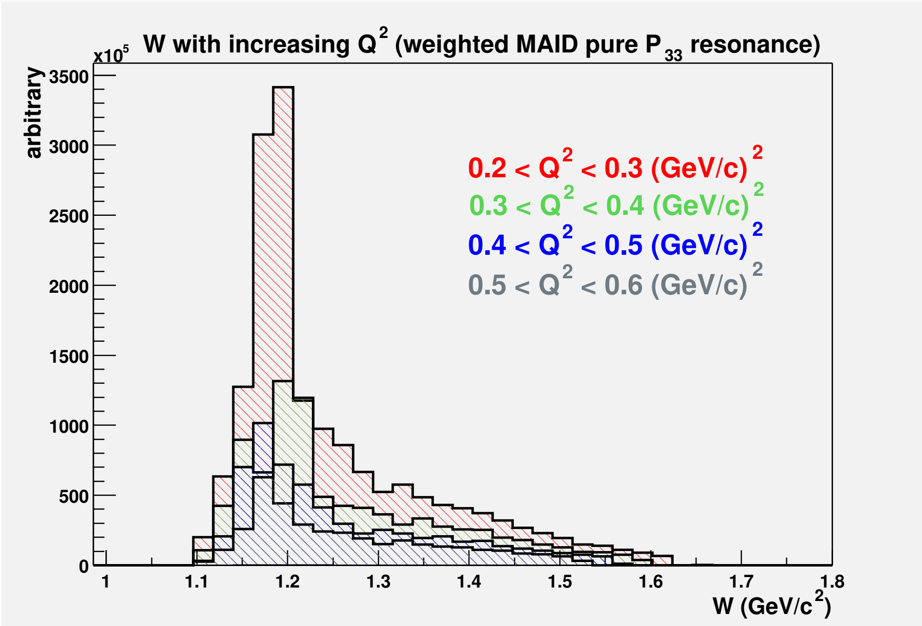

(a) pure P_{33} contributions

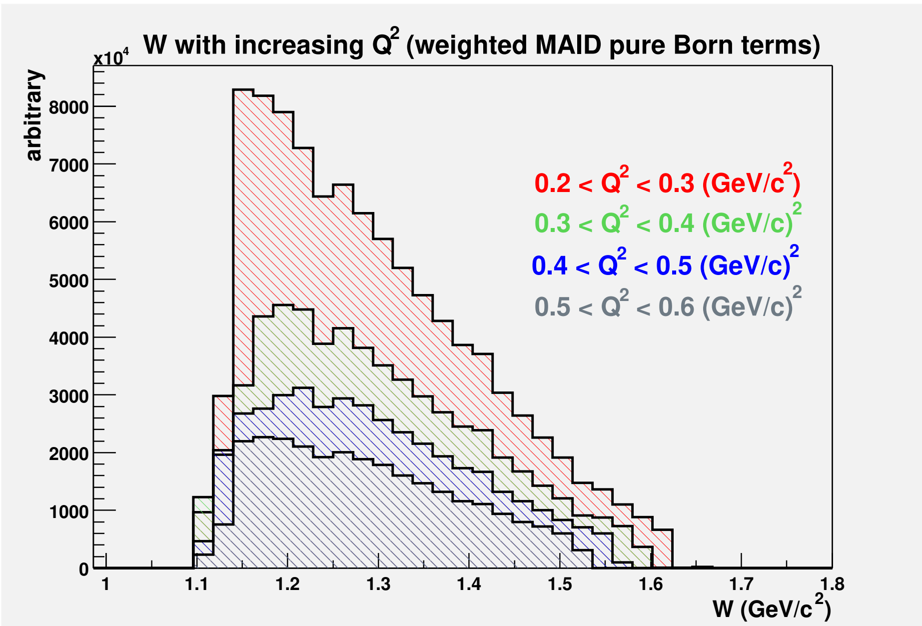

(b) pure Born term contributions

Figure 5.6: MAID invariant mass spectra (full range) for $p\pi^-(\Delta^0)$channel. Shown are the MAID calculations for the $p\pi^-$ final state for the pure P_{33} and Born term contributions for the full range of invariant mass.

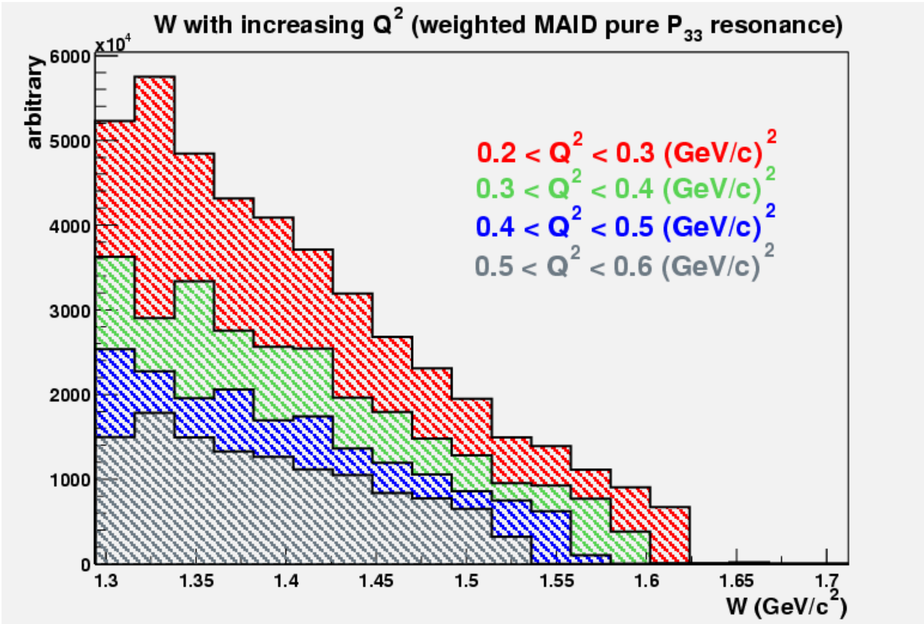

(a) pure P_{33} contribution

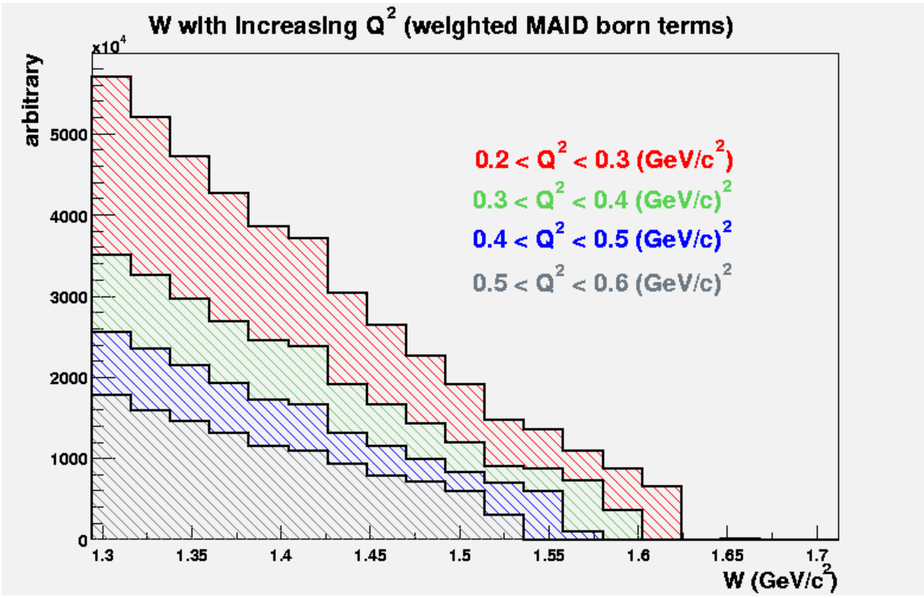

(b) Pure Born term contribution

Figure 5.7: MAID invariant mass spectra (1.3 - 1.7GeV/c^2) for the $p\pi^-(\Delta^0)$channel. Shown are the MAID calculations for the $p\pi^-$ final state for the pure P_{33} and Born term contributions.

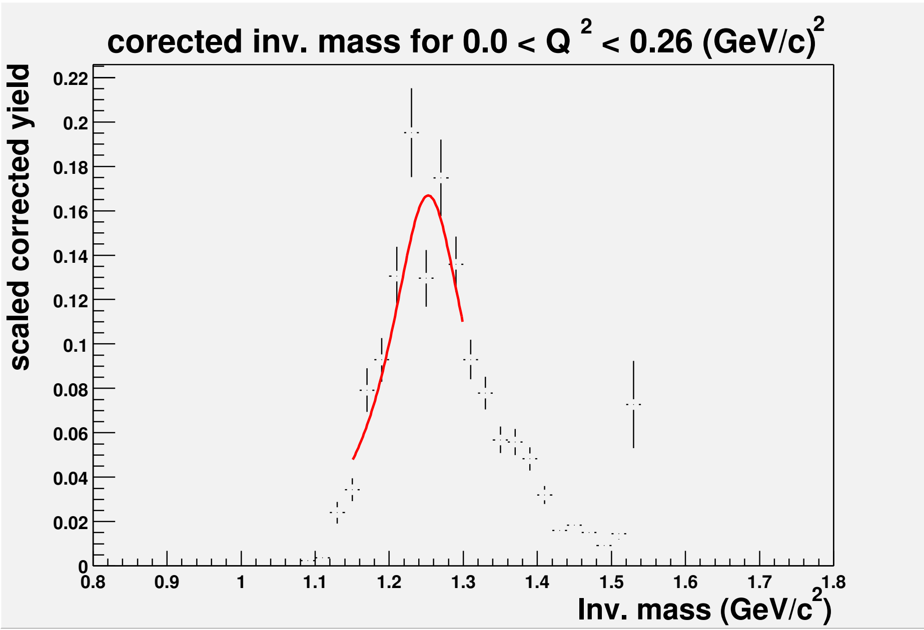

Figure 5.8: $p\pi^0(\Delta^+)$ invariant mass distribution $(0.0 < Q^2 < 0.26(GeV/c)^2)$ Corrected yield scaled for the area under the fitting range for the $^3He(e, e'p\pi^0)$ channel using events in the lowest Q^2range.

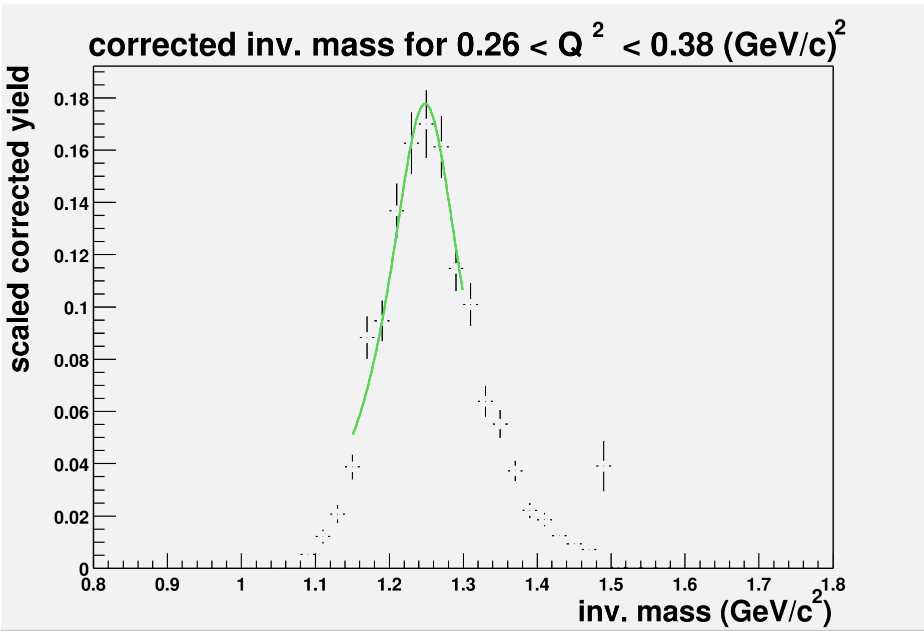

Figure 5.9: $p\pi^0(\Delta^+)$ invariant mass distribution $(0.26 < Q^2 < 0.38(GeV/c)^2)$ Corrected yield scaled for the area under the fitting range for the $^3He(e, e'p\pi^0)$ channel using events in the middle Q^2 range.

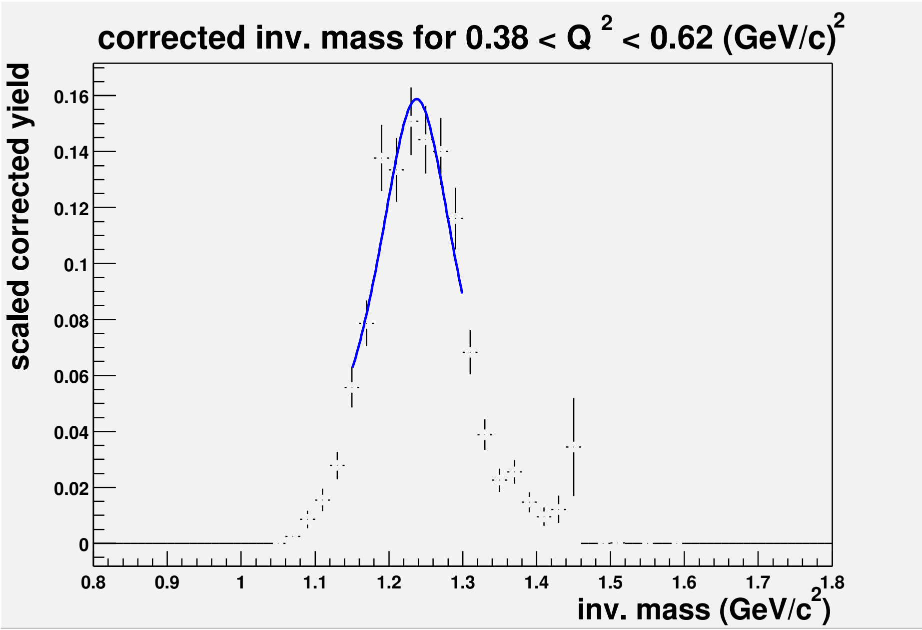

Figure 5.10: $p\pi^0(\Delta^+)$ invariant mass distribution $(0.38 < Q^2 < 0.62(GeV/c)^2)$ Corrected yield scaled for the area under the fitting range for the $^3He(e,e'p\pi^0)$ channel using events in the highest Q^2 range.

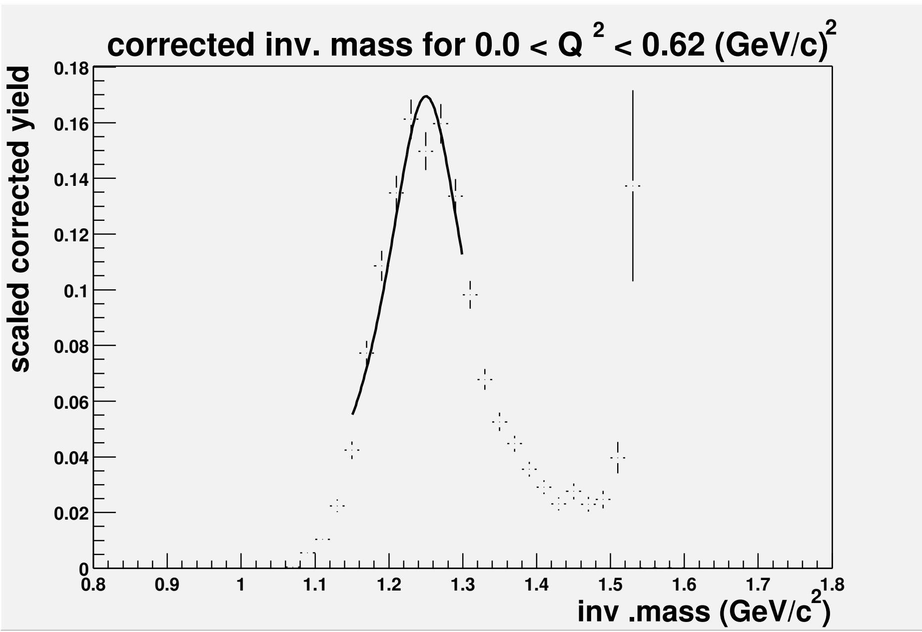

Figure 5.11: $p\pi^0(\Delta^+)$ invariant mass distribution $(0,0 < Q^2 < 0.62(GeV/c)^2)$ Corrected yield scaled for the area under the fitting range for the $^3He(e,e'p\pi^0)$ channel using events in the whole Q^2 range.

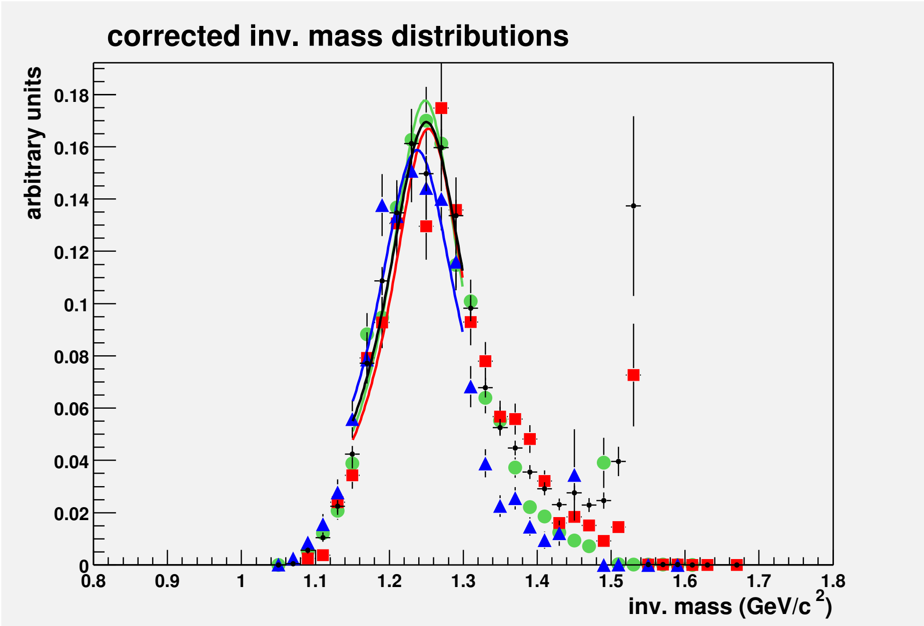

(a) Comparison of inv. mass distributions for varying Q^2 ranges.

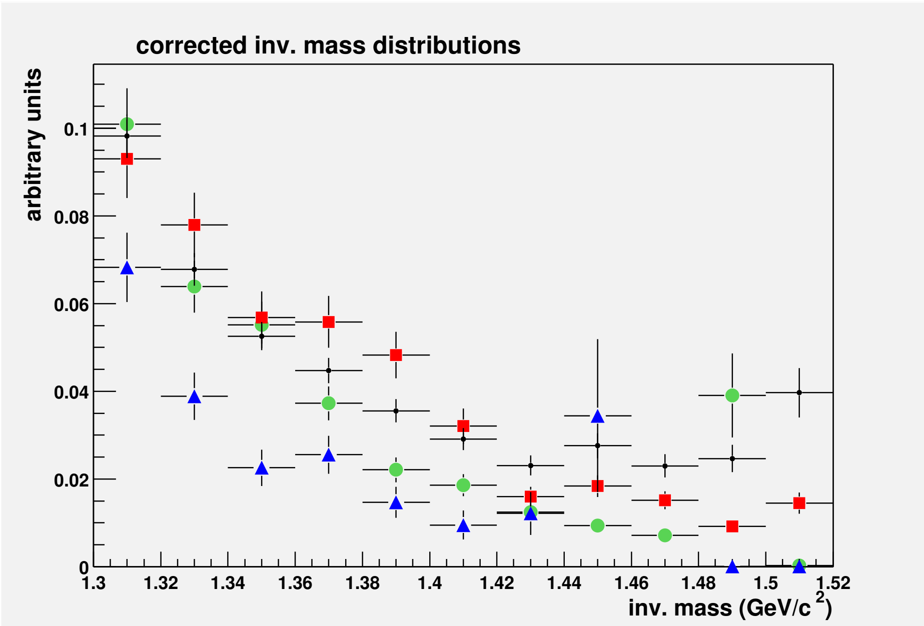

(b) as above but for inv. mass range 1.3 - 1.52 GeV/c ^{2}

Figure 5.12: Comparison of $p\pi^0(\Delta^+)$ invariant mass distributions. Comparison of four data sets: $0.0 < Q^2 < 0.26(GeV/c)^2$(red), $0,26 < Q^2 < 0.38(GeV/c)^2$(green), $0,38 < Q^2 < 0.62(GeV/c)^2$(blue), $0.0 < Q^2 < 0.62(GeV/c)^2$(black).

distributions varied by up to 30% depending upon the fitting range chosen. It is clear that a fuller description of both the relevant background processes and the effects of CLAS on these distribution must be completed before the widths of these distributions can be stated with any certainty.

As can be seen there is a reduction in the centroid position of the invariant mass distributions for both channels as Q^2 increases (the errors from the fit are typically less than $5MeV/c^2$ for the $^3He(e,e'p\pi^0)$channel and less than $1MeV/c^2$for the $^3He(e,e'p\pi^-)$channel, while an additional uncertainty in the centroid position due to the choice of fitting range of approximately $10MeV/c^2$exists, meaning that the variation with Q^2 is only just still valid after the errors are taken into account). As has been discussed earlier the invariant mass distributions have a non-resonant strength at higher invariant mass which diminishes with Q^2. This has the effect of shifting the centroid position to higher values of invariant mass which becomes less of an effect at higher values of Q^2. This could explain the decrease of the centroid position as Q^2 increases. Also there seems to be no evidence to support Sealock et al's observation that the invariant mass of the $\Delta(1232)$ increases with Q^2[1]. Once again there must be full acceptance corrections before this can be stated definitively although an effect as pronounced as that observed by Sealock is unlikely to arise from acceptance effects.

Based upon the fits to the data the width of the $\Delta(1232)$ invariant mass distribution appears to vary with Q^2 (although the sensitivity of the width to the fitting range means that this result is very speculative). For the $(e,e'p\pi^-)$ channel the presence of Born terms makes interpretation difficult. For a clear interpretation of these results further work is required in calculating the effect of the Born terms on the overall distribution. This would not be appropriate until the questions surrounding the acceptance effects have been resolved.

The Born terms are not present in the results from the $(e,e'p\pi^0)$ channel. There remains the problem of the width of the reconstructed π^0 invariant mass. This contributes significantly to the $\Delta(1232)$ invariant mass distribution and its behaviour with Q^2 is unknown. This problem is compounded by a limited understanding of acceptance effects which are likely to be different for this channel than for the previous one.

The results of the present analysis are shown alongside the data presented by Sealock et al[17] in figure 5.13. As can be seen the results of the present analysis show the apparent decrease in centroid position with Q^2, although this variation is accounted for within the error bars. Nevertheless the data set as a whole is in disagreement with Sealock et al in that the pronounced increase in centroid position with Q^2 is not present. Although a complete background subtraction and corrections for the effect of CLAS are still required it is unlikely that such a pronounced difference is due to background processes or CLAS.

Table 5.1: Invariant mass distribution fit parameters ($^3He(e,e'p\pi^-)$ channel)

Q^2 range $(GeV/c)^2$	centroid position (MeV/c^2)	statistical error in centroid position (MeV/c^2)	estimate of systematic error in centroid position (MeV/c^2)	width (MeV/c^2)	statistical error in width (MeV/c^2)	estimate of systematic error in width (MeV/c^2)
0.0- 0.26	1220	0.3	10	128	2.2	35
0.26- 0.38	1219	0.6	10	119	1.5	35
0.38- 0.60	1208	0.5	10	107	1.8	35
0.0- 0.60	1220	0.6	10	123	2.2	35

Table 5.2: Invariant mass distribution fit parameters ($^3He(e,e'p\pi^0)$ channel)

Q^2 range $(GeV/c)^2$	centroid position (MeV/c^2)	statistical error in centroid position (MeV/c^2)	estimated of systematic error in centroid position (MeV/c^2)	width (MeV/c^2)	error in width (MeV/c^2)	estimated of systematic error in width (MeV/c^2)
0.0- 0.26	1253	2.0	10	130	6	35
0.26- 0.38	1246	5.0	10	117	12	35
0.38- 0.62	1241	3.0	10	151	8	35
0.0- 0.62	1250	4.0	10	137	14	35

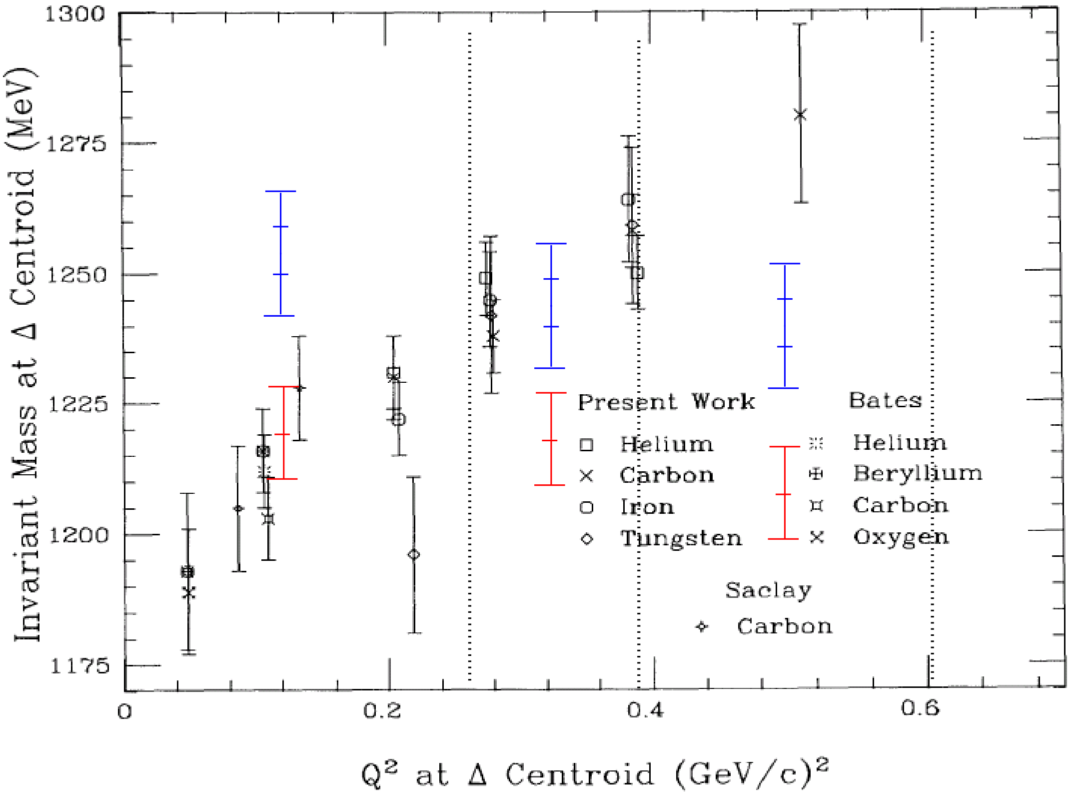

Figure 5.13: Comparison of current results with Sealock et al.

Above is shown figure 1.2 with the results of tables 5.1 and 5.2 superimposed. It should be stressed that the measurements described in this thesis are of the invariant mass of the detected proton and pion system while the results presented by Sealock et al[17] are inclusive measurements of W.

The vertical dotted lines show the limits of the three Q^2 bins used.

The data points are shown (the $(e, e'p\pi^-)$channel in red and the $(e, e'p\pi^0)$channel in blue) with statistical uncertainties in the centroid position stated as $1MeV/c^2$ for the $^3He(e, e'p\pi^-)$channel and $5MeV.c^2$ for the $^2He(e, ep\pi^0)$ channel (these are represented by the thinner inner error bars). The errors due to the sensitivity of the fitting range are small (less than 1%) but this only relates to the quality of the fit (These systematic errors are represented by the wider outer error bars). The distributions fitted may me skewed by underlying processes or the effects of CLAS. The Horizontal error bars show the width of the relevant Q^2 range.

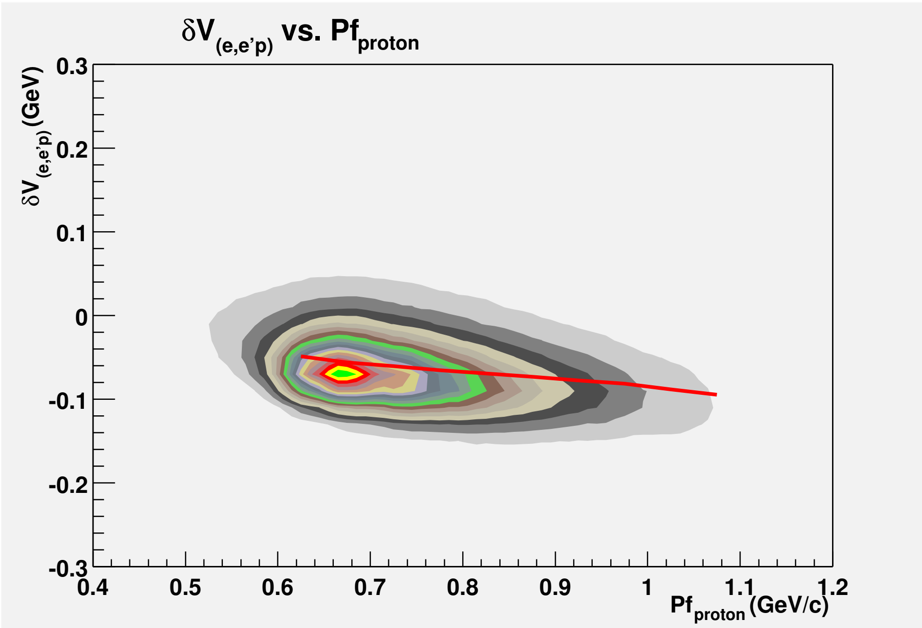

Figure 5.14: $\delta V_{(e,e'p)}$with p_f

5.2 Momentum Dependent Potential

The measured change in potential as described in section 4.6 is shown for the $^3He(e,e'p)$ channel in figure 5.14. Due to the expected spread in the data arising from Fermi motion for the $\delta V_{(e,e'p)}$ distribution the mean value was calculated and is shown on the plot. The mean values are the mean values of δV calculated for different values of p_f, the mean-lines shown the behaviour of the means as $p_f$varies. As can be seen the mean values for all the plots shown here are consistently located above the peak position of the distributions. The general trend of $\delta V_{(e,e'p)}$ shows that as the proton momentum inside the nucleus increases, the proton becomes more tightly bound.

Shown in figure 5.15 is the W vs. Q^2 distribution for all the events that remain after the selection procedure described in section 4.6. It must be noted that W and Q^2 are calculated using the 4-momentum of the scattered electron. It is apparent, there is no change in W as Q^2 is varied. This is not inconsistent with the results for $\delta V_{(e,e'p)}$ since W depends on the virtual photon and proton in its initial state. $\delta V_{(e,e'p)}$ depends on the final state of the proton and hence is influenced by any change in the proton potential arising from a change in its momentum.

The variation of potential with momentum for the $^3He(e,e'p\pi^-)$ channel is shown in figures 5.16 and 5.17. Figure 5.16 shows the values for δV_Δ when an invariant mass of $1.232GeV/c^2$ is assumed. This follows the analysis of O'Connell and Sealock (see reference [20]) where the Δ invariant mass is assumed to be $1.3GeV/c^2$. Figure 5.17 shows the result of the calculation where the experimental value of the Δ invariant mass is used on an event by event basis. The two plots vary significantly. The first displays a decreasing trend (from the region of poor statistics) until a minimum is reached and then an increasing trend. The second shows similar behaviour in the region of poor statistics at low values of p_f but continues to decrease, resembling the behaviour of the $^3He(e, e'p)$ data set.

The evaluation of δV_Δ using the experimental value of the Δ invariant mass is to be considered the more reliable.

Figure 5.18 shows the W vs. Q^2 distributions for the $^3He(e, e'p\pi^-)$ data set. There appears to be no significant variation of W with Q^2. This is consistent with the results presented earlier in this thesis, where it was found that that there was no significant change in the Δ invariant mass with Q^2. Neither the results shown in figure 5.15 nor the present measurements of the Δ invariant mass show any variation of invariant mass (W) with Q^2, as expected from Sealock et al[1].

However, the present studies of the variation of the proton nuclear potential with momentum are consistent with the present data on Δ invariant masses which show that the invariant mass seems to decrease slightly with increasing Q^2. Since the proton becomes more tightly bound inside the nucleus as its momentum increases, the momentum it has once it escapes is correspondingly less. This is reflected in a smaller value of the Δ invariant mass evaluated from the energy and momenta of the Δ decay products. This is best illustrated by a specific example considering $\Delta \rightarrow p+\pi$, i.e. If $Q^2 = 0.20(GeV/c)^2, \omega = 0.38GeV$ and the kinetic energy of the proton is $T_p = 0.13GeV$, then the kinetic energy of the pion $T_\pi = 0.11GeV$, and the Δinvariant mass is $M_\Delta = 1.182GeV/c^2$. However, if, for the same $Q^2$and T_π,the kinetic energy of the proton is $T_p = 0.10GeV$ due to the proton being more tightly bound in the nucleus, then to satisfy energy conservation, $\omega = 0.35GeV$,and $M_\Delta = 1.158GeV/c^2$.

The example shows that if the binding energy of a proton resulting from the decay of a Δ inside the nucleus becomes larger, then the invariant mass of the Δ calculated from the decay products becomes smaller. (In most cases, the Δ will decay inside the nucleus since with a lifetime of ~10^{-24} seconds it travels ~0.3fm before decaying.)

The mean-lines for the three plots are shown in figure 5.19. As can be seen the mean values of the change in potential for $^3He(e, e'p)$ and $^3He(e, e'p\pi^-)$ (relying upon the experimental values for invariant mass) are slightly different. The $^3He(e, e'p\pi^-)$ result is shifted up by approximately 15 MeV, but there is no significant difference in the behaviour of the trends.

5.3 Azimuthal distributions

What follows are the ϕ^* distributions for the two decay channels. First is shown $^3He(e, e'p\pi^-)$ with the fits in red (figures 5.21 through to 5.28), followed by the fit parameters (figures

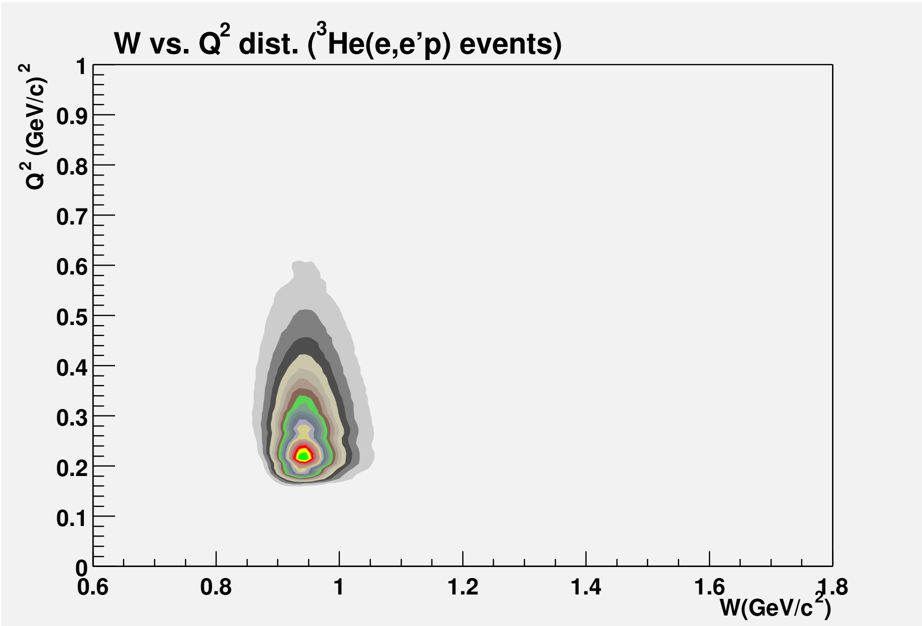

Figure 5.15: W vs. Q^2, for (e,e'p) events

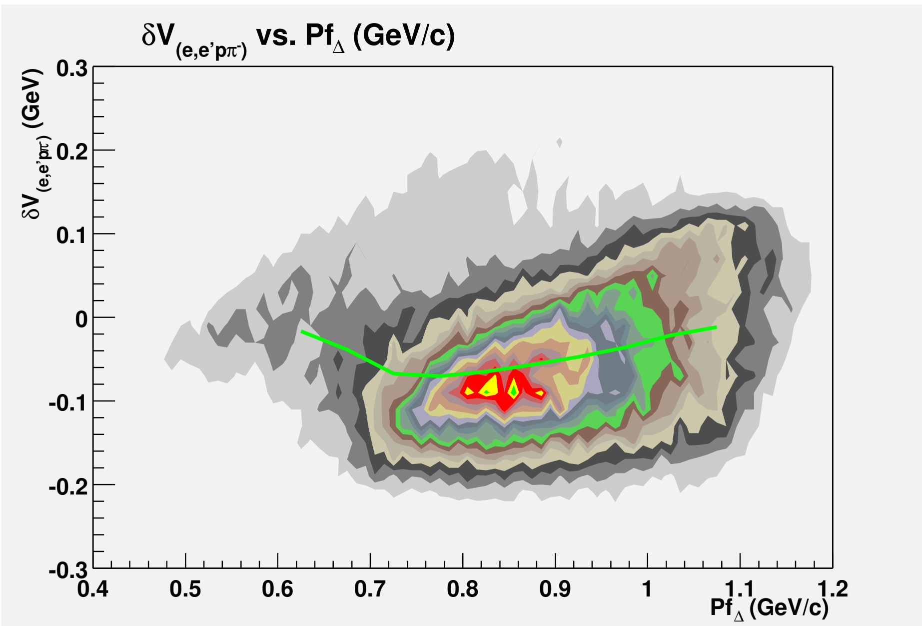

Figure 5.16: $\delta V_{(e,e'p\pi^-)}$ with p_f(using $M_\Delta = 1.232$)

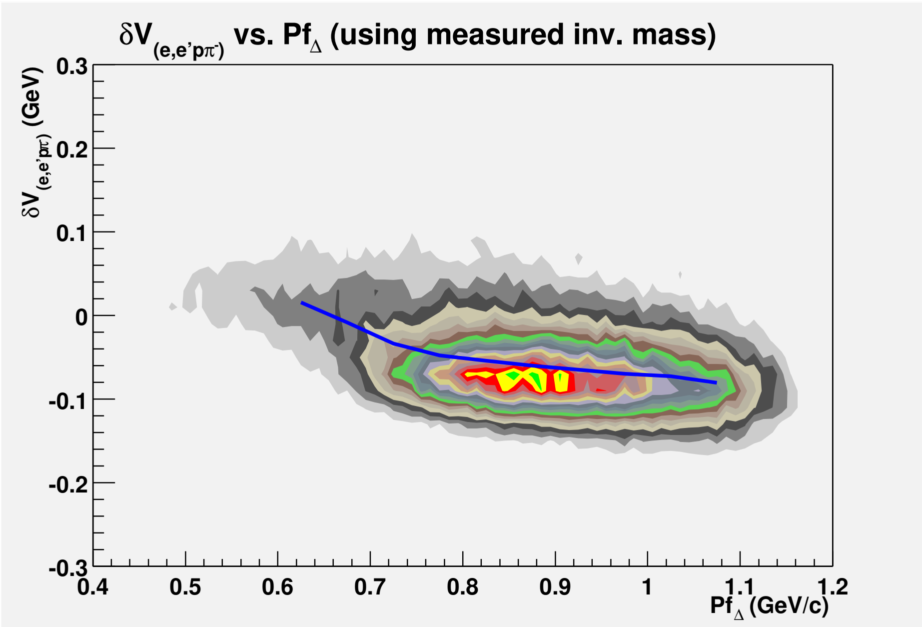

Figure 5.17: $\delta V_{(e,e'p\pi-)}$ with p_f (using measured M_Δ)

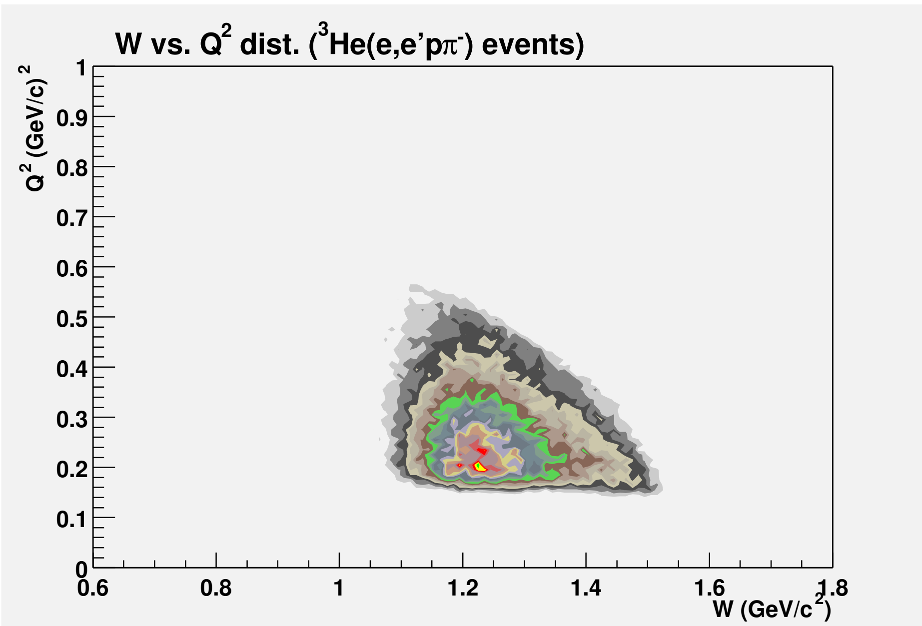

Figure 5.18: W vs. Q^2, for $(e, e'p\pi^-)$ events

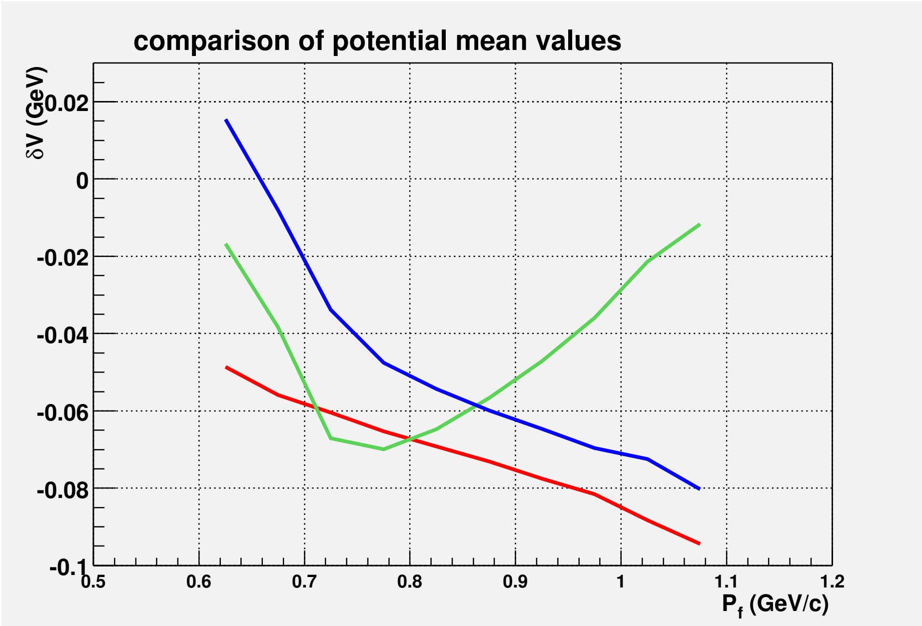

Figure 5.19: Comparison of mean-lines
Shown are the mean values of $\delta V$for the $^3He(e,e'p)$ channel (red), the $^3He(e,e'p\pi^-)$channel where $M_\Delta = 1.232GeV/c^2$(green) and the $^3He(e,e'p\pi^-)$channel where $M_\Delta$is measured on an event by event basis (blue).

5.29 through to 5.31). These fit parameters are presented in terms of the structure functions from which they are defined (see section 4.7). The units for these structure functions come from the ϕ^* distributions which are expressed in terms of yield modified by the acceptance correction. Hence we present relative values for the structure functions for both the $^3He(e,e'p\pi^-)$ and the $^3He(e,e'p\pi^0)$ i.e. their relative shapes can be compared.

It must be noted that the range of θ^* values available depends upon the acceptance of CLAS, and since photons are only detected in the EC, the θ^* range for the $^3He(e,e'p\pi^0)$ channel is restricted.

There are a number of measured ϕ^* distributions for both channels for which fits are not shown. Because of poor statistics, the data are not of a quality to be fitted by the angular distribution function.

Also a number of the ϕ^* distributions are fitted over restricted ranges, again due to lack of statistics in the data. Some plots are shown using a ϕ^* range from $180^o - 540^o$, as opposed to the $0^o - 360^o$ range which is standard. This is to improve the quality of the fit and relies upon the cyclical nature of the distribution. Tests were undertaken to ensure that this approach to the fitting did not affect the parameters derived from the fits.

The uncorrected distributions expected from the MAID code are shown in figure 5.20 for the $^3He(e,e'p\pi^-)$ and the $^3He(e,e'p\pi^0)$ channel. The $\phi^* vs. \theta^*$ distributions as predicted by MAID are shown. Both the pure P_{33} and pure Born terms are shown for the $^3He(e,e'p\pi^-)$

channel, but only the pure P_{33} resonance for the $^3He(e, e'p\pi^0)$ channel (as Born terms are suppressed). The differences between the P_{33} and the Born term distributions are noteworthy. The degree to which the characteristics of either calculated distribution manifests itself in the data may allow some estimation of the contributions from Born terms. This is discussed more fully at the end of this section. It is also apparent that the P_{33} distributions for both the $^3He(e, e'p\pi^-)$ and $^3He(e, e'p\pi^0)$ channels are very similar.

5.3.1 $^3He(e, e'p\pi^-)$ events

The plots of $\phi^*$are presented for θ^* intervals of 0.2 radians. Each ϕ^* bin is of width 30^o. The plots are shown in figures 5.21 through to 5.28. It should be noticed that the ϕ^* range is not the standard $0 - 360^o$ for some plots, but the ϕ^* range is $180 - 540^o$(as discussed in section 5.3). Where this is the case the plot in question is annotated appropriately.

The structure functions for the $^3He(e, e'p\pi^-)$ channel.

The experimental and MAID calculations for pure P_{33} and pure Born for the function $\sigma_T + \epsilon\sigma_L$ are shown in figure 5.29. The corresponding values for σ_{TT} are shown in figure 5.30 and for σ_{LT} in figure 5.31. As can be seen the three structure functions vary dramatically between the pure Born terms and the pure P_{33} resonance. For $\sigma_T + \epsilon\sigma_L$ the experimental structure function is biased toward forward angles. From the shapes of the theoretical curves, the experimental functions clearly contain significant contributions from both P_{33} and Born terms. For σ_{TT} both theoretical curves have similar negative forms which have maximum magnitude around $\theta^* = 90^o$. The experimental curve has a similar negative feature but has maximum magnitude at around $\theta^* = 60^o$. Perhaps this results from interference between the P_{33} and Born terms or is due to medium effects in ^3He. The theoretical shapes for σ_{LT} are quite different from the experimental shape. Again this could be due to interference or nuclear effects. Without a thorough acceptance correction and theoretical treatment only tentative conclusions can be made.

5.3.2 $^3He(e, e'p\pi^0)$ events

The same layout is used for the $^3He(e, e'p\pi^0)$ channel as for the previous $^3He(e, e'p\pi^-)$ channel (shown in figures 5.32 through to 5.36.). There are only ten ϕ^* distributions presented in the θ^* range 0.0 - 2.0 radians. This is a result of the requirement that both of the $\gamma's$ from the π^0 must be detected in the EC and this limits the available θ^* range to forward angles (θ^* and θ_{lab} are different, as θ^* is measured relative to the virtual photon. Despite this, the two angles are related as the virtual photon does tend to be very biased

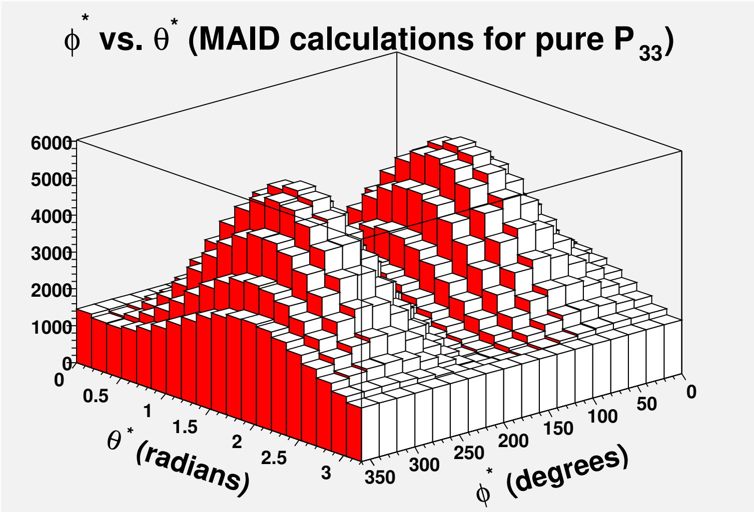

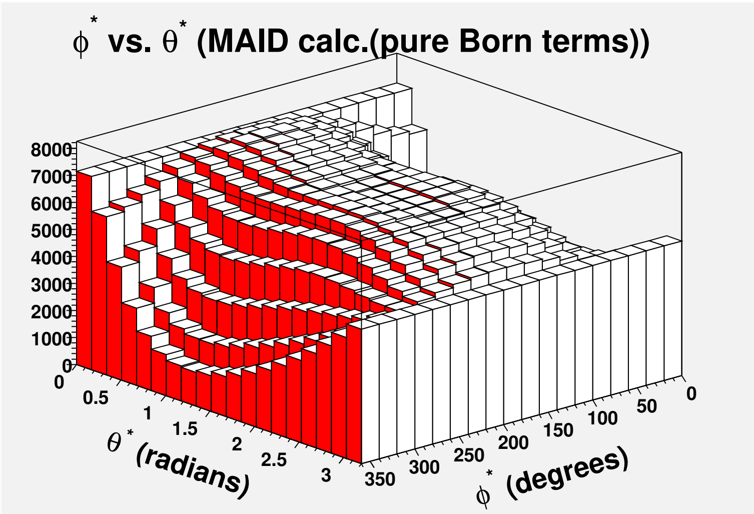

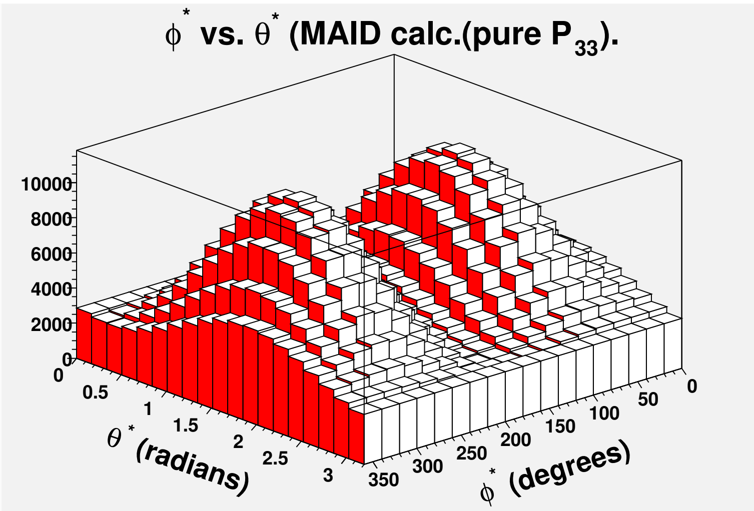

Figure 5.20: MAID calculations of the ϕ^*vs θ^*distributions for the $p\pi^-$ and $p\pi^0$ decay channel.
Pure P_{33} contributions to the $^3He(e, e'p\pi^-)$ channel in the top figure, pure Born contributions to the $^3He(e, e'p\pi^-)$ channel in the middle figure and the pure P_{33} contribution to the $^3He(e, e'p\pi^0)$channel in the bottom figure.

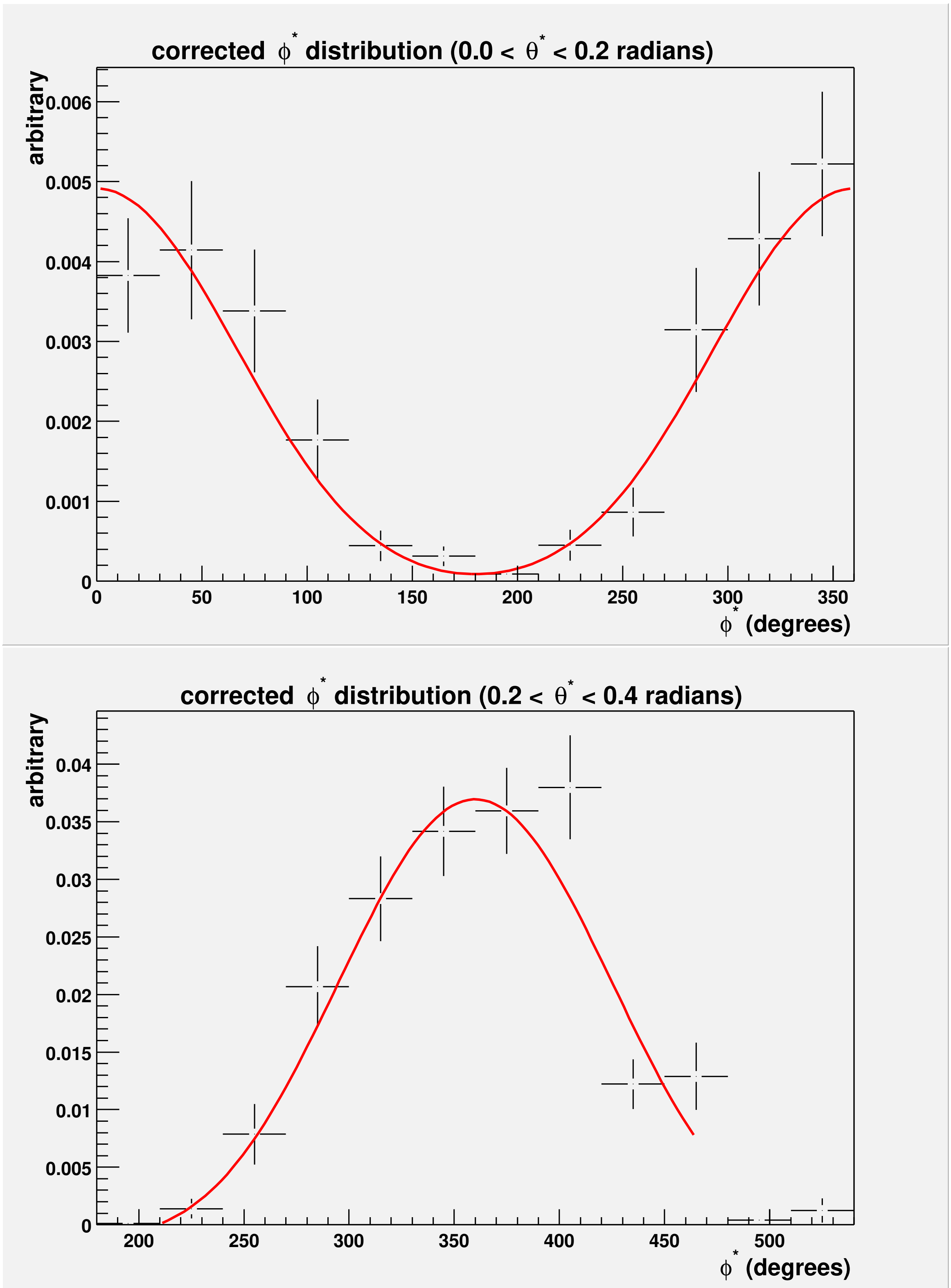

Figure 5.21: ϕ^* distributions for $p\pi^-$ channel(1,2)

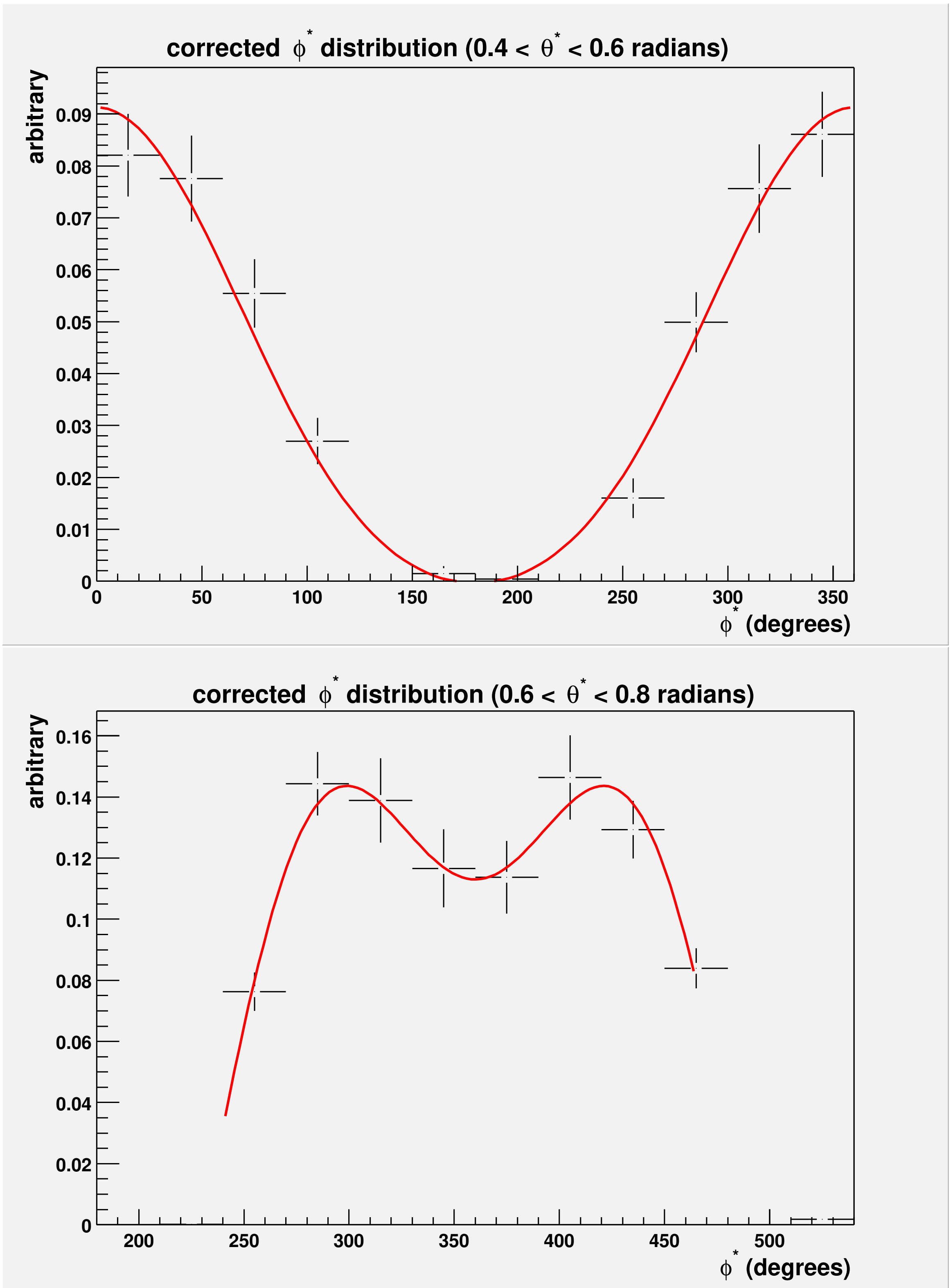

Figure 5.22: ϕ^* distributions for $p\pi^-$ channel(3,4)

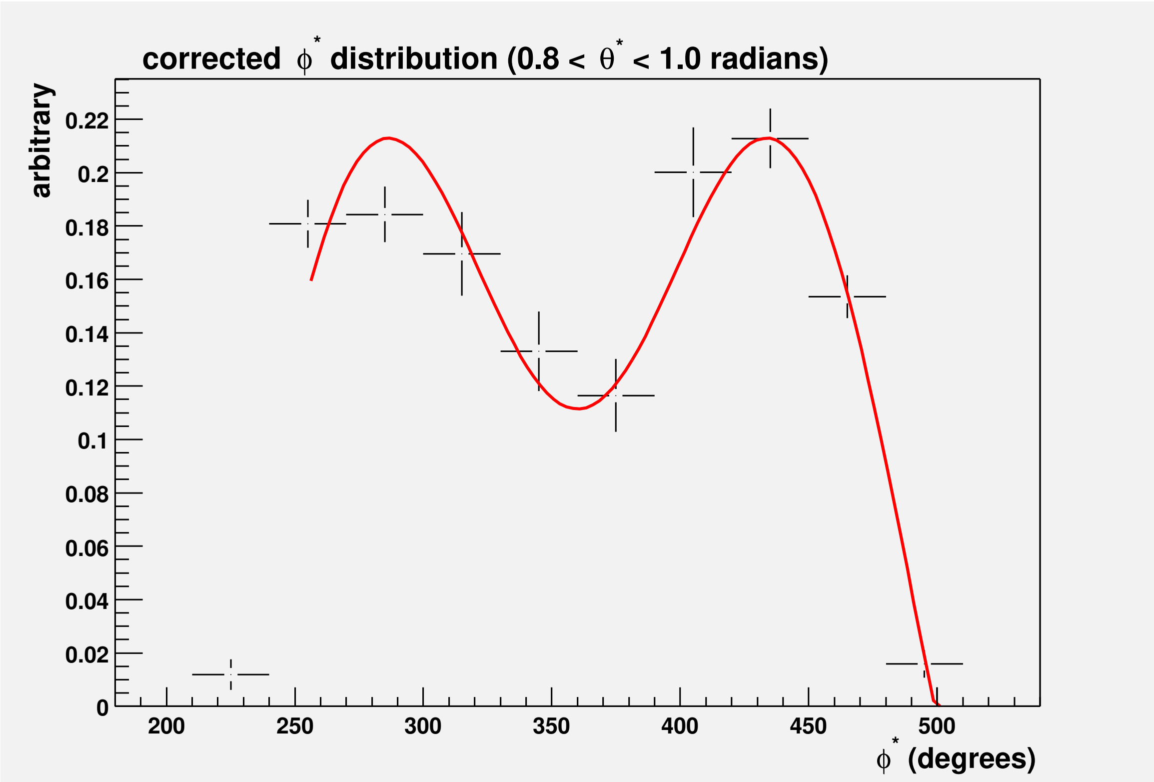

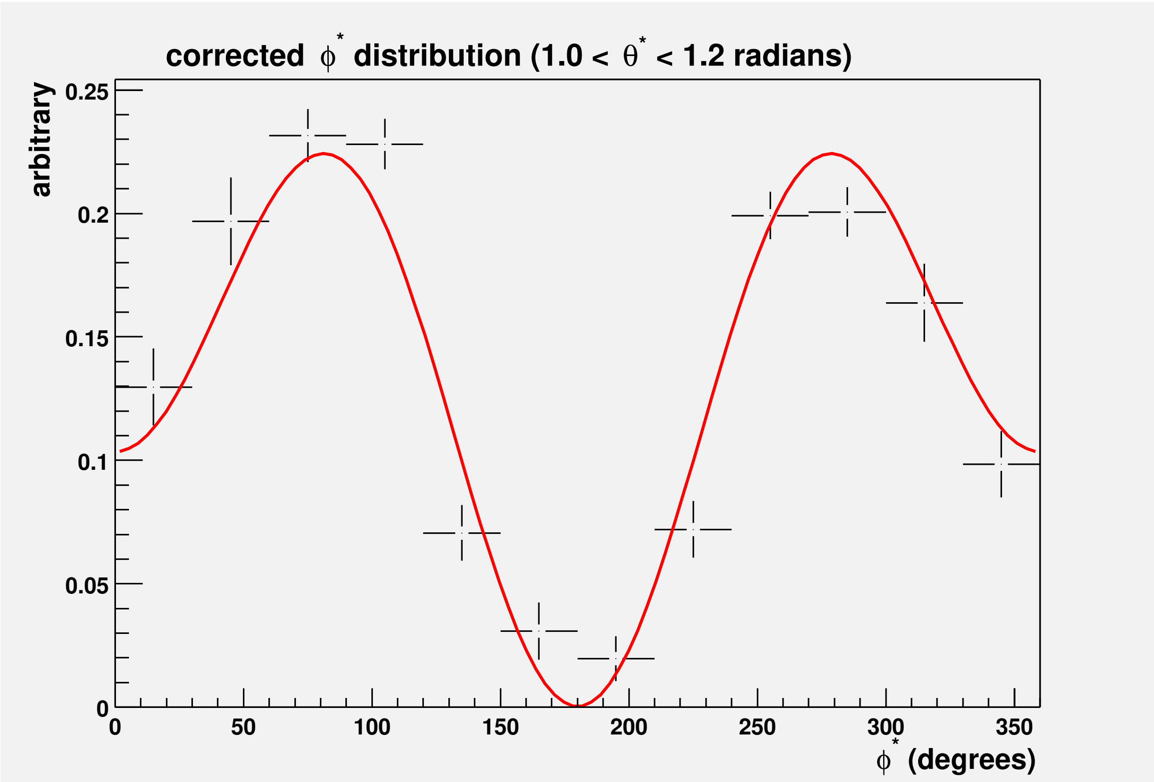

Figure 5.23: ϕ^* distributions for $p\pi^-$ channel(5,6)

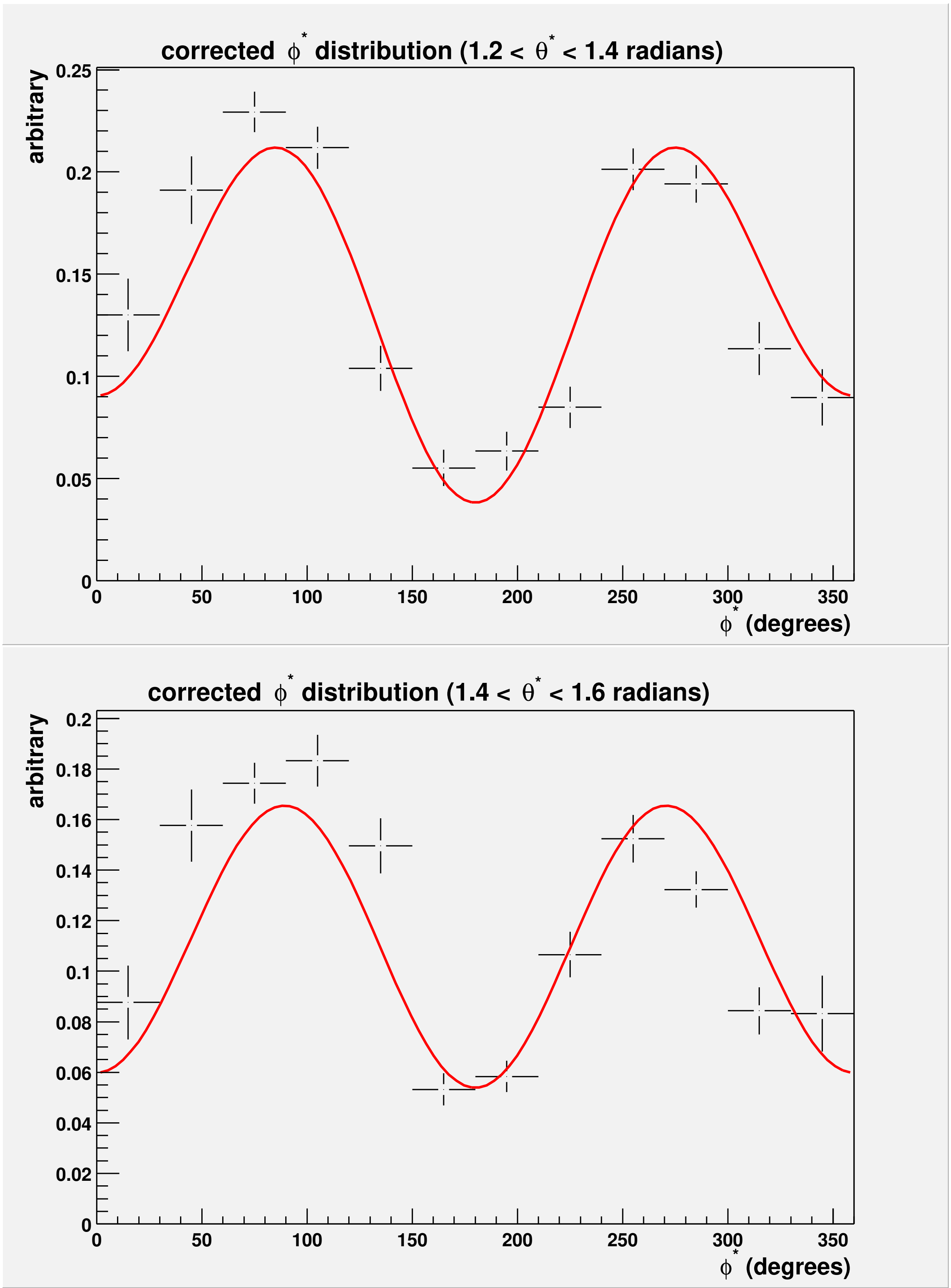

Figure 5.24: ϕ^* distributions for $p\pi^-$ channel(7,8)

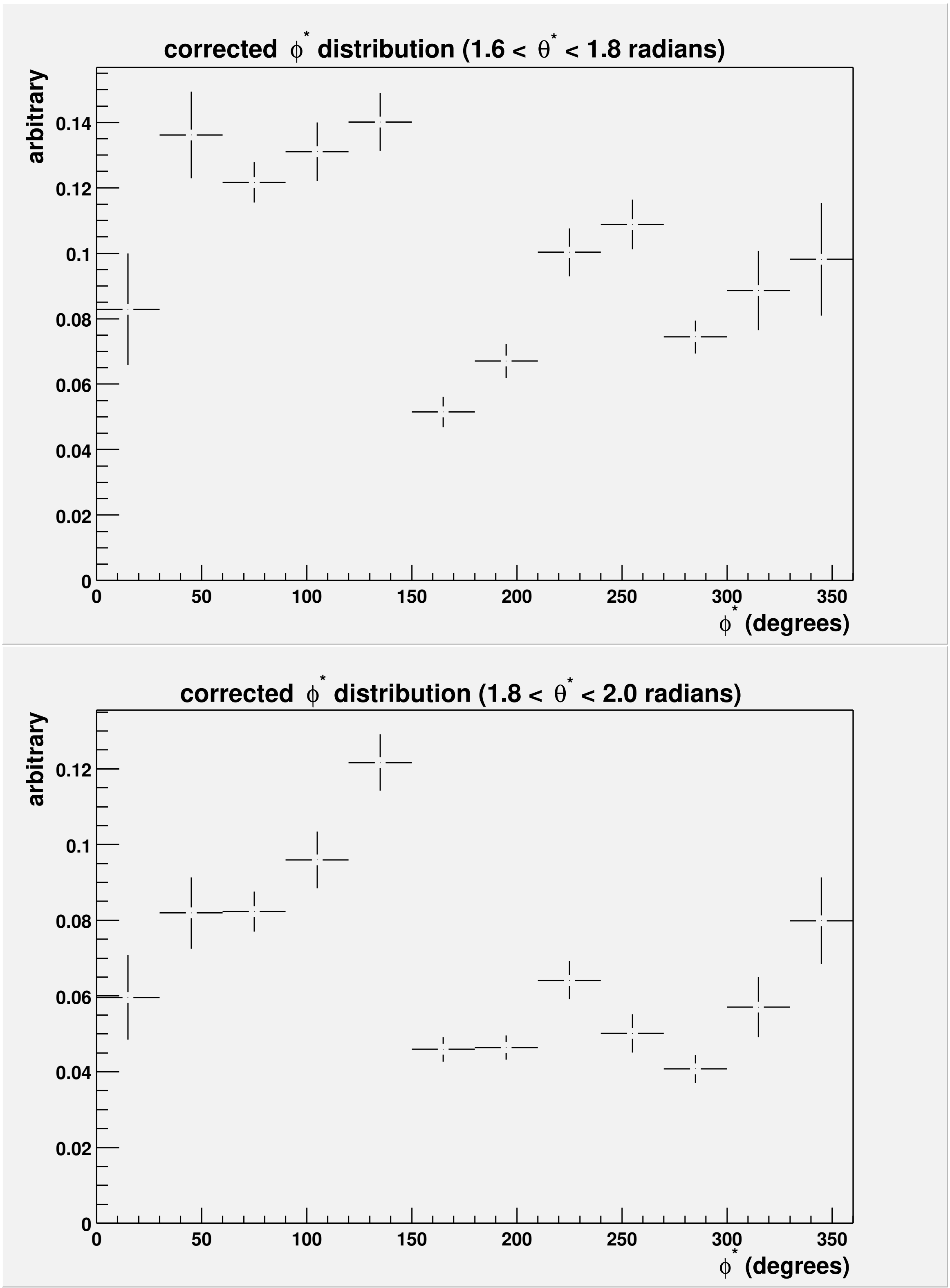

Figure 5.25: ϕ^* distributions for $p\pi^-$ channel(9,10)

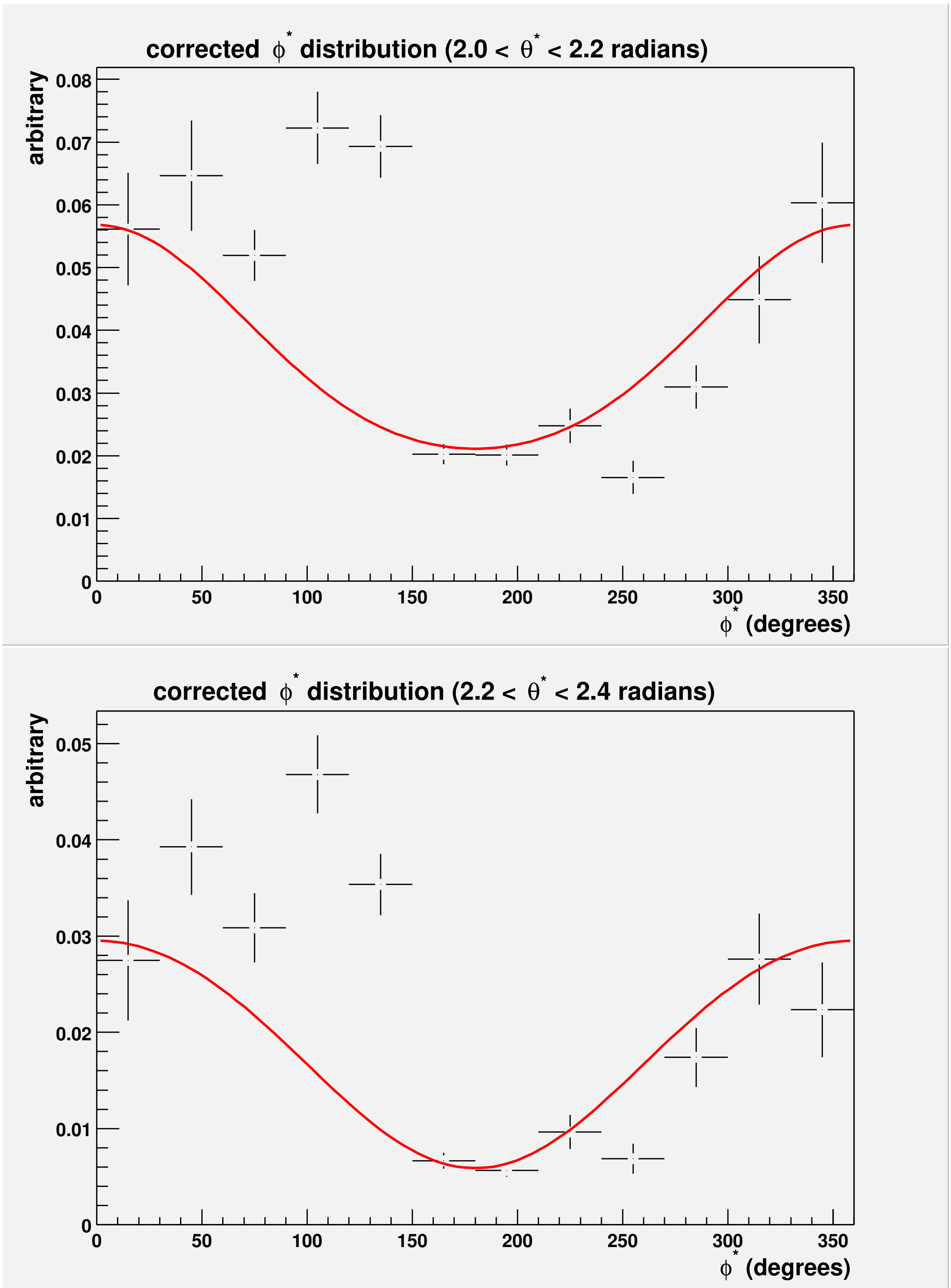

Figure 5.26: ϕ^* distributions for $p\pi^-$ channel(11,12)

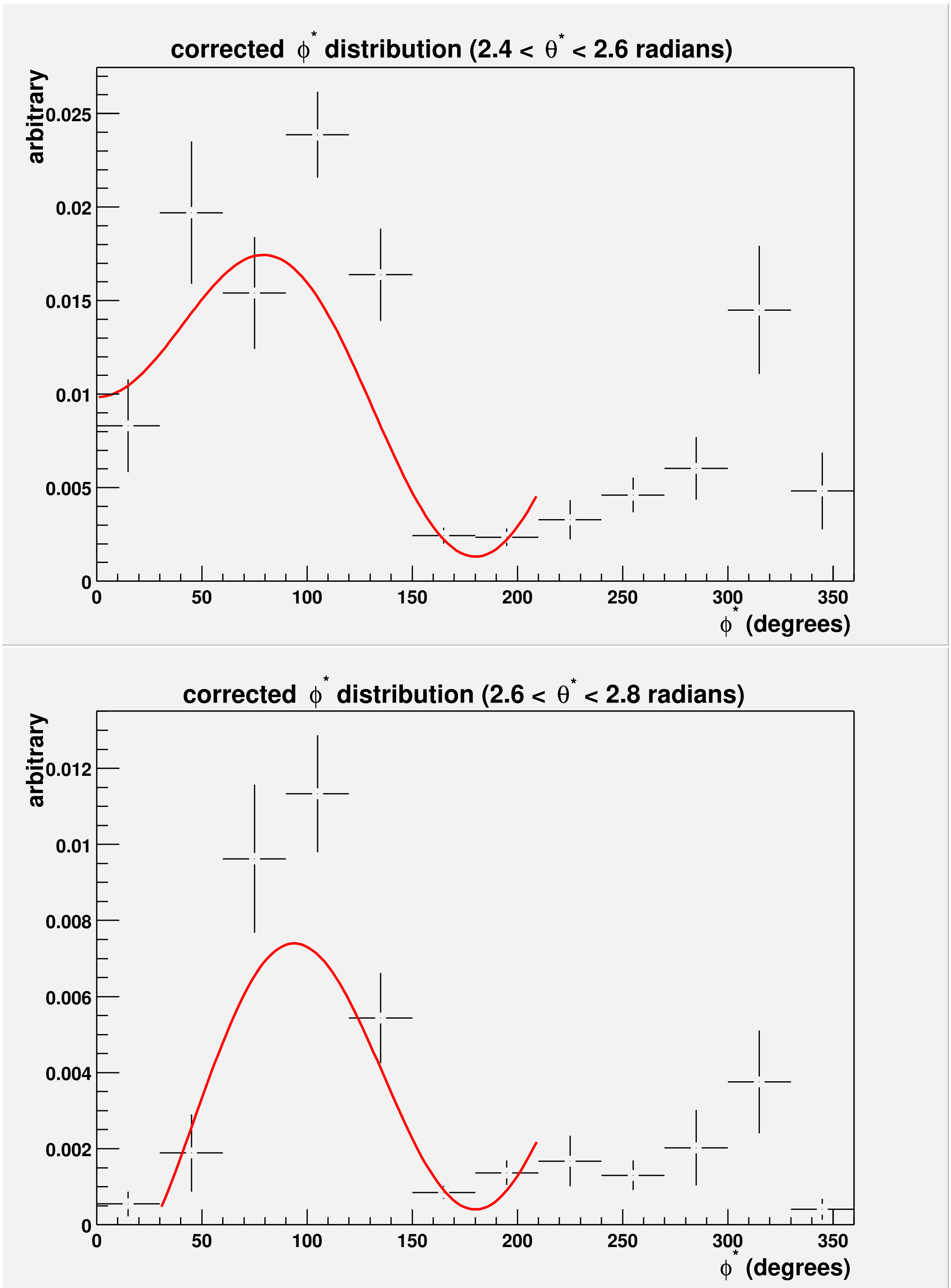

Figure 5.27: ϕ^* distributions for $p\pi^-$ channel(13,14)

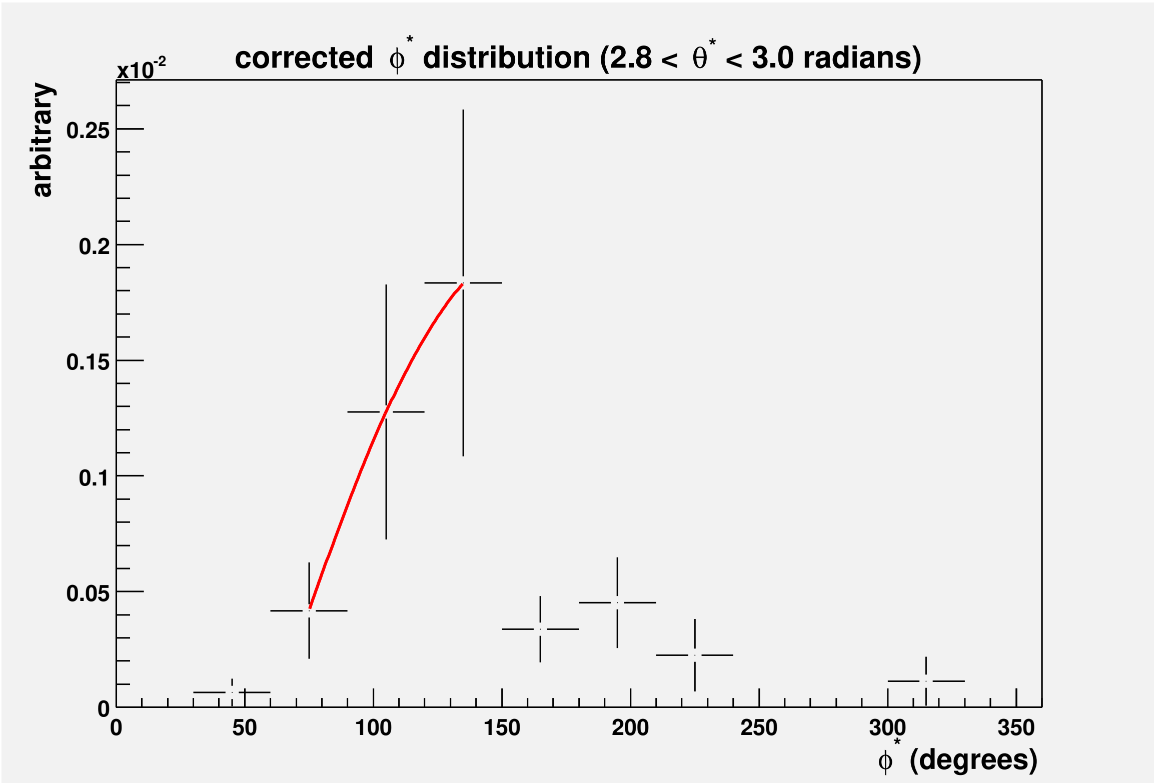

Figure 5.28: ϕ^* distributions for $p\pi^-$ channel(15)

toward forward angles, resulting in a correlation between low θ_{lab} and low θ^*). Due to the acceptance of CLAS for detecting photons and the difficulties arising in detecting two $\gamma's$, the statistics for the $^3He(e, e'p\pi^0)$ channel are significantly less than for the $^3He(e, e'p\pi^-)$ channel. As a result the measurements beyond the $0.8 < \theta^* < 1.0$ radians range are not of sufficient quality to be fitted.

The structure functions for the $^3He(e, e'p\pi^0)$ channel.

The structure functions are shown alongside their corresponding MAID calculation in figures 5.37, 5.38 and 5.39. The experimental ranges are limited due to the response of CLAS to $\gamma's$ as discussed above. The MAID calculations shown are for the P_{33} resonance alone as non-resonant production of neutral pions is suppressed.

5.3.3 Comparison of $^3He(e, e'p\pi^-)$ and $^3He(e, e'p\pi^0)$.

The comparison of the $^3He(e, e'p\pi^-)$ and $^3He(e, e'p\pi^0)$ channels is limited by the reduced range of θ^* available for the $^3He(e, e'p\pi^0)$ channel.

The experimental plots of $\sigma_T + \epsilon\sigma_L$ for the two channels are both positive. However, whereas $\sigma_T + \epsilon\sigma_L$ is more forward peaked than the pure P_{33} curve for the $p\pi^-$channel,

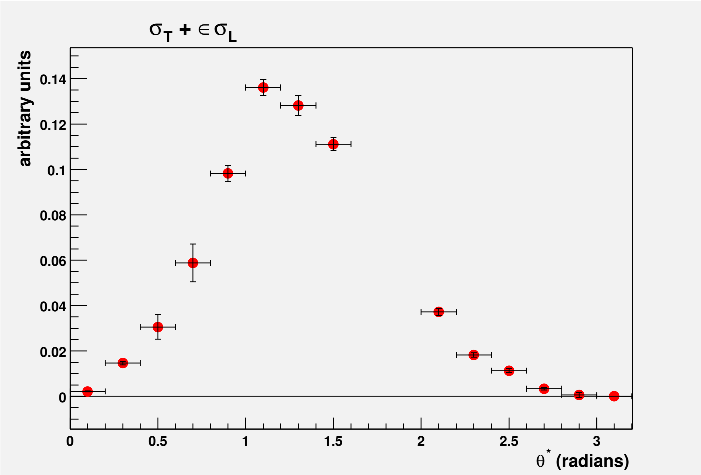

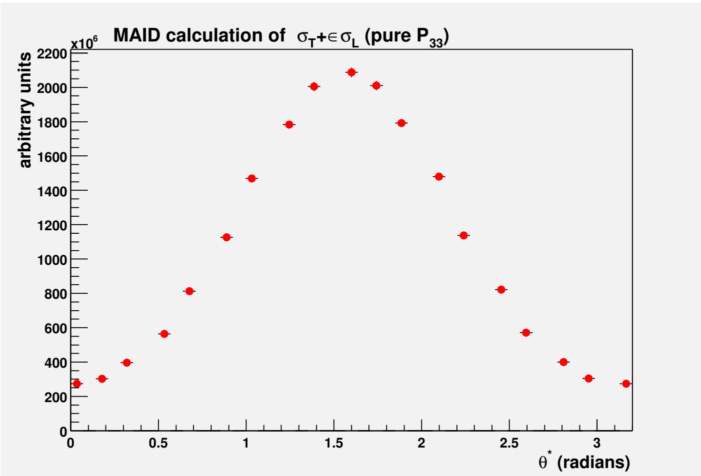

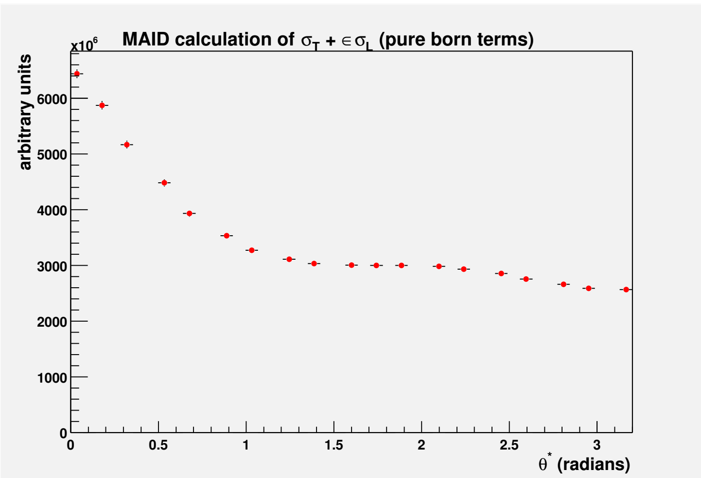

Figure 5.29: $\sigma_T + \epsilon\sigma_L$ for $p\pi^-$ channel

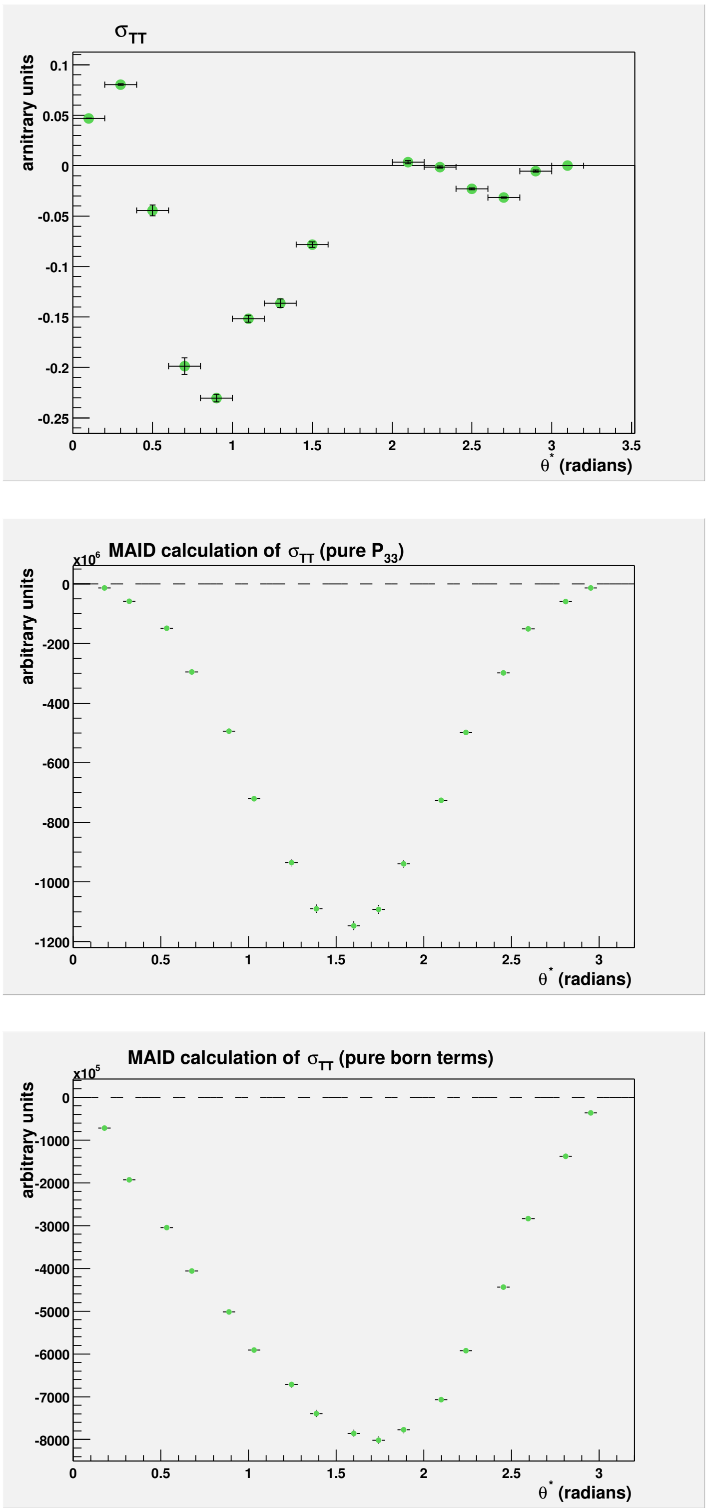

Figure 5.30: σ_{TT} for $p\pi^-$ channel

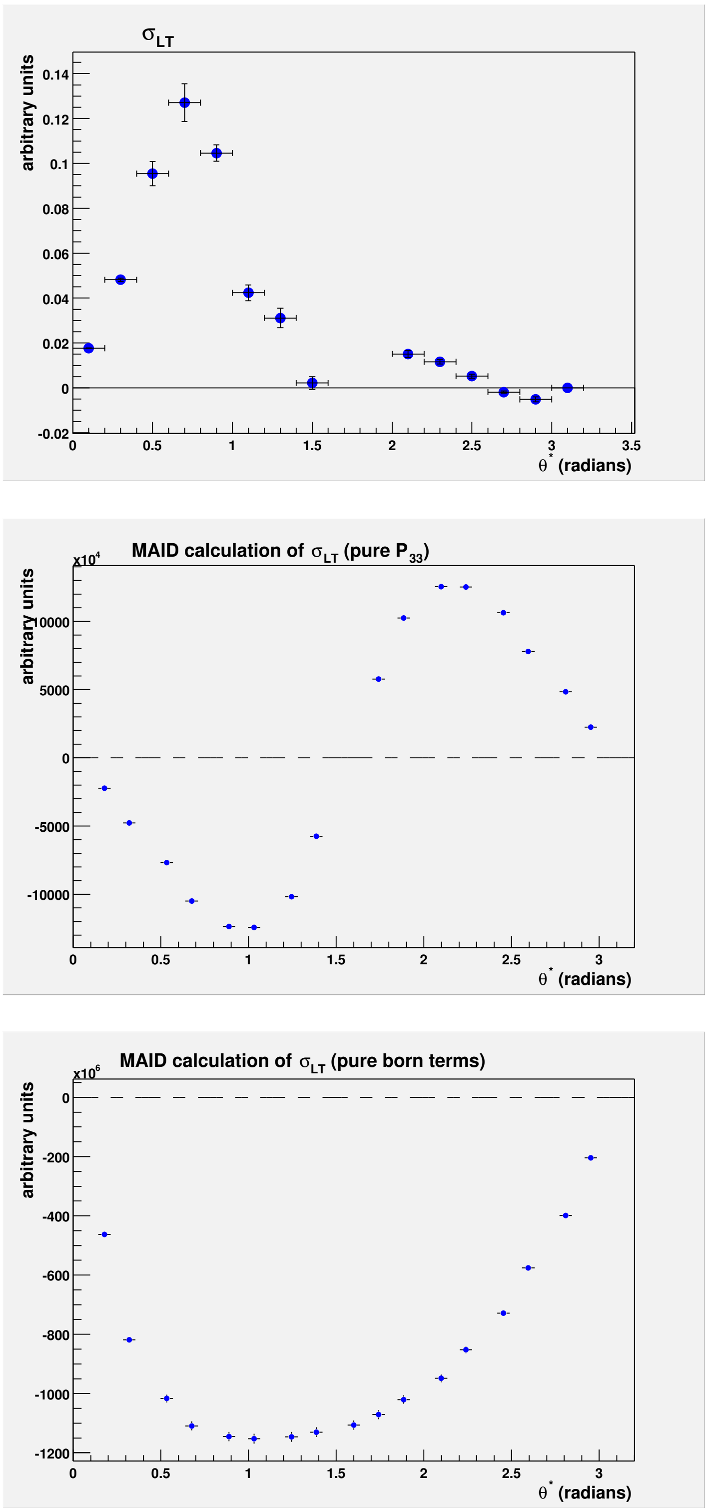

Figure 5.31: σ_{LT} for $p\pi^-$ channel

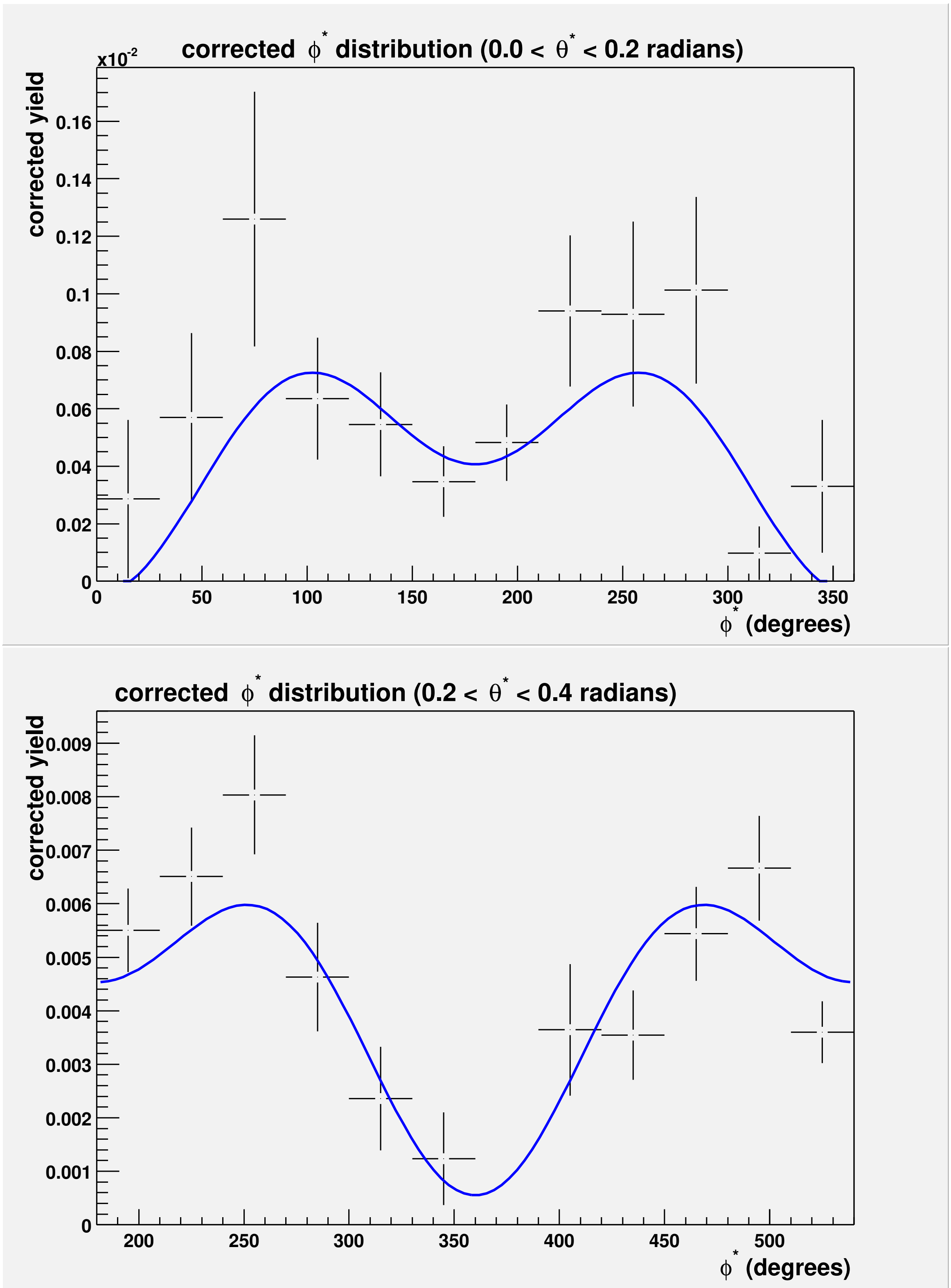

Figure 5.32: ϕ^* distributions for $p\pi^0$ channel(1,2).

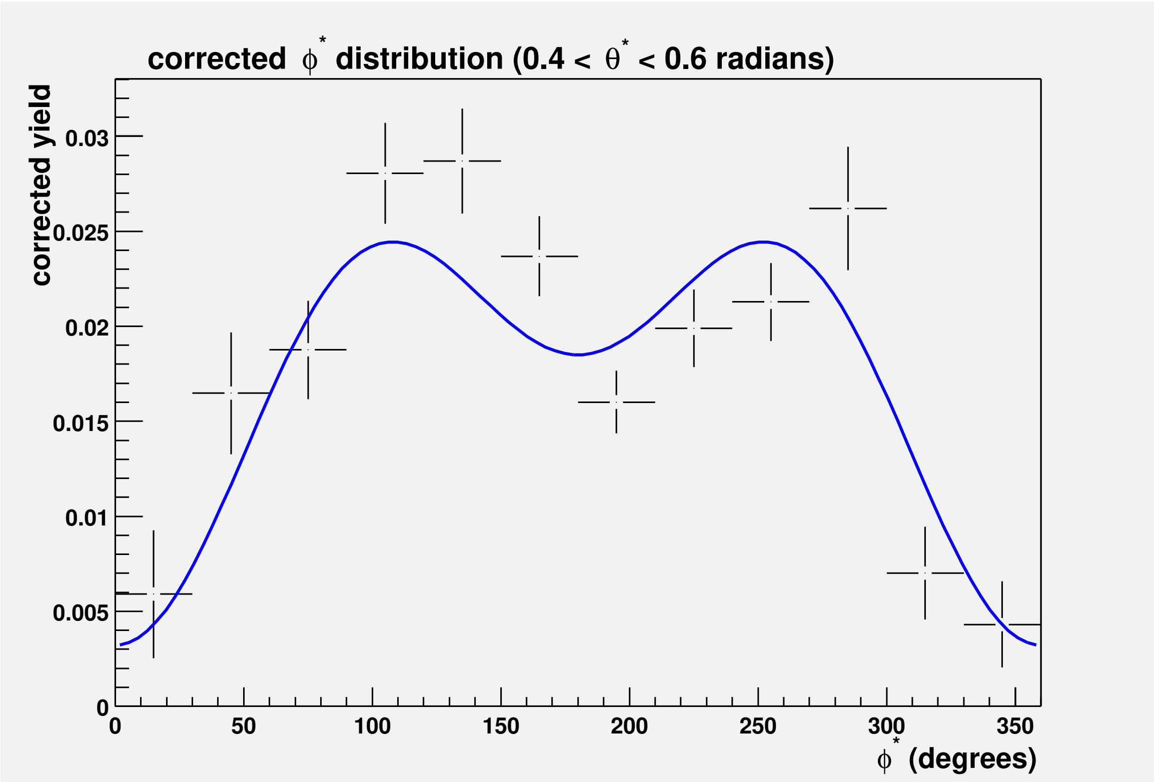

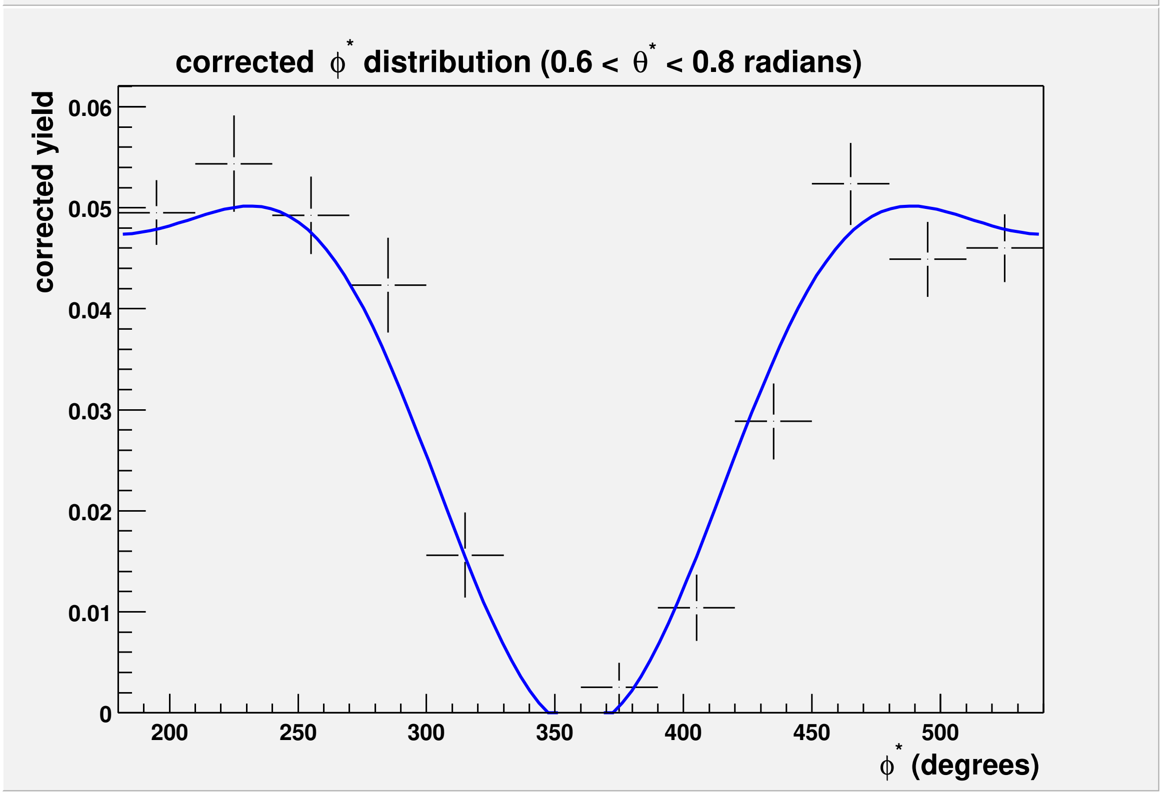

Figure 5.33: ϕ^* distributions for $p\pi^0$ channel(3,4).

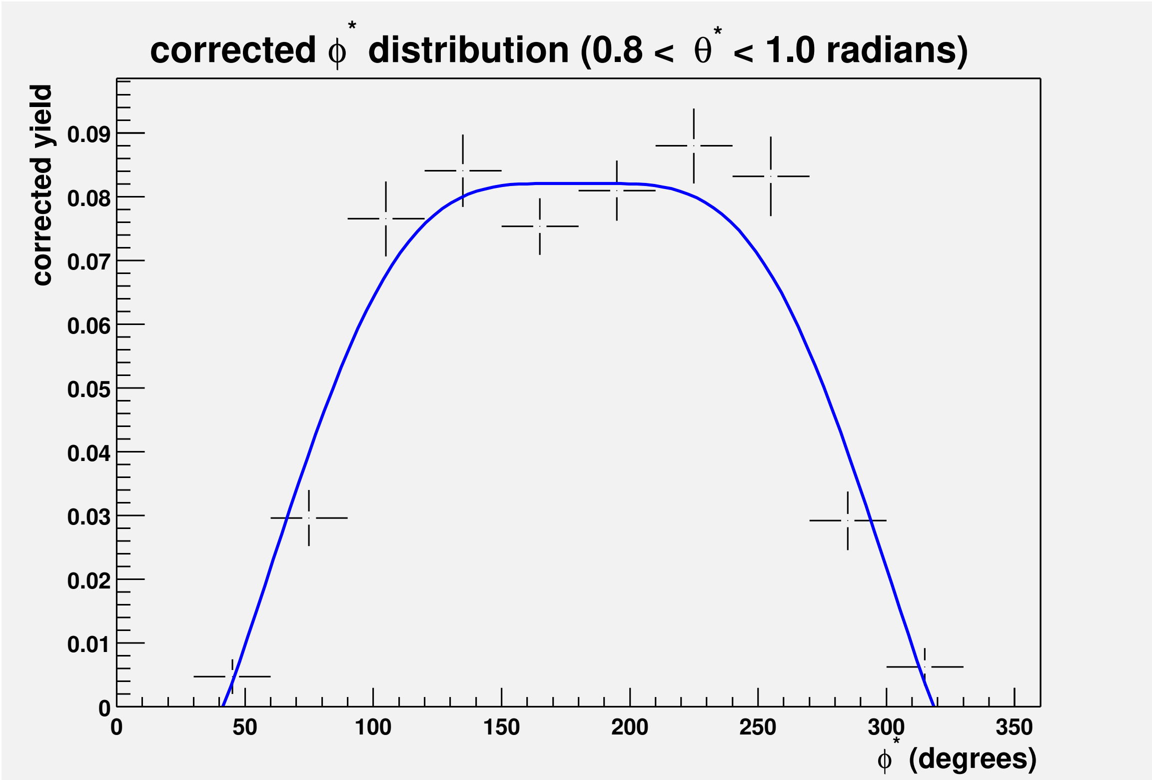

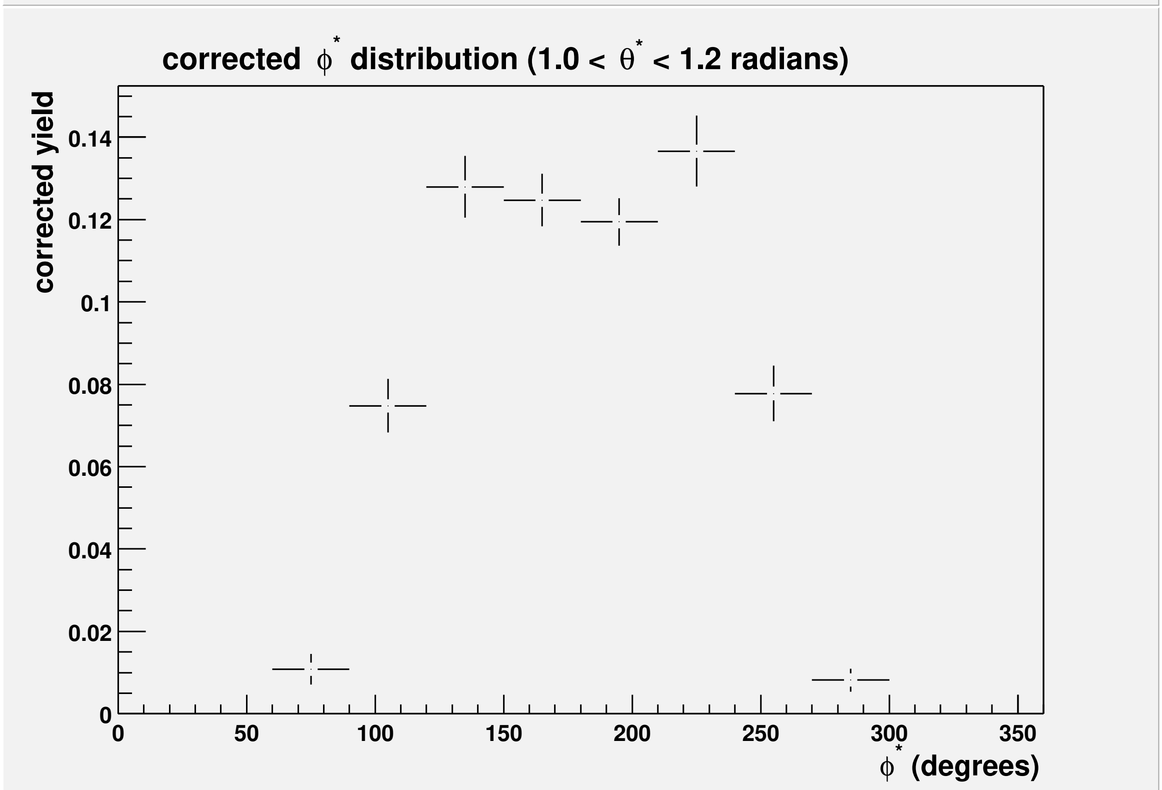

Figure 5.34: ϕ^* distributions for $p\pi^0$ channel(5,6).

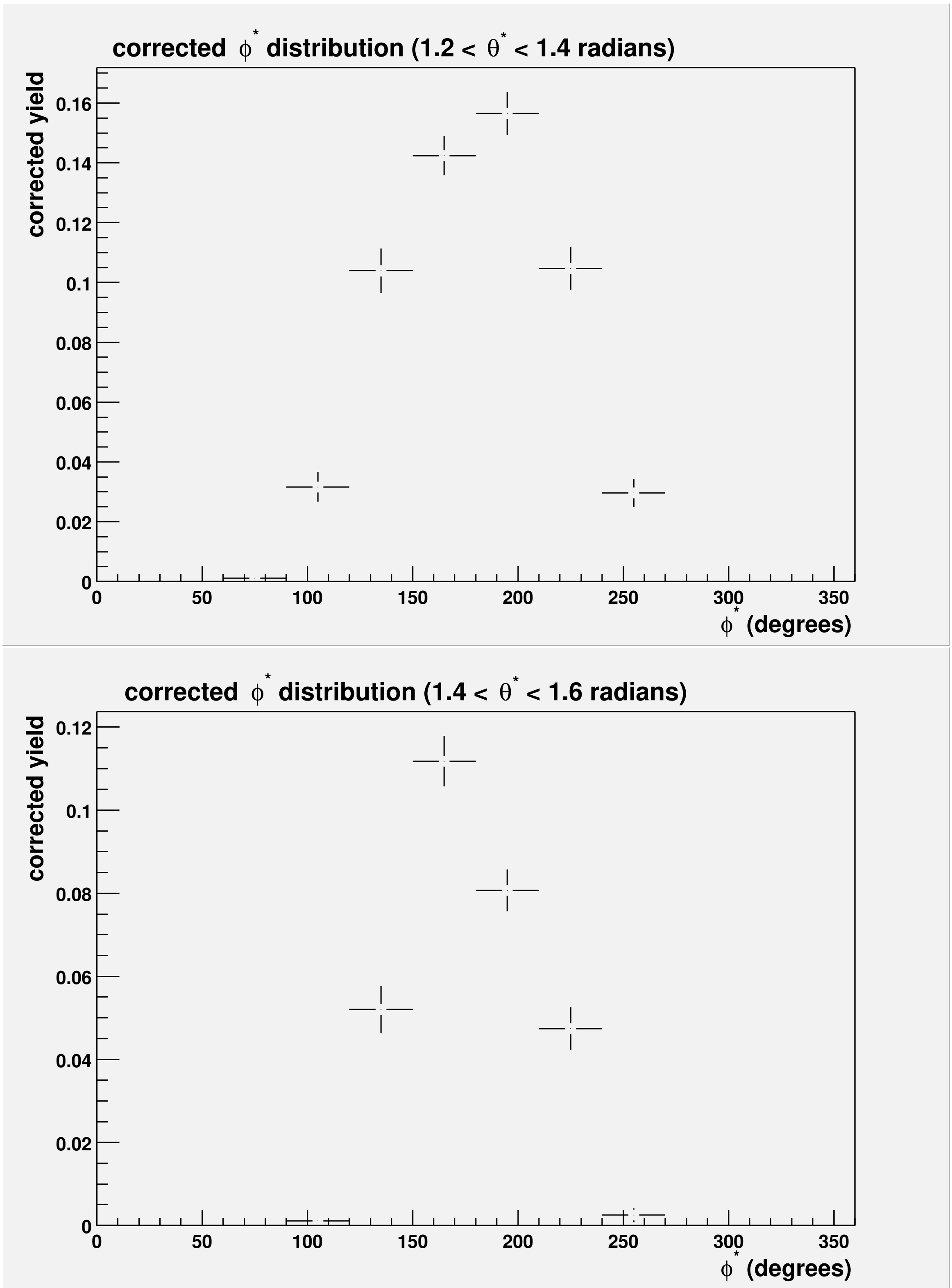

Figure 5.35: ϕ^* distributions for $p\pi^0$ channel(7,8).

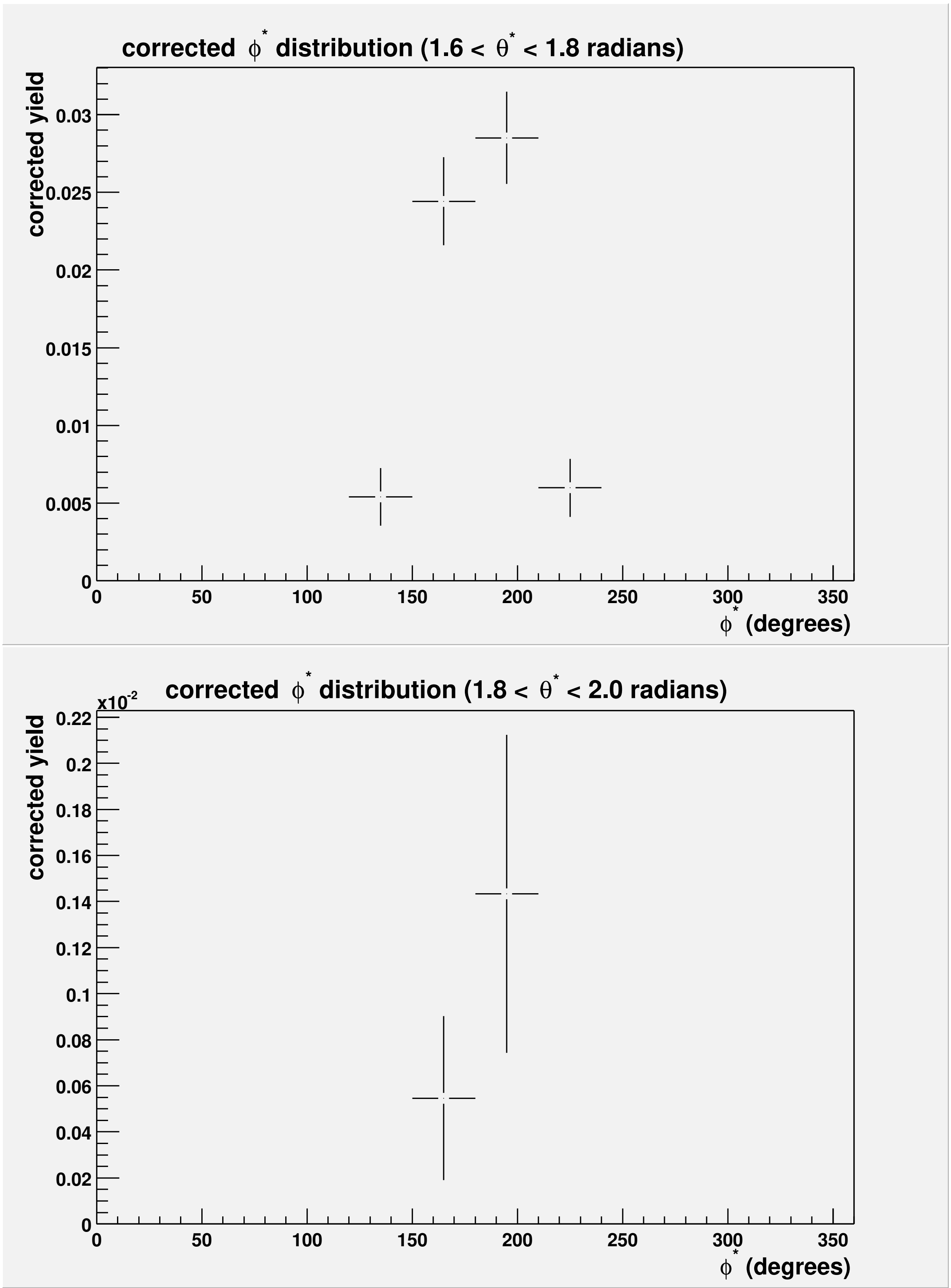

Figure 5.36: ϕ^* distributions for $p\pi^0$ channel(9,10).

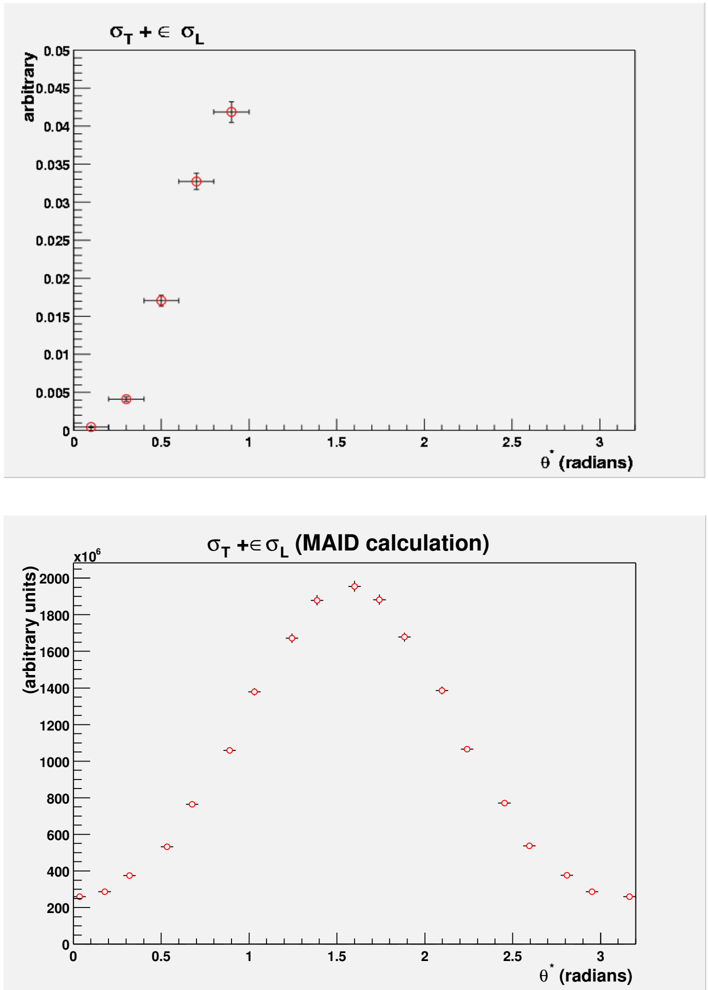

Figure 5.37: $\sigma_T + \epsilon\sigma_L$ for $p\pi^0$ channel.

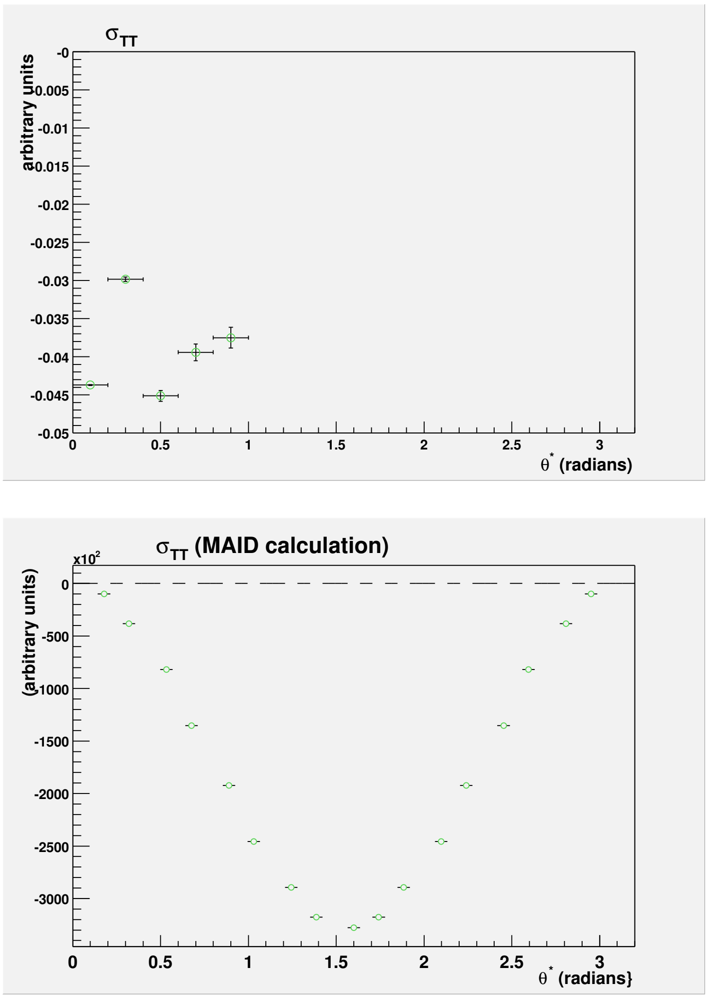

Figure 5.38: σ_{TT} for $p\pi^0$ channel.

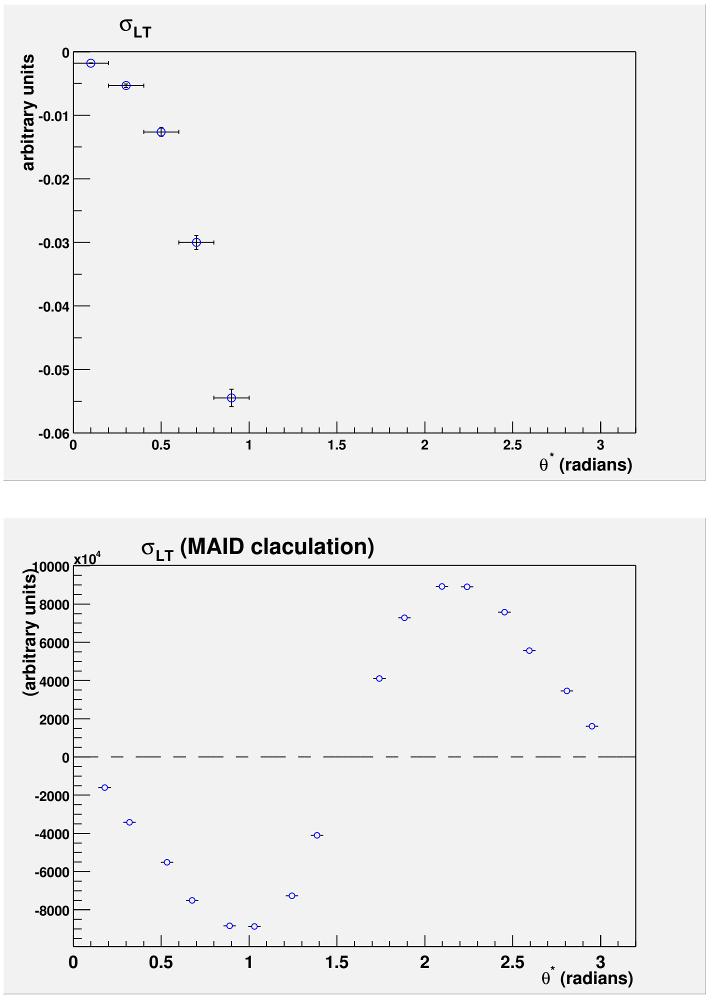

Figure 5.39: σ_{LT} for $p\pi^0$ channel.

it is plausible there will be a better level of agreement for the $p\pi^0$ channel.

The experimental plots of σ_{TT} also appear to be different. The $^3He(e, e'p\pi^-)$ channel exhibits a change in sign at low θ^*, which is not present with the $^3He(e, e'p\pi^0)$ channel.

It is the experimental σ_{LT} plots which differ most obviously. The $^3He(e, e'p\pi^-)$ channel is positive throughout most of its θ^*range and positive and increasing throughout the total range available to the $^3He(e, e'p\pi^0)$ channel. In contrast to this the $^3He(e, e'p\pi^0)$ plot is negative and decreasing throughout the same range.

This suggests there is a difference between the electro-excitation process of the Δ^0 and Δ^+resonances. If this is the case this finding would be quite significant. Unfortunately without a more complete experimental analysis, and improved theoretical calculations, any conclusions must remain speculative.

The comparison of this data with the MAID calculations; which assume a single nucleon target, have shown some differences between the electro-excitation of the Δ from a nucleon in the nucleus and the free nucleon target.

However the limitations of the present acceptance correction will affect all the results. Also the fact that γ pairs from the π^0 decay must be detected in the EC means that the range of θ^* for the $^3He(e, e'p\pi^0)$ channel is severely limited. These two CLAS effects restrict the reliability of the results. However once full acceptance corrections are applied better results will be obtained. Furthermore, a new experimental run was completed in June 2002 which increases the statistics considerably.

5.4 Conclusions.

The purpose of this study was originally to investigate the observations by Sealock et al.[1] from inclusive electron scattering experiments that the invariant mass of the $\Delta(1232)$ resonance increases significantly with Q^2. The present measurements using CLAS have delivered results over a broad range of phase space for both the $^3He(e, e'p\pi^-)$ and the $^3He(e, e'p\pi^0)$ channels. Since CLAS is an unusually complex detector, understanding the effect of the CLAS acceptance (including geometrical coverage, detection efficiencies and the effects of event reconstruction) on the results is similarly complex. The approach to acceptance corrections taken (corrections for geometrical coverage alone) in this work means that the results presented here are not final but are of sufficient accuracy to be indicative of the physics processes they relate to. Before final statements can be made about the electro-production of the $\Delta(1232)$ in ^3He, a full acceptance correction must be completed.

Nevertheless, any improvement of the acceptance correction will impose a refinement upon the results shown here and are unlikely to change them significantly.

In conclusion it appears that the invariant mass of the $\Delta^+(1232)$ and $\Delta^0(1232)$ do not increase with Q^2 during electro-production. If there is any variation with Q^2 it appears that the invariant mass decreases with Q^2; the opposite effect to the Sealock observation, although this effect is slight and may be due to the variation of the background discussed earlier. A more thorough theoretical approach to the contributions to the $^3He(e, e'p\pi^-)$ and $^3He(e, e'p\pi^0)$ channels is also necessary to decide upon the true behaviour of these invariant mass distributions.

The investigation of the angular distributions of the decay products of the $\Delta(1232)$ resonance in the $^3He(e, e'p\pi^-)$ and $^3He(e, e'p\pi^0)$ channels is similarly limited by the acceptance problem. It is also limited by the range of θ^* available with the $^3He(e, e'p\pi^0)$ channel. To increase this range more statistics are required. This means more beam time. The second run period of the e2 run group (e2b) has collected significantly more data with a 0.98 GeV beam on ^3He. This should provide a better comparison between the two channels studied here. At present it looks probable that there is a difference between the two channels in terms of the structure functions, especially the σ_{LT} structure function.

The study of the momentum dependence of the potential experienced by the proton and Δ^0 suggests that the magnitude of the mean value of $\delta V_{(e,e'p\pi^-)}$ is greater than $\delta V_{(e,e'p)}$ by approximately 15 MeV, based upon the most reliable area of the data set. This could be significant since it is relevant to the charge independence of nuclear forces, as the Δ^0 is excited from the neutron, and hence provides an interesting comparison to the proton result. Preferably the same analysis should be carried out with quasi-elastic neutron and Δ^+ electro-production then more direct comparisons would be possible. To produce high quality results for the neutron and the Δ^+ potentials, improved statistics are necessary due to the difficulty of detecting neutral particles in CLAS. The e2b run should provide a better data set for such an analysis.

Bibliography

[1] R. Sealock et al. Electroproduction of the $\Delta(1232)$ in nuclei. Proposal PR-89-017 to Jefferson lab., 1989.

[2] D. Drechsel and L. Tiator. Threshhold pion photoproduction on nucleons. *J. Phys. G*, 18:449–497, 1992.

[3] A song of ascents. Of Solomon. Psalm 127.

[4] Hugh D. Young. *University Physics*. Addison Wesley, 1992.

[5] Burcham and Jobes. *Nuclear and Particle Physics*. Longman Scientific & Technical, 1995.

[6] S. Boffi. *Electromagnetic Response of Atomic Nuclei*. Oxford Science Publications, 1996.

[7] N. Isgur. To reveal the quark structure of matter. *Nuclear Physics A*, (623):37–55, 1997.

[8] Volker D. Burkert. Electromagnetic excitation of nucleon resonances. In *14th International IUPAP Conferance on few body problems in physics, available from JLab Library*, May 1994.

[9] Volker D. Burkert. Leptonic production of baryon resonances. In M. N. Harakah et al., editor, *Perspectives in the Structure of Hadronic Systems*, pages 101–139, New York, 1994. Plenum Press.

[10] H. Baghaei et al. Electroexcitation of the Δ resonance in the (e,e'p) reaction. *Physical Review C*, 39(1), 1989.

[11] D. T. Baran. Δ electroproduction and inelastic charge scattering from carbon and iron. *Physical Review letters*, 61(4), 1988.

[12] P. Barreau et al. *Nuclear Physics A*, 402:515, 1983.

[13] R.W. Lourie et al. *Physical Review Letters*, 56:2368, 1986.

[14] Z.E. Meziani et al. *Physical Review Letters*, 54:1233, 1985.

[15] J.S. O'Connell et al. *Physical Review C*, 35:1063, 1987.

[16] J. S. O'Connell et al. Electron scattering in the excitation region of the delta resonance on nuclei with A=1 to 16. *Physical Review letters*, 53(17), 1984.

[17] Richard Sealock et al. Electroexcitation of the Δ(1232) in nuclei. *Physical Review Letters*, 62(12):1350 – 1353, 1989.

[18] Richard Sealock. Q^2 dependence of Δ electroexcitation in nuclei. In M. Ishihara H. Toki, M. Ichimura, editor, *DELTA EXCITATION IN NUCLEI*, page 59, Singapore, 1993. World Scientific.

[19] K. Joo et al. q^2 dependence of quadrupole strength in γ^*p -> Δ^+(1232) -> pπ^0 transition. *Physical Review Letters*, 88, 2002.

[20] J.S. O'Connell and R. M. Sealock. Phenomenological Δ-Nucleus potential from inclusive electron-nucleus scattering data. *Physical Review C*, 42(6):2290, 1990.

[21] H.P. Blok. Electron scattering, 1984. Lectures, Vrije Institute, Amsterdam.

[22] John LeRose et al. Direct measurement of the radiative tail in electron scattering from atomic nuclei. *Physical Review C*, 32(2):449–451, 1985.

[23] J. A. Templon. Radiative corrections to (e,e'p) reactions. In *1999 User Group Annual Meeting & Workshop*. Jefferson Lab workshop on "Radiative corrections in electron scattering for everyone".

[24] J. A. Templon. Radiation tail in (e,e'p) reactions and corrections to experimental data. *Physical Review C*, 61(014607), 1999.

[25] J. Lightbody and J.S. O'Connell. *Computers in Physics 2*, 57, 1988.

[26] G. Audit et al. Study of three-nucleon mechanisms in the photodisintegration of ^{3}He. *Nuclear Physics A*, (614):461–471, 1997.

[27] M. T. Pena et al. Three-nucleon force and the Δ mechanism for pion production and pion absorption. *Physical Review C*, 48(5):2208–2221, 1993.

[28] Peter Bartsch et al. Evidence for narrow Δ(1232) states in the $^{12}C(e,e'p\pi^-)^{11}C$ reaction. *The European Physical Journal A*, 4(3):209–216, 1999.

[29] K. I. Blomqvist et al. Forward-angle $^3He(e,e'p\pi^{+/-})$ coincident electroproduction and search for Δ's in the ground state of ^3He. *Physical Review letters*, 77(12):2396–2399, 1996.

[30] Mahmoud A. Hasan. Mean-field calculation of compressed finite nuclei with Δ excitations. *Physical Review C*, 56(6):3063–3069, 1997.

[31] Kenneth S. Krane. *Introductory Nuclear Physics*. John Wiley & sons, 1987.

[32] K. Hagiwara et al. Review of particle physics. *Phys. Rev. D66*, 2002.

[33] R. M. Davidson. Problems with extraction of the nucleon to $\Delta(1232)$ photonic amplitudes. *Physical Review C*, 59(2):1059–63, 1999.

[34] R. Beck. Measurement of the E2/M1 ration in the N-Δ transition using the reaction p(γ,p)π^0. *Physical Review letters*, 78(4):4509–4510, 1997.

[35] D. Branford et al. Nuclear pion photoproduction in the Δ resonance region. *Physical Review C*, 61:014603/1–9, 1999.

[36] D. Branford et al. Investigation of delta-medium effects using the ^{4}He(γ,π^+n)^{3}H and ^{4}He(γ,π^+p)nnn reactions. *Physical Review C*, 66, 2002.

[37] M. Kohl. Self energies of the pion and the Δ isobar from the ^{3}He(e,e'π^+)^{3}H reaction. *Physics Letters B*, 530:67 – 73, 2002.

[38] D. Contardo et al. *Physics Letters B*, 168(4):331–335, 1986.

[39] M. Roy-Stephen. *Nuclear Physics A*, 482:373, 1988.

[40] Justus H. Koch. Electron - nucleus scattering in the Δ-resonance region. Taken from Modern Topics in Electron Scattering, World Scientific Press, Edited by Frois.

[41] D. Drechsel et al. A unitary isobar model for pion photo- and electroproduction on the proton up to 1 GeV. *Nuclear Physics A*, 645:145 – 174, 1999.

[42] G. A. Warren et al. Induced proton polarization for π^0 electroproduction at Q^2=0.126 GeV^2/c^2 around the $\Delta(1232)$ resonance. *Physical Review C*, 58(6):3722–3725, 1998.

[43] L. C. Smith et al. Electroproduction results from CLAS. for the CLAS collaboration, 2000.

[44] D. Drechsel G. Knochlein and L. Tiator. Photo and electroproduction of eta mesons. *Z.Phys.*, A352:327–343, 1995.

[45] B.A. Mecking et al. The cebaf large acceptance spectrometer. *Nuclear Instruments and Methods A*, 503(3):513, 2003.

[46] M. D. Mestayer et al. The CLAS Drift chamber system. *Nuclear instrunents and methods A*, 449:81–111, 2000.

[47] F. J. Barbosa. A drift chamber system for a toroidal detector. *Nuclear Instruments and Methods A*, 323:191–197, 1992.

[48] G. Adams et al. The CLAS cerenkov detector. *Nuclear Instruments and Methods A*, 465:414–427, 2001.

[49] E.S.Smith. The time of flight system for CLAS. *Nuclear Instruments and Methods A*, 432:265, 1999.

[50] M. Ripani et al. Choice and test of the photomultiplier for the large angle electromagnetic shower calorimeter on the CLAS detector at CEBAF. *Nuclear Instruments & Methods in Physics Research A*, (406):404–410, 1998.

[51] Steven McLauchlan. Δ *Electroproduction in* ^{12}C. PhD thesis, University of Glasgow, 2003.

[52] Steven McLauchlan. Private Communication, May 2003.

[53] L. Tiator. http://www.kph.uni-mainz.de/MAID/maidnew/maidnew.html. University of Mainz website.

[54] Bjorn C. Lehnhart. *User Guide for the programmes 'crosse' and 'prod' for the Calculations of the cross sections of Pionelectroproduction with data from MAID*, March 2002.